Study on organic photovoltaic cell utilizing thin film of novel porphyrinoids

Saeki, Hiroyuki

(Degree)
博士（工学）

(Date of Degree)
2013-09-25

(Date of Publication)
2015-09-25

(Resource Type)
doctoral thesis

(Report Number)
甲第5942号

(URL)
https://hdl.handle.net/20.500.14094/D1005942

Doctoral Dissertation

博士論文

Study on organic photovoltaic cell utilizing thin film of novel porphyrinoids

新規ポルフィリノイド薄膜を用いた有機薄膜太陽電池に関する研究

July, 2013

平成２５年７月

Graduate School of Engineering, Kobe University

神戸大学大学院工学研究科

Hiroyuki Saeki

佐伯　宏之

Contents

1. Introduction

2. Current-Voltage Characteristics of Organic Photovoltaic Cells Following Deposition of Cathode Electrode

3. Evaluation of Vacuum Deposited Benzoporphycene Thin Film as Photoactive Layer

4. Fabrication of Phase-separated Benzoporphycene/[6,6]-Phenyl-C_{61}-Butyric Acid Methyl Ester Films for Use in Organic Photovoltaic Cells

5. Dimethyl Fused Benzoporphycene Precursor and Its Application to Organic Photovoltaic Cells

6. Fabrication and Semiconducting Properties of Monodisperse n-Type Phthalocyanine Nanograss

1. Introduction

1.1 Background

The energy question has become one of most major and worrying problem of the modern society. Our worldwide consumption of energy increased as consequence of the increase in the industrialization of the world. The need for energy is likely to grow even more with the improvements in standard of living across the planet.

Today, fossil fuel including petroleum, coal and gas are the most common energy sources currently in widespread use. Unfortunately, these energy sources are finite, exhaustible resources. Fossil fuel also emits large amounts of carbon dioxide and other greenhouse gases into the atmosphere. Nuclear power energy also has been playing a part in the energy policy in past decades. However, the danger of nuclear becomes apparent by the nuclear plant accident in Great East Japan Earthquake. It is expected to break the dependence on nuclear energy. From these problems, the energy saving and the use of renewable energy is expected.

Renewable energy is a collective term of the energy taken out of the natural phenomenon. It indicates sunlight, solar heat, hydraulic power, wind power, biomass, terrestrial heat, wave force, vibration and temperatures fluctuate etc. In particular, the solar cell is the most expected way in renewable energy generation. The target value of power generation was set at 53 million kW in Japan in year of 2030. However, the solar power generation capacity have limited by the long energy payback time of solar cells. The decrease of the power generating cost is indispensable for further spreading of the power generation unit, which is pointed out in NEDO "Outline of the Roadmap PV2030+".1) In the account record, the cost target is also settled on at seven yen kilowatt-hour or less in 2030. The tough hurdle can only overcome with new concept for photoconversion.

1.2 Organic photovoltaic cells

1.2.1 The position of organic photovoltaic cells in solar cells

Solar cells developed now are divided roughly into inorganic solar cells (Si and Cadmium telluride etc.) and organic solar cells (Fig. 1.1). Inorganic solar cells have already been put to practical use. Each company is mass-producing the solar cells with the following conversion efficiencies. SunPower is producing 24.2% monocrystaline silicon solar cells. Kyocera mass-produces 17% polycrystalline silicon solar cells. Solar frontiers mass-produces 17% Cadmium-Indium-Selene solar cells.

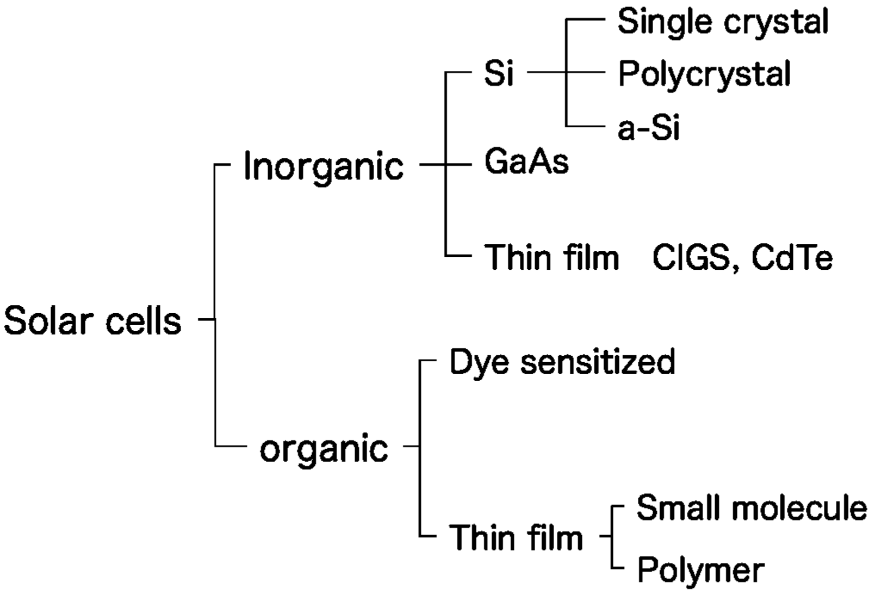

Fig. 1.1. Categories of solar cells.

Organic solar cells can also be divided into two categories, dye-sensitized solar cells (DSSCs) and organic photovoltaic (OPV) cells.

The modern version of a DSSC, also known as the Grätzel cell, has been invented in 1988. DSSC is based on a semiconductor formed on a photo-sensitized anode, a cathode and an electrolyte. The highest power conversion efficiency (PCE) reached at 11.8% in 2012. The DSSC has an attractive feature; it is simple to make using conventional roll-printing techniques. However, it has proven difficult to eliminate rigid TiO_2 layer and a number of expensive materials, notably platinum and ruthenium, which makes difficult to construct flexible and low-cost solar cell. The liquid electrolyte is also one of the problems for flexible solar cell.

On the contrary of DSSCs, OPV cell generally composed of solid films, conductive organic polymers or small organic semiconducting molecules. Recently, the PCE has been reached at 12% (heliatek) in 2013. However, it still takes time for practical use because of a decrease in efficiency when building up the modules. Further improvement in efficiency must be achieved.

Though the efficiency is still low, OPV cells have attracted considerable attention due to many of industrial advantages. The features of OPV cells are as follows. (1) Because OPV cells are composed of organic materials, it is free from a large amount of rare metals. (2) The introduction of soluble substituent into the molecule enables to adopt print technology. From the point (1) and (2), OPV cells have great merit in cost. (3) The feature of lightness and flexibility can be given when it forms on a plastic film. (4) The using dye enable to fabricate colorful solar cells. From these points, the OPV cells can be used in various situations.

1.2.2 Brief history of organic photovoltaic cells

The first OPV cells were fabricated by Calvin *et al.*2) as single layer devices in which thin film of porphyrins were sandwiched between two electrodes with different work functions (Fig. 1.2). The charge separation requires a Schottky barrier at one of the organic-electrode interfaces.

A bilayer device, first developed by C. W. Tang in 1986,3) solved the problem of tightly bound excitons by inserting an acceptor semiconductor, perylene layer, between a donor, phthalocyanine, and a cathode electrode, Al. The reported PCE was 1% under simulated AM2 conditions. The report clarified that OPV cells operate with *pn* junction principle as same as inorganics. Another advantage of the bilayer device is that the electrons are transported in the acceptor layer and the holes in the donor layer to their respective electrodes after the dissociation of excitons. Therefore, the dissociated holes and electrons are effectively separated from each other and charge recombination is greatly reduced. However, the reported PCE of bilayer device is still significantly lower than that of inorganic based PV cells. The principle reason for this low efficiency is the intrinsically short diffusion length of excitons in organic semiconductors, which are typically in order of 10 ~ 20 nm. 4-7)

The two-dimensional interface of the bilayer approach is here exchanged by a three-dimensional interpenetrating network. Bulk heterojunction solar cells 8) and *pin* junction cells 9, 10) were reported ("*i*" means the layer of mixture of *p*-type semiconductor and *n*-type semiconductor.). After a few years, the number of reports on bulk heterojunction solar cells increased exponentially. Currently, the highest reported efficiency is 12% (heliatek) with tandem structure cell.

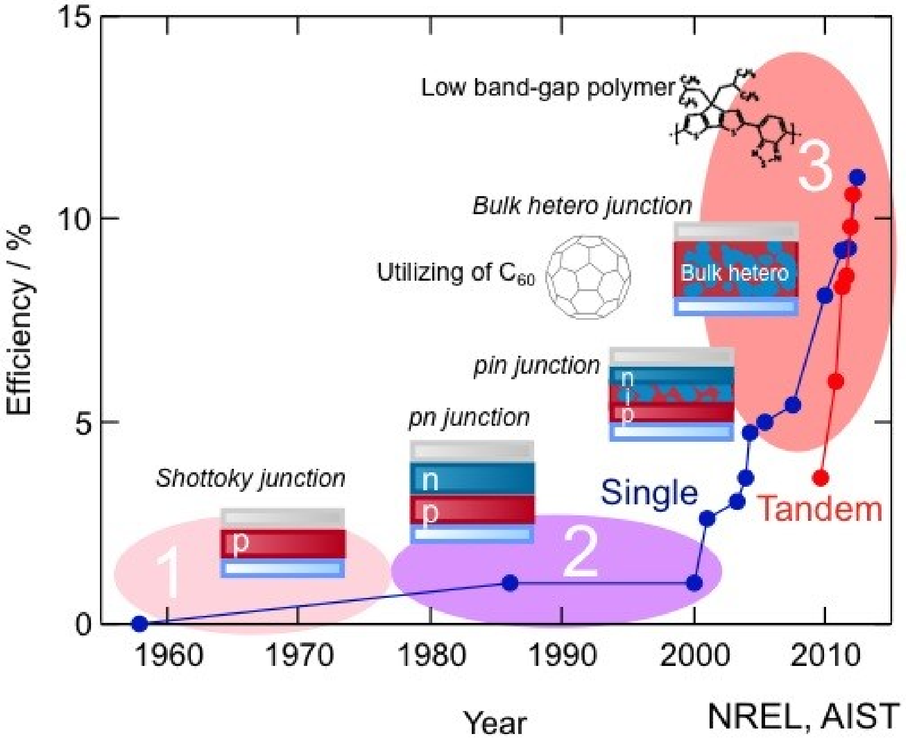

Fig. 1.2. History of efficiencies of organic photovoltaic cells.

1.2.3 Device working principle of organic photovoltaic cells

In OPV cells, the photovoltaic process of converting incident light to electricity is composed of four consecutive steps, (1) light absorption; (2) exciton diffusion to the donor-acceptor interface; (3) exciton dissociation and charge transfer; and (4) charge collection (Fig. 1.3). (1) When incident photon, which has larger energy than gaps between HOMO-LUMO, hits a molecule, a exciton is generated. After light absorption, inorganic semiconductors immediately produce free carriers, while organic semiconductors require an additional process to produce free carriers. (2) An exciton formed in the organic semiconductor diffuses to the *pn* interface and be dissociated into free electrons and holes. When excitons do not reach the *pn* interface, they recombine and the absorbed energy is dissipated without generating photocurrent. (3) Generated free electrons and holes diffuses in respective organic semiconductors. (4) Only a free career that reaches the electrode contributes to the photoelectric conversion.

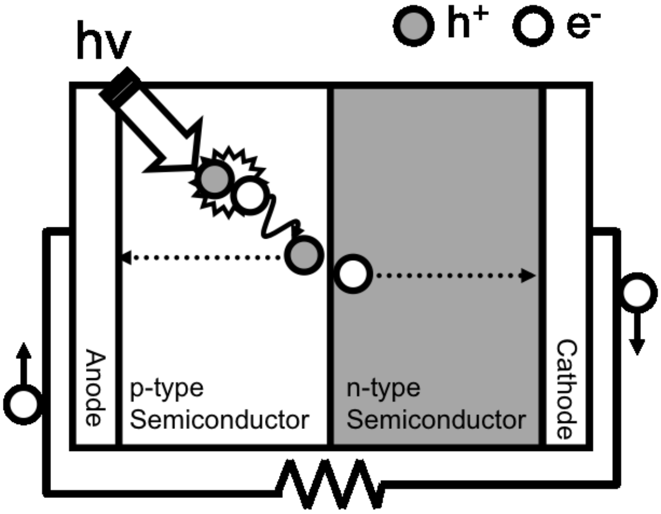

Fig. 1.3. Device working principle of organic photovoltaic cells.

1.2.4 Strategies to improve photovoltaic performance

Development of a bulk heterojunction solar cell based on the precise material design for *p*-type semiconductors and fullerenes as *n*-type organic semiconductor rapidly improved the efficiency of OPV cells. However, maximum reported external quantum efficiency (EQE), how much the absorbed photon extracts to an external circuit as a free carrier, is about 70% in the specific wavelength, and 60% in overall wavelength.11-13) The EQE is limited by the absorption of the transparent electrode and the reflection of the substrate to 75%.14) There is roughly a room for improvement about 15% internal carrier correction. In order to overcome the charge recombination problem of the bulk heterojunction OPV cells, the nanostructured OPV cell was designed.

Since excitons travel 10 to 20 nm, a 20 to 40 nm cylindrical pattern can be expected to efficiently dissociate excitons. Second, the height of the pattern should be tuned to absorb enough photons without losing free charges by recombination. For example, 200 nm thick poly-3-hexylthiophene (P3HT), which is representative organic semiconductor, absorbs over 90% of incident light at the peak of maximum absorption wavelength. In this case, the pattern height should be around 200 nm thick. Third, the continuous layer at the top and bottom of the nanostructured pattern is also important and enables to form a continuous *pn* junction (Fig. 1.4). From these points, cylindrical structure of polymer and nanoimprinting technology were developed 15) , and characterized in OPV cells. Moreover, inorganic nanorods such as TiO_2 and ZnO nanorods had also been introduced in OPV cells. 16, 17) However, the inorganic nanorod is weak to the bending and not suitable as a flexible solar cell. Therefore the nanorods of organic semiconductor are very attractive. Yang *et. al* and Hirade *et. al* fabricated the nanorod utilizing CuPc. 18, 19) Matsuo *et. al* have reported that the *p-i-n* structured OPV cells processed with benzoporphyrin (BP) precursor exhibit a high PCE of 5.2% 20). They also pointed out the importance of morphology control in the *i*-layer, since such a high PCE could be obtained due to a nanoscale structure in *i*-layer, as it called column/canyon structure. An orientational control of crystals is also important for further improvement of PCE. The free carriers transfer through the π-electron cloud. Therefore, the crystals, which closely packed with the adjacent molecule and face-to-face, are preferable. And, it is thought that tuning the direction of π-stacking to the vertical to the substrate can maximize the PCE of an OPV cell.

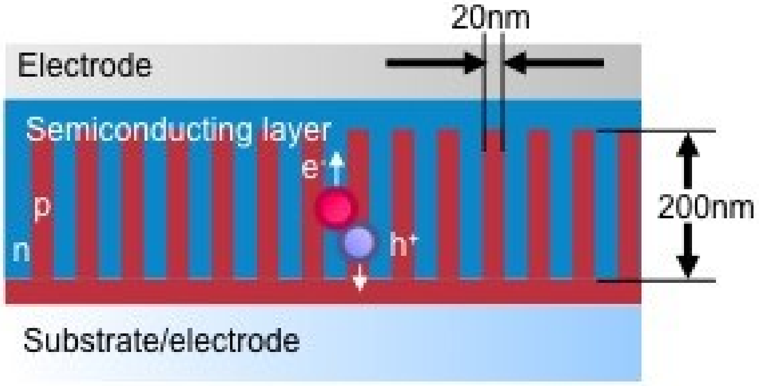

Fig. 1.4. Ordered bulk hetero junction (cylindrical structure).

Nowadays, the PCE of the OPV cell was achieved at 10%. It can be said that OPV cells entered the phase of practical use. In this phase, we have to make our effort to achieve the improvement of not only conversion efficiency but also the durability of the cells.

For further durability, it is essential to understand the degradation mechanism of OPV cells.

However many of phenomenon in the cells have not been dissolved, neither the deterioration by the current and light nor the structural stability. The influence of diffusion of oxygen and water, atoms, and molecules etc. is not also fully understood. From these points, the importance of fundamental research on the phenomenon must increase more than ever.

1.2.5 Organic semiconducting materials for photovoltaic cells

The origin of "organic semiconductors" can be date back to the 1954, when the investigations on electrical conductivities of condensed aromatic hydrocarbons such as perylene and pyrene were conducted by Inokuchi, Akamatsu, Matsunaga and co-workers. 21) Typical current carriers in organic semiconductors are holes and electrons in π-bonds. The carriers can move via π-electron cloud overlaps, especially by hopping, tunnelling and related mechanisms. Detailed physics of the electrical behavior in organic semiconductors were not completely understood with the inorganic device physics. Considerable effort has been devoted to understand the fundamental electronic structure of the organic semiconductor, in particular microscopic, molecular-scale transport processes and the interface with metals.

Organic semiconductors are roughly divided into polymer and small molecular weight material. Semiconducting polymers have been attracted considerable attention due to their potential in the application to a wet process and the advantage in manufacturing because the mechanical property is good. However, polymers generally have wide distribution of molecular weight and a difficulty of improving the purity. Moreover, polymers easily decompose under excessive heat compared with the small molecular weight materials.

On the other hand, a semiconducting small molecular can be easily recrystallized, and has the feature of high purity and crystalinity. However, the cohesive of the molecule is indispensable, a wet process cannot be applied without introduction of the appropriate substituents.

In the present study, semiconducting small molecules, in particular, macrocyclic molecules represented by porphyrins and phthalocyanines, were investigated.

Porphyrins are pigments that can either be obtained in nature or in organic synthesis. Porphyrins contain a fundamental skeleton of four pyrrole moieties connected at their α-position via methine bridges to form a planar macrocyclic structure.22) Due to their high conjugation, porphyrins show intense absorption in the visible region. The absorption spectra of porphyrins are characterized by a strong band and four weaker bands, Soret band and Q bands, respectively.23) Phthalocyanines are structural analogues of porphyrins. Their absorption spectra also show a Soret band and Q bands in the visible region. From their good photo and electric properties, the macrocyclic compounds widely investigated as the photoactive materials for OPV cells, already mentioned in 1.2.2. Hori *et. al* have been synthesized 1,4,8,11,15,18,22,25-octahexylphthalocyanine (Fig. 1.5 (a)) and reported that the OPV cells utilizing the phthalocyanine showed 3.1% PCE. 24, 25) The OPV cells utilizing zinc-phthalocyanine (Fig. 1.5 (b)) and benzoporphyrin (Fig. 1.5 (c)) showed 4.08% and 5.20%, respectively. 26, 20) These macrocyclic π-conjugated molecules are a promising material for OPV cells. These macrocyclic compounds, which also can form complexes with a range of metal ions. Large metal ions can bring together these tetrapyrrole derivatives to form shuttlecock type (Fig. 1.5 (d)). 27) Lead-phthalocyanine has the shuttlecock structure and forms J-aggregate or H-aggregate. 28) The control of aggregation enables to increase absorption range or carrier mobility. Macrocyclic compounds can also form sandwich-type double- (Fig. 1.5 (e)) and triple-decker (Fig. 1.5 (f)) 29). The control of the complex and crystal structure is the one of the important factor to improve the PCEs.

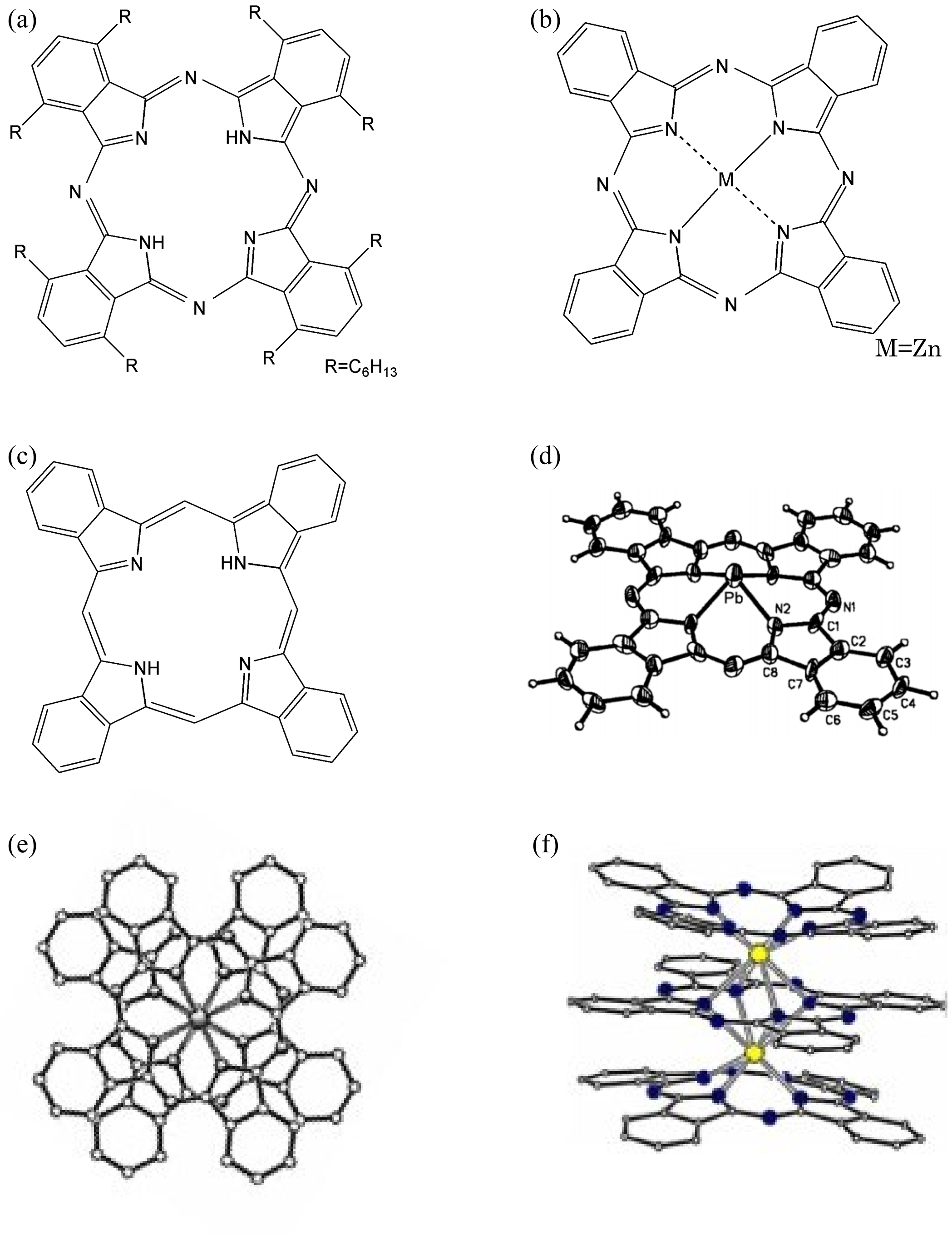

Fig. 1.5. (a) 1,4,8,11,15,18,22,25-octahexylphthalocyanine (b) zinc-phthalocyanine (c) benzoporphyrin (d) lead-phthalocyanine (e) double- and (f) triple-decker complexes.

1.3 The film formation method of organic thin films

To date, a variety of fabrication method of thin film have been developed. The fabrication processes can divide roughly into two kinds, dry process and wet process. The dry process includes vacuum evaporation method, molecular-beam epitaxy (MBE) method, sputtering technique and chemical vapor deposition (CVD) methods, etc. The wet process includes the drop cast method, the spin-coat method, the dip coat method and the Langmuir brochette method, etc. In particular, vacuum evaporation and spin-coating were widely applied for the formation of organic semiconducting thin films. These representative methods were described precisely as below section. And more, as the recent development for fabrication of organic semiconducting thin-film, the precursor method and the CVD method for organic thin film were introduced.

1.3.1 Thermal evaporation

Thermal evaporation is a method to fabricate thin film of metal, metal oxide or small molecules. The variables to control the evaporation are vacuum chamber pressure, source material purity and the temperature of evaporation source and substrate, which is correlated with the evaporation rate. Figure 1.6 summarizes the mechanism of film formation for thermal evaporation.30) When molecules evaporated from the source arrive at the substrate surface, some molecules are trapped on the surface and then moving over the surface (surface migration). Some of the migrating molecules would re-evaporate from the surface into the vapor phase (re-evaporation). When migrating molecules reach a steady position (adsorption), the molecule stay in and forms a nucleus (nucleation), and then, the admolecules on the substrate trap migration molecules. Consequently, the thin film grows up (film formation). The film over tens of nanometers generally have smooth surface because the driving force is the "deposition". However indented surface of semiconducting layer is expected to increase the area of *pn* interface in OPV cells. Nowadays, a lot of techniques for making the indented film are developed by using organic vapor phase deposition,18, 30) glancing angle deposition,26, 31-34) and molecular seeding growth.19) The switch of driving force of film formation from deposition to other force is expected to fabricate unique nanometer texture.

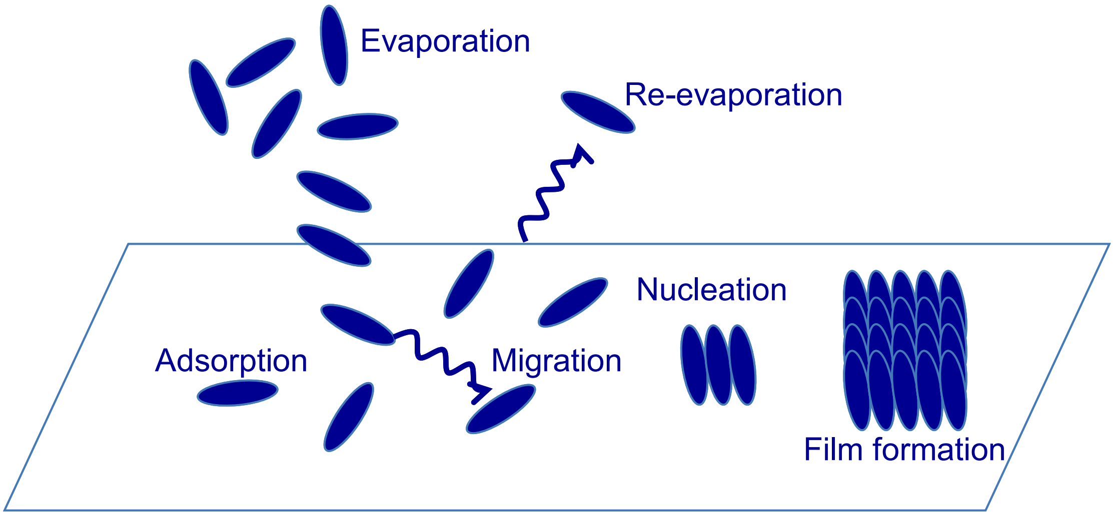

Fig. 1.6. Mechanism of film formation in thermal evaporation method.

1.3.2 Chemical vapor deposition（CVD）

Chemical vapor deposition (CVD) is a deposition process utilizing chemical reaction during the deposition. The process is often used in the semiconductor industry to produce thin films, poly silicon, amorphous silicon and silicon oxide etc. Precursor gases, which are often diluted in carrier gases, are delivered into the reaction chamber. As they pass over or come into contact with a heated substrate, they react and are deposited onto the substrate. In organic materials field, CVD and related methods have been applied to produce polymers. 35-37) Murata *et. al*38) reported the synthesis of a polyoxadiazole polymers and characterized as electroluminescent or carrier-injecting layers by optimizing the device structures. It is revealed that CVD method is very attractive method to form materials that easily decompose with the heat for evaporation.

Figure 1.7 summarizes the mechanism of film formation for CVD method. In CVD method, two compounds generally participate in the chemical reaction. In this chapter, it is assumed that element B exists beforehand. When element A evaporated from the source arrive at the substrate surface, some molecules are trapped on the surface and then moving over the surface (surface migration). Some of the migrating molecules would re-evaporate from the surface into the vapor phase (re-evaporation). When migrating molecules reach an element B, the elements react (reaction) and the production migrates (migration). When migrating molecules reach a steady position, the molecule stay in and forms a nucleus (nucleation), and then, the admolecules on the substrate trap migration molecules. Consequently, the thin film grows up (film formation). In CVD method, we have to take into account the elemental steps of not only produced materials but also the monomers.

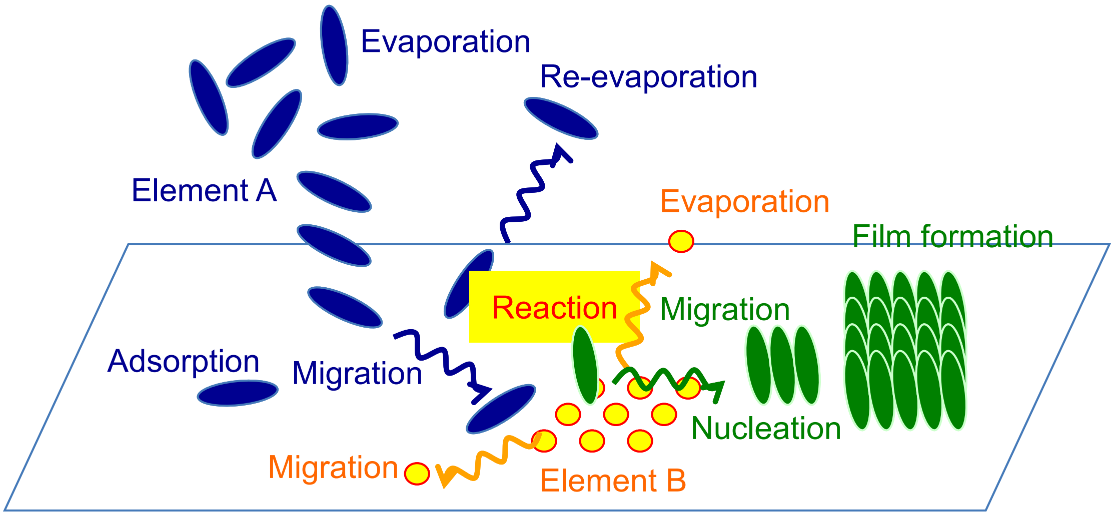

Fig. 1.7. Mechanism of film formation in CVD method.

1.3.3 Spin-coating

Spin-coating is a simple and precise method that uses centrifugal force to produce a uniform thin film ranging from 10 to 1000 nm in thickness. The variables in spin-coating process are solvent concentration, spin speed and spin time. By varying solution concentration and spin speed, the film thickness can be easily controlled. Spin time is determined by drying the wet film. During spin-coating, volatile solvent is evaporated and typical spin time is 30 sec to 1 min.

Spin-coating method have the advantages, processability, large area and low-cost. From these advantages, this process is finding application in the production of optical and magnetic recording media. In recent years, spin-coating method was also applied to fabrication of next generation organic devices such as OPV cells and organic light emitting diodes (OLEDs). However, these devices consist of multi organic layers. The spin-coated solution dissolve the under organic layer, which makes difficult to stack organic layers. The under layer must be performed some treatment of insolubilization for stacking layers.

1.3.4 Precursor for organic semiconductor

π-conjugated molecules such as pentacene, phthalocyanine and porphyrin generally have low solubility in common solvents. To overcome the problem, the introduction of soluble substituents was performed. However, the molecular design lowers the performance below that of their vacuum-deposited counterparts, because substituents inhibit π-π stacking of molecules, and therefore inhibit charge transfer between molecules. Moreover, soluble substituents generally consist of insulating hydrocarbons, which can lower the overall conductivity of materials.39)

In recent years, soluble photo-convertible and/or thermo-convertible precursors with bulky substituent have been synthesized.40-43) The bulky structure in precursor enables to dissolve precursor into solvents, and to apply wet process for film formation. Photo or heat treatment of spin-coated film causes a reaction that desorption and removal of the insulating substituent from film, and the molecules become insoluble. Over the past decade, there have been several reports on the conversion behavior from soluble precursors and the electric properties of organic compounds after conversion. 44-49) 1,4:8,11:15,18:22,25-Tetraethano-29H,31H-tetrabenzo[b,g,l,q]porphine (CP) has been synthesized by Ono *et. al* in 1998. 41) CP molecule has bicyclo structure at outer side of porphyrin ring. The bulky structure suppresses the intermolecular π-π interactions, which enable to dissolve CP into common solvents, and to apply spin-coating method for film formation. CP converts into 29H,31H-tetrabenzo[b,g,l,q]porphine （BP） with desorption of four ethylene by heat treatment, as shown in Fig. 1.8. BP slightly dissolves into dimethylformamide, pyridine and tetrahydrofuran, but insoluble against chloroform and toluene. The insolubility enable to stack organic layers without dissolving the under layer. Matsuo *et. al*20) have stacked organic layers by spin-coating onto BP layer that converted from CP, and reported 5.2% PCE. Though the precursor method is very attractive for fabrication of stacked device, not only OPV cells but also OLED and others, details of the relationship between the conversion behavior and crystal growth of the film have not been clarified. During conversion, two components exist in the film, precursor and the production. We have to consider three elementally steps for each components; migration, nucleation and film formation. In the case of thermo-convertible precursor, the substrate is kept at high temperature. Therefore the molecules have large migration energy. It become more important to investigate the dependence of the elementally film formation steps on temperature. Moreover, the mechanism of layer stacking is also unrevealed. These fundamental evaluations are indispensable to more precise design of precursor and its application.

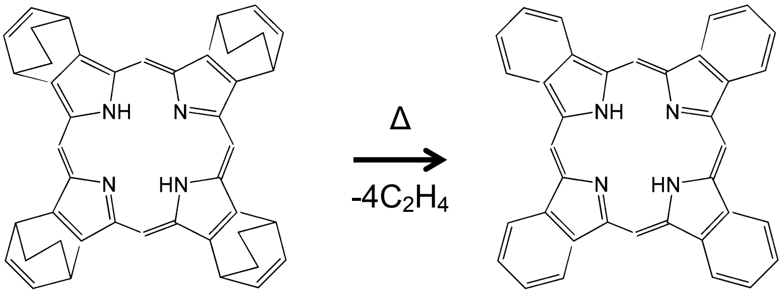

Fig. 1.8. Reaction scheme of CP to BP.

1.4 Aims and outline of the thesis

pn junction OPV cell consists of at least two semiconducting materials and two electrode materials. Therefore the device includes three different kinds of material interfaces. To evaluate precisely the effect of morphology of organic semiconducting layers on performance of OPV cell, it is indispensable to understand and control the mixing states and the energy states on the semiconductor-electrode interfaces in advance. In OPV cell, the charge separation of exciton happens on the *pn* junction. Therefore, the texture of the interface between *p*-type and *n*-type semiconducting layers is an important parameter that determines the performances of OPV cells. Increasing of *pn* interface area without disconnecting the hole-channel and electron-channel each other directly leads to high performance OPV cell. Moreover, to maximize the lifetime of exciton and charge transfer in semiconductor, the control of crystalinity of thin film is also indispensable.

Aiming at the control of interface between *p*-type and *n*-type semiconductor, and the crystalinity of organic semiconductor, the following target was set in the present study based on the above-mentioned background.

(1) The time-dependent change of semiconductor-electrode interface in an OPV cell is clarified.
(2) A new structural control method to obtain high-crystalline nano-phase-separated thin film is investigated.
(3) The film formation mechanism and crystallization are examined.
(4) The thin film is mounted on photonic and electronic devices.
(5) The relationship between film morphology and photovoltaic performance were evaluated.

This thesis is structured in the following seven sections.

In chapter 1 "Introducton", first, a general introduction to OPV cells was presented. The basic properties of macrocyclic molecules were described. As the recent development for fabrication of organic semiconducting thin-film, the precursor and CVD method were introduced. This chapter was concluded by aims and outline of the thesis.

In chapter 2 "Current-Voltage Characteristics of Organic Photovoltaic Cells Following Deposition of Cathode Electrode", the time-dependent changes of the current-voltage characteristics from immediately after Al cathode deposition until the time when the device is exposed to N_2 gas at atmospheric pressure is evaluated. The rapid change in the inner structure of OPV cells was revealed even under vacuum. The introduction of N_2 gas also increased the photovoltaic performance. It could be well explained by the formation of AlO_X. It was revealed that the formation of AlO_X layer not deteriorates rather improves the OPV performance in the case of very thin film.

In chapter 3 "Evaluation of Vacuum Deposited Benzoporphycene Thin Film as Photoactive Layer", the morphology and photovoltaic properties of vacuum deposited BPc film are evaluated. The film vacuum deposited at room temperature was composed of BPc crystals, orienting uniaxially to the substrate surface with edge-on orientation. Even though the fabrication process for OPV cells is not optimized, the OPV cell utilizing vacuum deposited BPc film showed nearly 1% PCE. The BPc can be expected as a candidate of photoactive layer in OPV cell.

In chapter 4 "Fabrication of Phase-separated Benzoporphycene (BPc)/[6,6]-Phenyl-C_{61}-Butyric Acid Methyl Ester (PCBM) Films for Use in Organic Photovoltaic Cells", the dynamics of thermal conversion from precursor to BPc and phase-separation in coexistence with fullerene derivative are examined. PCBM crystal dramatically inhibited the aggregation of BPc. It is also revealed that the BPc crystals in the underlying layer act as seed crystals after each deposition. As a result, even if the precursor has low solubility and a high cohesive property, it is enable to form a film that is thick enough to apply as the photoactive layer by repeating spin-coating and subsequent annealing. It should be noted that the BPc crystals converted from BPc-pre also oriented uniaxially to the substrate surface with edge-on orientation but with random in-plane. The phase-separated structure was heavily depended on the annealing temperature. The OPV cells utilizing optimized structure showed 0.16% PCE.

A novel BPc precursor with more bulky substituent is synthesized in chapter 5. The cohesion of precursor was dramatically suppressed, which enable to form smooth BPc film. The crystalinity was improved by high temperature annealing without increasing of the surface roughness and changing the molecular orientation. By utilizing these BPc films prepared from novel precursor, the correlation between the crystalinity of films and the photoelectric conversion characteristic is analyzed in detail. It is revealed that the hole mobility was 10-fold enhanced and the PCE was doubled by utilizing crystalized BPc film instead of amorphous like one. The OPV cells utilizing high crystalline BPc film reached 1.5%, 1.5 times the PCE of OPV cells utilizing vacuum deposited BPc film. The importance of crystalinity for enhancing the PCE was experimentally demonstrated.

BPc takes edge-on orientation and preferentially forms tabular crystals. The control of the direction of crystal growth is critical factor for the film texture. In chapter 6 "Fabrication and Semiconducting Properties of Monodisperse n-Type Phthalocyanine Nanograss", dipotassium-2,3,9,10,16,17,23,24-octacyanophthalocyanine–potassium ($K_2Pc(CN)_8$–K) complex was focused because it is known that metal-2,3,9,10,16,17,23,24-octacyanophthalocyanine ($MPc(CN)_8$) molecules formed from tetracyanobenzene (TCNB) and metals take face-on orientation and stack face-to-face in $MPc(CN)_8$–M complex crystal on the metal substrate. The process was controlled to achieve monodisperse nanograss with individual rod diameters of 60 nm and lengths of 250 nm by adjusting the feed amount of TCNB and the reaction temperature. OPV cells containing $K_2Pc(CN)_8$–K as an *n*-type semiconductor were fabricated, and the PCE of a cell containing vertical-aligned-nanograss was approximately four times larger than that of a nanograss dispersed bulk-heterojunction-type cell. These results support that the film fabricated by CVD method has good semiconducting properties and utilization of nanograss is efficient for improvement of the PCE in OPV cells.

Chapter 7 summarizes the results presented in this thesis, and provides an outlook for further investigation of film formation and potential device improvement.

1.5 Reference

[1] NEDO “Outline of the Roadmap PV2030+”.

[2] D. Kearns, M. Calvin, *J. Chem. Phys.*, 29, 950 (1958).

[3] C. W. Tang, *Appl. Phys. Lett.*, 48, 183 (1986).

[4] M. Theander, A. Yartsev, D. Zigmantas, V. Sundstrom, W. Mammo, M.R. Andersson, O. Inganas, Phys. Rev. B, 61, 12957 (2000).

[5] A. Haugeneder, M. Neges, C. Kallinger, W. Spirkl, U. Lemmer, J. Feldmann, U. Scherf, E. Harth, A. Gugel, K. Mullen, *Phys. Rev. B*, 59, 15346 (1999).

[6] J. J. M. Halls, K. Pichler, R.H. Friend, S.C. Moratti, A.B. Holmes, *Appl. Phys. Lett.*, 68, 3120 (1996).

[7] T. Stubinger, W.J. Brutting, *J. Appl. Phys.*, 90, 3632 (2001).

[8] G. Yu, A. J. Heeger, *J. Appl. Phys.*, 78, 4510 (1995).

[9] M. Hiramoto, H. Fujiwara, M. Yokoyama, *Appl. Phys. Lett.*, 58, 1062 (1991).

[10] M. Hiramoto, H. Fujiwara, M. Yokoyama, *J. Appl. Phys.*, 72, 3781 (1992).

[11] Y. He, G. Zhao, B. Peng, Y. Li, *Adv. Func. Mater.*, **20**, 3383 (2010).

[12] Y. Liang, L. Yu, *Acc. of Chem. Res.*, **43**, 1227 (2010).

[13] Y. Sun, G. C. Welch, W. L. Leong, C. J. Takacs, G. C. Bazan, A. J. Heeger, *Nature Mater.*, **11**, 44 (2012).

[14] R. R. Lunt, T. P. Osedach, P. B. Brown, J. A. Rowehl, V. Bulovic, *Adv. Mater.*, **23**, 5712 (2011).

[15] X. He, F. Gao, G. Tu, D. Hasko, S. Huttner, U. Steiner, N. C. Greenham, R. H. Friend, W. Huck, *Nano Lett.*, 10, 1302 (2010).

[16] K. Takanezawa, K. Tajima, K. Hashimoto, *Appl. Phys. Lett.*, 93, 063308 (2008).

[17] W. H. Baek, Il. Seo, T.S. Yoon, H. H. Lee, C. M. Yun, Y. S. Kim, *Sol. Ene. Mater. & Sol. Cell.*, 93, 1587 (2009).

[18] F. Yang, M. Shtein, S.R. Forrest, *Nature Mater.*, 4, 37 (2005).

[19] M. Hirade, H. Nakanotani, M. Yahiro, C. Adachi, *ACS App. Mater. Interfaces*, 1, 80 (2010).

[20] Y. Matsuo, Y. Sato, T. Niinomi, I. Soga, H. Tanaka, E. Nakamura, *J. Am. Chem. Soc.*, 131, 16048 (2009).

[21] H. Akamatsu, H. Inokuchi, Y. Matsunaga, *Nature*, 173, 168 (1954).

[22] A. D. Mcnaught, A. Wilkinson, IUPAC. Compendium of Chemical Terminology, 2nd ed. (the "Gold Book"), Blackwell Scientific Publications, Oxford (1997).

[23] T. Hashimoto, Y.-K. Choe, H. Nakano, K. Hirao, *J. Phys. Chem. A*, 103, 1894 (1999).

[24] T. Hori, Y. Miyake, N. Yamasaki, H. Yoshida, A. Fujii, Y.Shimizu, M. Ozaki, *Appl. Phys. Express*, 3, 101602 (2010).

[25] T. Hori, N. Fukuoka, T. Masuda, Y. Miyake, H. Yoshida, A. Fujii, Y. Shimizu, M. Ozaki, *Sol. Ener. Mater. and Sol. Cells*, 95, 3087 (2011).

[26] Y. Zhou, T. Taima, T. Miyadera, T. Yamanari, M. Kitamura, K. Nakatsu, Y. Yoshida, *Nano Lett.*, 12, 4146 (2012).

[27] K. Ukei, *Acta Cryst.*, B29, 2290 (1973).

[28] Y. Iyechika, K. Yakushi, I. Ikemoto, H. Kuroda, *Acta Crystallogr., Sect. B: Struct. Crystallogr. Cryst. Chem.*, 38, 766 (1982).

[29] J. Jiang, Functional Phthalocyanine Molecular Materials - Structure and Bonding, 135, Springer (2010).

[30] F. Yang, M. Shtein, S. R. Forrest, *J. App. Phys.* 98, 014906 (2005).

[31] Y. Zheng, R. Bekele, J. Ouyang, J. Xue., *Org. Electron.* 10, 1621 (2009).

[32] N. Li, S. R. Forrest, *Appl. Phys. Lett.* 95, 123309 (2009).

[33] J. G. Van Dijken, M. D. Fleischauer, M. J. Brett, *J. Mater. Chem.* 21, 1013 (2011).

[34] J. G. Van Dijken, M. D. Fleischauer, M. J. Brett, *J. Org. Electron.* 12, 2111 (2011).

[35] H. Naito, A. Kubono, M. Funahashi, N. Yoshimoto, Advanced Technology of Molecular Alignment for Organic Electronics, CMC Publishing (2007).

[36] A. Kubono, N. Okui, *Prog. Polym. Sci.*, 19, 389 (1994).

[37] R. Sreenivasan , K. K. Gleason, *Chem. Vap. Deposition*, 15, 77 (2009).

[38] H. Murata, S. Ukishima, H. Hirano, T. Yamanaka, *Polym. For adv. Tech.*, 8, 459 (1997).

[39] A. R. Murphy, J. M. J. Frechet, *Chem. Rev.*, 107, 1066 (2007).

[40] A. R. Brown, A. Pomp, D. M. de Leeuw, D. B. M. Klaassen, E. E. Havinga, P. Herwig, K. Mullen, *J. Appl. Phys.*, 79, 2136 (1996).

[41] S. Ito, T. Murashima, H. Uno and N. Ono, *Chem. Commun.*, 1661 (1998).

[42] H. Uno, Y. Yamashita, M. Kikuchi, H. Watanabe, H. Yamada, T. Okujima, T. Ogawa, N. Ono, *Tetrahedron Lett.*, 46, 1981 (2005).

[43] A. Afzali, C. D. Dimitrakopoulos, T. L. Breen, *J. Am. Chem. Soc.*, 124, 8812 (2002).

[44] S. Aramaki, Y. Sakai, N. Ono, *Appl. Phys. Lett.*, 84, 2085 (2004).

[45] H. Yamada, T. Okujima, N. Ono, *Chem. Commun.*, 2957 (2008).

[46] N. Noguchi, S. Junwei, H. Asatani, M. Matsuoka, *Cryst. Growth and Design*, 10, 1848 (2010).

[47] S.-Y. Ku, C. D. Liman, J. E. Cochran, M. F. Toney, M. L. Chabinyc, C. J. Hawker, *Adv. Mater.*, 23, 2289 (2011).

[48] M. Guide, X.-D. Dang, T.-Q. Nguyen, *Adv. Mater.*, 23, 2313 (2011).

[49] Y. Murai, M. Misaki, K. Ishida, Y. Ueda, *App. Phys. Express*, 4, 121603 (2011).

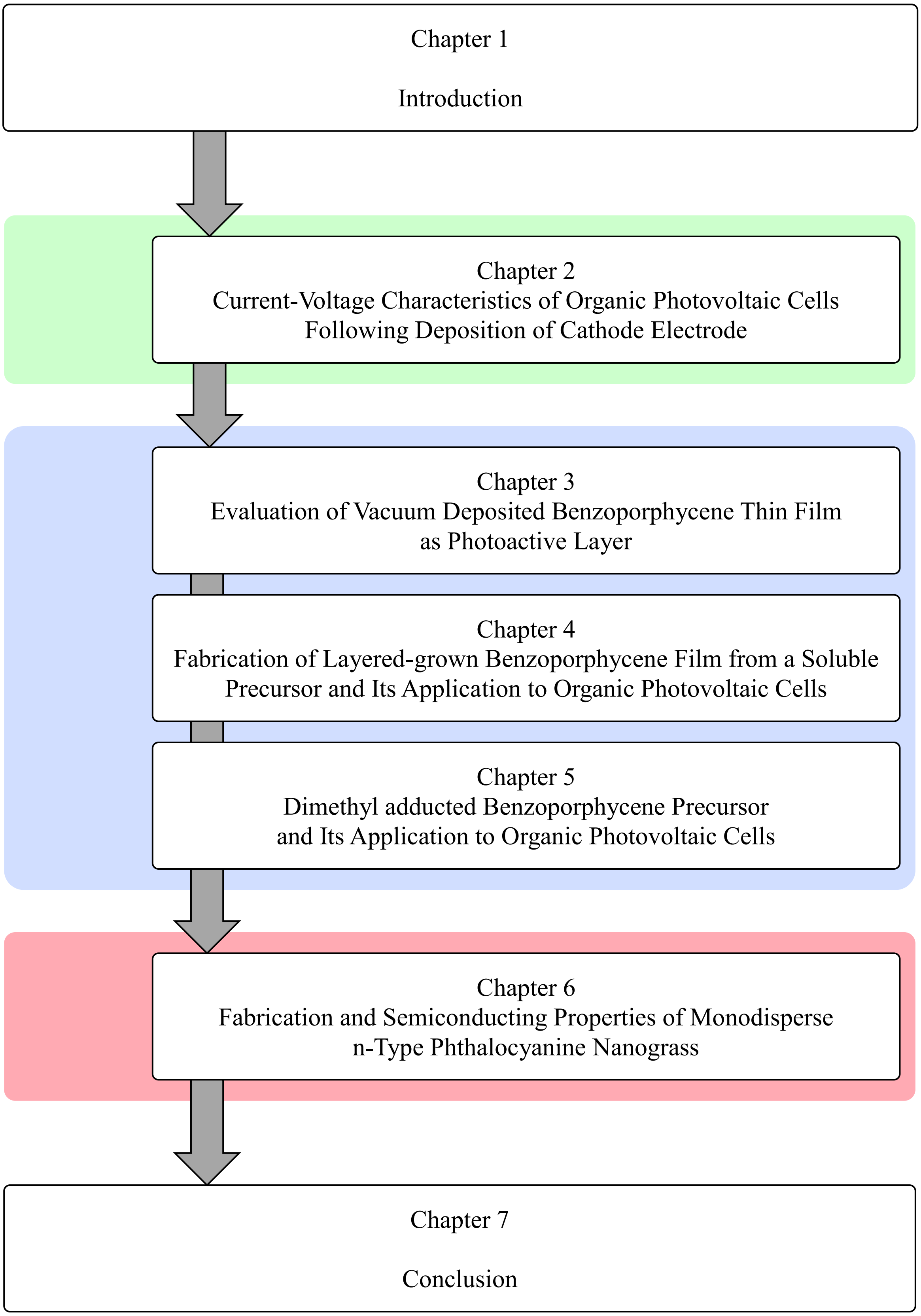
Chapter 1
Introduction
Chapter 2
Current-Voltage Characteristics of Organic Photovoltaic Cells Following Deposition of Cathode Electrode
Chapter 3
Evaluation of Vacuum Deposited Benzoporphycene Thin Film as Photoactive Layer
Chapter 4
Fabrication of Layered-grown Benzoporphycene Film from a Soluble Precursor and Its Application to Organic Photovoltaic Cells
Chapter 5
Dimethyl adducted Benzoporphycene Precursor and Its Application to Organic Photovoltaic Cells
Chapter 6
Fabrication and Semiconducting Properties of Monodisperse n-Type Phthalocyanine Nanograss
Chapter 7
Conclusion

2. Current-Voltage Characteristics of Organic Photovoltaic Cells Following Deposition of Cathode Electrode

2.1 Introduction

Organic photovoltaic (OPV) cells are expected to be next-generation solar energy conversion devices that promise to be light, flexible and printable. Control of the charge transport at the hetero-interfaces of multilayered OPV structures is one of the most important issues for the improvement of OPV cells.[1-9)] It has been reported that the insertion of buffer layers between the organic layer and the electrodes improves the device performance.[2-9)] For example, the insertion of a LiF layer that is several nanometers thick between the organic layer and an Al electrode is one of the most effective ways to improve performance.[8)] However, the detailed effects and mechanism of improvement of parameters are still not entirely clear. In addition, hetero-interfaces can be easily affected by external factors over time,[10-12)] which makes evaluation even more difficult. In order to clarify the hetero-interface phenomena, it is necessary to evaluate OPV cells soon after formation of the interface (vacuum deposition of a metal electrode). In this chapter, the time-dependent changes of the current-voltage (*J-V*) characteristics from immediately after Al cathode deposition until the time when the device is exposed to N_2 gas at atmospheric pressure is reported on before evaluation of the effect of the morphologies of photoactive layer (Chapter 3~6).

2.2 Experimental

2.2.1. Device fabrication

The OPV cell configuration used was indium tin oxide (ITO)/ poly(3,4-ethylenedioxythiophene):poly(styrenesulfonate) (PEDOT:PSS) / tetrabenzoporphyrin (BP)/ [6,6]-phenyl-C_{61}-butyric acid methyl ester (PCBM)/ Al. The BP/fullerene derivatives materials were selected because they have both high stability and high power conversion efficiency (PCE, η) of 5.2% with an optimized *p-i-n* structure.[13)] Moreover, the photoactive layer of *p-i-n* structure is fully covered with *n*-type semiconductor. There is no need to consider the contact between *p*-type semiconductor and electrode material. The *p-i-n* structure enables to simplify the contact between photoactive layer and electrode. The BP layer was fabricated by using precursor method as shown in chapter 1; spin-coating of 1,4:8,11:15,18:22,25-tetraethano-29H,31H-tetrabenzo[b,g,l,q]porphine (CP) and subsequent annealing. The fabrication process of OPV cells utilizing BP/PCBM was as follows. A 20 nm of the PEDOT:PSS was deposited from an aqueous solution on the top of a glass substrate with patterned ITO layers by a spin-coating at 3000 rpm. The layer was then annealed at 135 °C for 10 min. A solution of the CP in chloroform/chlorobenzene (1:1 (v/v)) (0.5% (w/w)) was spin-coated on the glass/ITO/PEDOT:PSS substrate at 1500 rpm. The as-spun film was thermally converted to BP by annealing at 250 °C for 3 min to form a donor *p*-layer (30 nm). In the second step, a homogeneous mixture (a typical weight ratio of 5:5) of CP and an acceptor PCBM in chloroform/chlorobenzene (1.0% (w/w)) was spin-coated at 1500 rpm, and CP was also converted at 250 °C to form a 40-nm-thick *i*-layer. Subsequent spin-coating of 1% (w/w) PCBM/ toluene solution to form 30-nm-thick *n*-layer and constructed the *p*-*i*-*n* structure. The device was then transferred into a chamber for Al deposition. In order to evaluate the photovoltaic parameters of the devices immediately after Al deposition, the solar simulator and measurement system were attached to the evaporation chamber (Fig. 2.1). A measurement probe was contacted to the ITO electrode and another one was contacted to the area that was to be deposited with Al to allow measurement soon after Al deposition. Prior to evacuation, the evaporation chamber was displaced with an inert gas at least several times to prevent residual gases, such as oxygen. An Al layer (100 nm) was deposited through a shadow mask in 3×10^{-4} Pa. The effective area of the devices was 0.06 cm^2. The light flux was set 80 mW/cm^2 light illumination, produced with a filtered Xe-lamp in a solar simulator. The *J*-*V* characteristics were then measured using a Keithley 2400 source measurement unit under vacuum or atmospheric pressure.

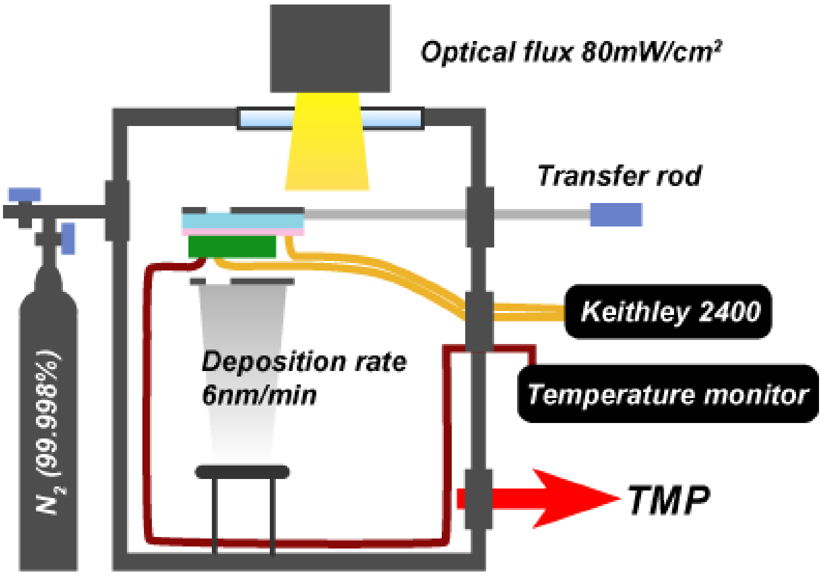

Fig. 2.1. Schematic representation of deposition and measurement set-up.

2.2.2. Characterization of OPV cells in the dark

For an ideal diode,[14)] the dark current density (J_{dark}) is

$$J_{dark} = J_0\left\{exp\left(\frac{qV}{n_d kT}\right)-1\right\} \tag{2.1}$$

where J_0 is a reverse saturation current, q is elementary charge, n_d is diode factor, k is Boltzmann's constant and T is temperature in degrees Kelvin. The overall current-voltage response of the cell can be approximated as the sum of the short circuit photocurrent (J_{SC}) and the dark current. The net current density in the cell is as follows.

$$J_{illumination} = -J_{SC} + J_0\left\{exp\left(\frac{qV}{n_d kT}\right)-1\right\} \tag{2.2}$$

When we consider parasitic resistances such as series resistance (R_s) and shunt resistance (R_{sh}), a electrical circuit of photovoltaic device is depicted in Fig. 2.2. The equation (2.2) is modified as follows.

$$J = -J_{SC} + J_0\left\{exp\left(\frac{qV}{n_d kT}\right)-1\right\} + \frac{V - JAR_s}{R_{sh}} \tag{2.3}$$

where A is the device area. The series resistance arises from the resistance of the materials, which can be calculated from the high correct bias. The shunt resistance arises from leakage of current through the cell, which can be calculated from the slope at high inverse bias.

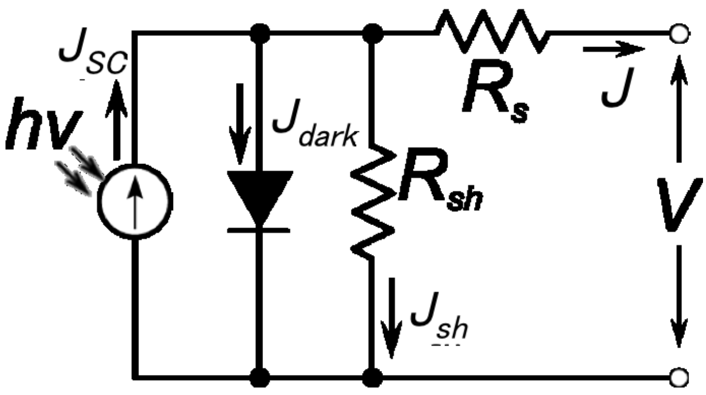

Fig. 2.2. Equivalent circuit of PV cells.

2.2.3. Characterization of OPV cells under illumination

By recording the *J–V* curves under illumination, it is possible to determine the maximum power output; the PCE (η). As shown in Fig. 2.3, the photovoltaic parameters also can be derived from the *J–V* characteristics under illumination, the short circuit current density (J_{SC}), the open circuit voltage (V_{OC}), and the fill factor (*FF*). J_{SC} is the current density, which flows with zero load resistance (V=0, short circuit conditions), and it corresponds to the maximum current generated by the cell under illumination. V_{OC} is the voltage in conditions of open circuit, when no current flows through the cell. The *FF* is the ratio of the maximum power that can be drawn from the device (W_{MAX}) and the multiplication of V_{OC} and J_{SC} (Eq. 2.4).

$$FF = \frac{W_{MAX}}{V_{OC} \times J_{SC}} \tag{2.4}$$

η can be calculated from the defined parameters. η is the ratio of the maximum generated power to the incident optical power (P_{in}). Hence, η can be expressed as follows (Eq. 2.5)

$$\eta = \frac{W_{MAX}}{P_{in}} \times 100 = \frac{V_{OC} \times J_{SC} \times FF}{P_{in}} \times 100 \tag{2.5}$$

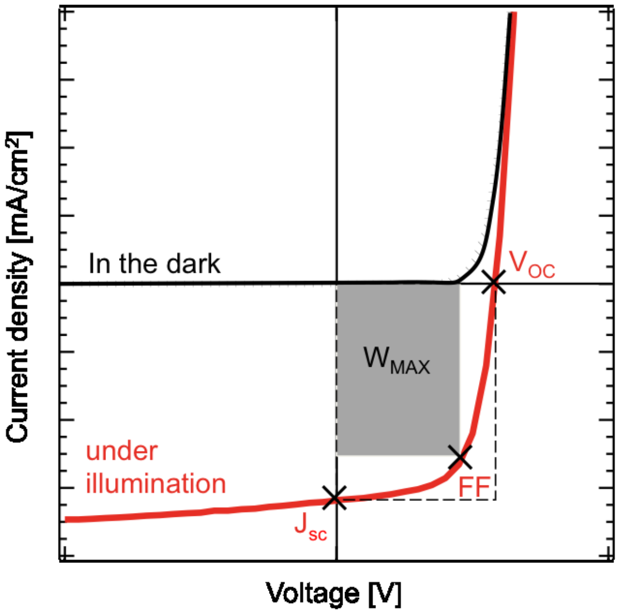

Fig. 2.3. Typical J-V curves of OPV cell under illumination and in the dark.

2.3 Results and Discussion

Figure 2.4(a) shows the *J-V* characteristics measured just after Al deposition (dashed line) and following 30 min (solid line). Although the characteristics have almost the same PCE of approximately 1%, each OPV parameter (V_{OC}, J_{SC}, and FF) was shifted slightly, shown in Table 2.I. V_{OC} increased from 0.42 to 0.45 V, while J_{SC} and FF decreased from 4.23 to 4.10 mA/cm^2 and from 0.47 to 0.45 for 30min, respectively.

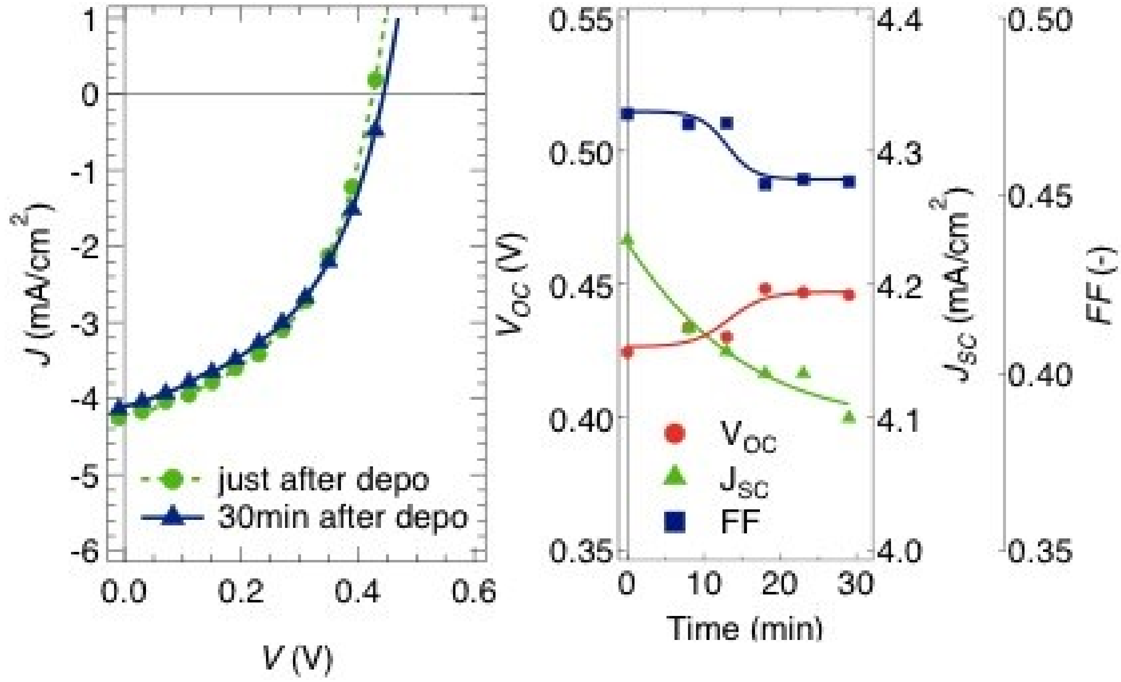

Fig. 2.4. (a) J-V characteristics of the OPV cell under 80mW/cm^2 light, (dotted line) just after Al deposition, (solid line) following 30min after Al deposition.
(b) Behavior of the photovoltaic parameters, V_{OC}(●), J_{SC}(▲), and FF(■).

Table 2.1. The photovoltaic parameters during procedure.

		V_{OC} [V]	J_{SC} [mA/cm^2]	FF [-]	PCE [%]
(A)	3×10^{-4} Pa	0.42	4.23	0.47	1.04
(B)	(30 min)	0.45	4.10	0.45	1.04
Introduction of N_2 gas					
(C)	1×10^5 Pa	0.52	4.30	0.46	1.29

The time-dependent changes of each OPV parameter are shown in Fig. 2.4(b). The parameter shifts were reproducible and were not due to thermal effects by Al deposition, because the temperature change of the OPV cells was maintained at less than ±1 °C. The origin of the parameter shifts is not clear, but appears to be related to relaxation phenomenon at the organic-inorganic interface. Hereafter, this relaxation phenomenon is referred to as the aging effect.

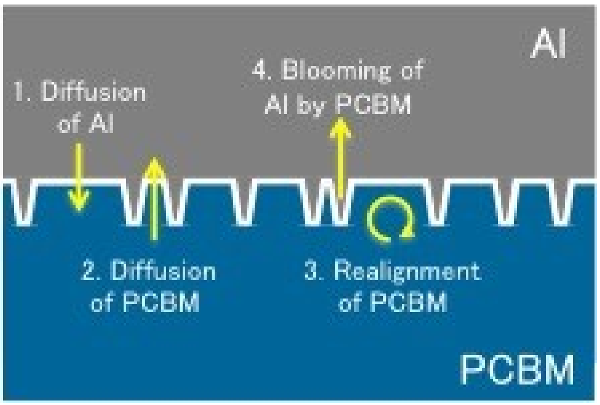

Fig. 2.5. Schematic image of the mechanism for aging effect.

It is well known that the melting point of Al is 660 °C. Therefore Al is deposited on organic layer with large thermal energy and diffuses into organic layer during deposition. After deposition, four patterns of mechanism about the aging effect can be drawn as shown in Fig. 2.5.

[1] Further diffusion of Al.

[2] Diffusion of PCBM into Al.

[3] Realignment of PCBM.

[4] Blooming of Al by PCBM.

To verification of four hypotheses, we evaluated the *J*-*V* characteristics in detail. J_{SC} is the photovoltaic parameter, the indicator how much photon converts into current. In this aging term, it is assumable that not only the amount of incident photon but also every interface without PCBM-Al is stable. Therefore, decreasing of J_{SC} directly indicates that the efficiency of charge transfer at PCBM-Al interface decreases as the aging time. PCBM consist of fullerene and insulating side chain group. The insulating hydrocarbons can lower the conductivity. Direction of side chain against metal electrode is the one of the probable mechanism (mechanism [3]). When PCBM extract Al from itself, the area of interface between PCBM and Al decreases. It also leads to decreasing of J_{SC}. Therefore, not only the realignment of PCBM but also the blooming of Al by PCBM (mechanism [4]) is also the probable mechanism.

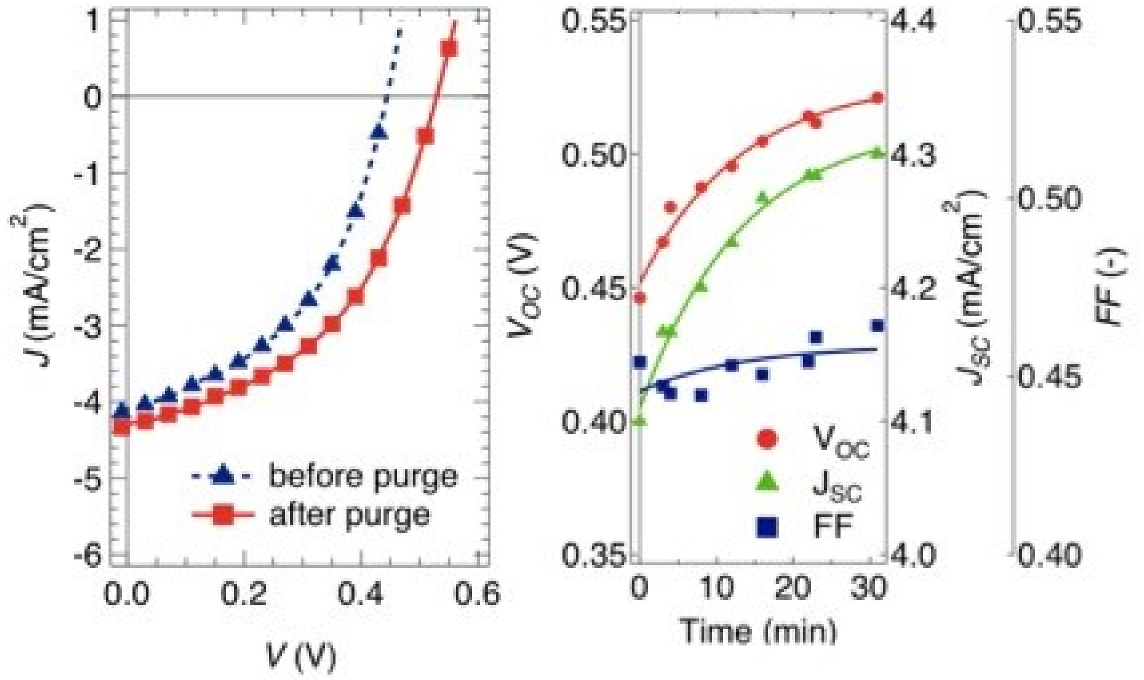

Fig. 2.6. (a) J-V characteristics of the OPV cell under 80mW/cm2 light. (dotted line) before (at 30min after Al deposition), (solid line) 30min after the introduction of N_2 gas. (b) Behavior of photovoltaic parameters, V_{OC}(●), J_{SC}(▲), and FF(■).

Figure 2.6(a) shows the *J-V* characteristics before (30 min after Al deposition; dashed line) and 30 min after displacement of N_2 (99.998%) gas into the vacuum chamber (solid line) to atmospheric pressure. The OPV performance was clearly improved by the introduction of N_2 gas. The time-dependent changes of each OPV parameter are shown in Fig. 2.6(b). Here, the finished time of N_2 displacement is redefined as 0 min. Large shifts were observed in all parameters, but such shifts became saturated for 30 min after the N_2 displacement. V_{OC} changed from 0.45 to 0.52 V and the increase of V_{OC} reached 0.10 V in total procedure. J_{SC} and FF also increased from 4.10 to 4.30 mA/cm^2 and from 0.45 to 0.46, respectively. The resulting PCE was increased 24% from first characterization, as shown in Table 2.1. J_{SC} and FF exhibited different trends under N_2 gas atmosphere compared with that under vacuum, which implies a different mechanism under each condition. UV-vis spectrum and X-ray diffraction analysis were carried out on the device before and after Al evaporation. The BP/PCBM films before and after deposition of 10 nm thick Al were evaluated. Figure 2.7(a) shows the UV-vis absorption spectra before (blue) and after deposition (red).

No specific change was observed. Figure 2.7(b) shows the results of XRD analysis. In vacuum deposited film, the (111) plane reflection of Al crystal was observed. However, XRD results also indicated that there is no change in structure of thin films. These results indicate that the change of *J*-*V* characteristics is not due to the effect of the bulk condition but due to interfacial condition.

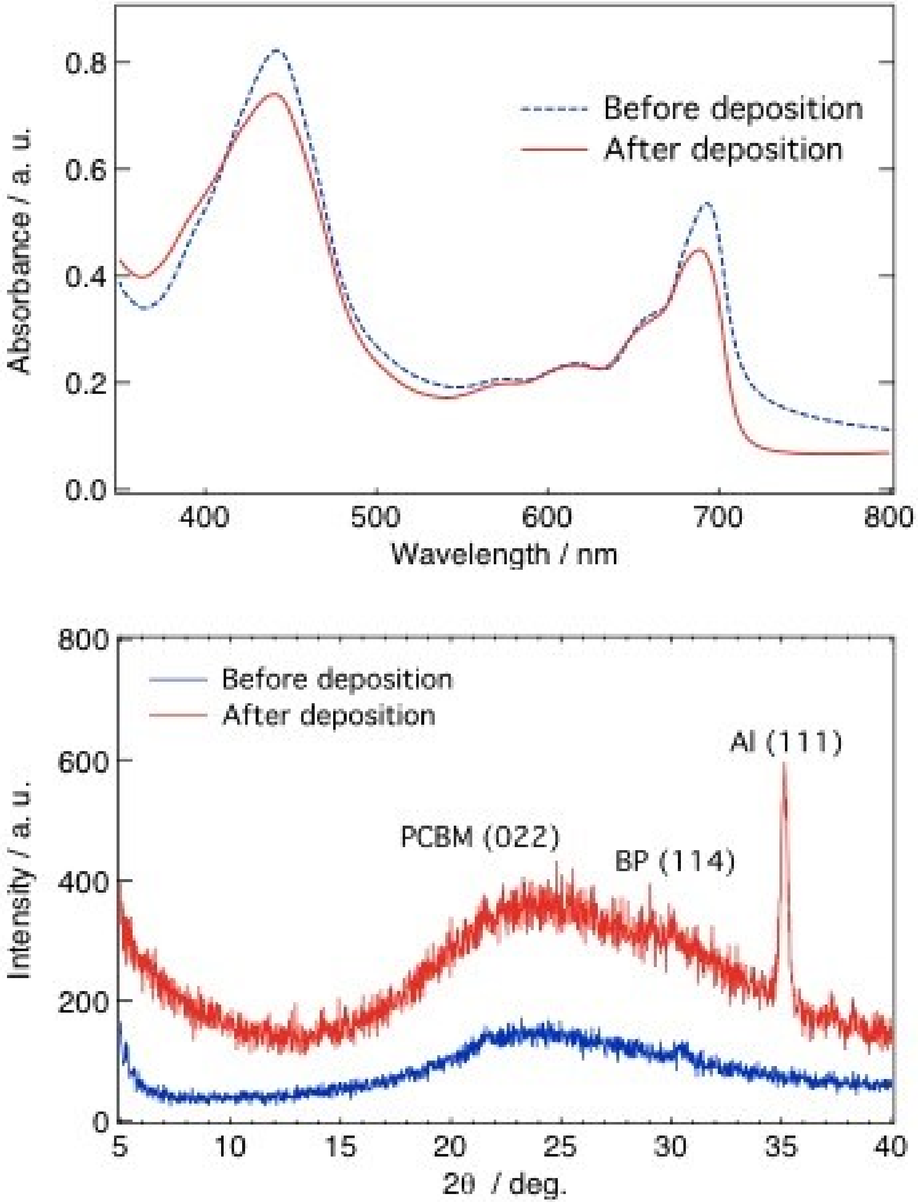

Fig. 2.7. (a) UV-vis spectra and (b) XRD profiles of p-i-n stacked organic thin films before and after deposition of Al.

The results could be explained by formation of AlO_X at the organic-inorganic interface. It is assumed that the formation of AlO_X is caused not by oxygen included in organic layer (internal oxidation), but by oxygen from the introduced dry N_2 gas (external oxidation), because if the formation of AlO_X is caused by internal factors, similar shifts (increased J_{SC} and FF) should be observed even under vacuum. To ensure the effect of external oxidation on each OPV parameter, the J-V characteristics were also investigated after the introduction of an inert gas with different purity (Ar, 98%). Figure 2.8 shows the time dependent change in V_{OC} after purge of N_2 (99.998%) and Ar (98%).

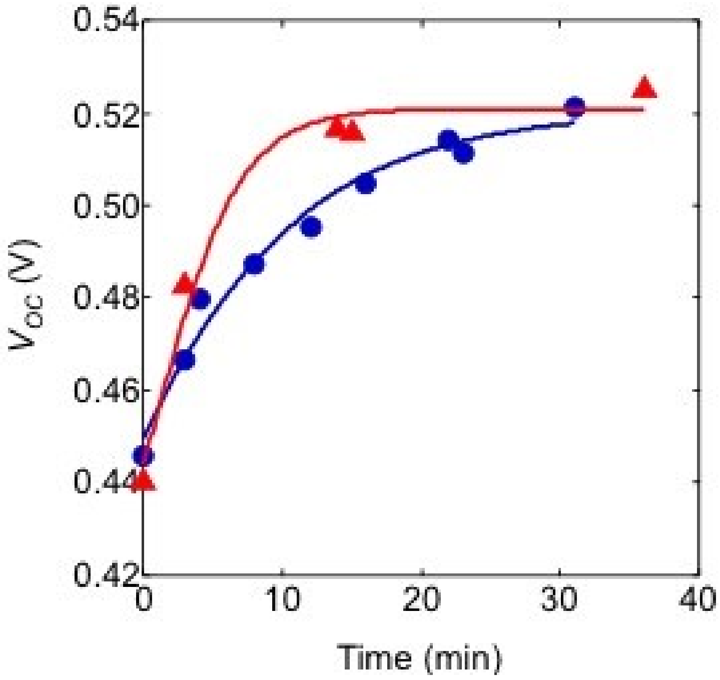

Fig. 2.8. Time dependent change of V_{OC} after purge of N_2 (99.998 %) (●) and Ar (98 %) (▲).

The V_{OC} shift amount was the same as that in N_2 procedure, but the speed of shift in V_{OC} was dependent on the purity of inert gas. In the case of N_2 gas (99.998%), it took 30 min to reach the saturated value. On the other hand, it took only 10 min in Ar procedure (98%). Thus, low degree of purity accelerated the oxidation of Al. Surprisingly, our results indicated that very slight amount of impurities affect the characteristics of OPV cells. The most striking result in this experiment is the widely shift in V_{OC}. In general, the interface sensitively affects to the OPV performances. It is reported that the insertion of buffer layer acts as dipole-moment (LiF),[8,16] exciton blocking layer (bathocuproine (BCP),[17] lowering of work function (tris(8-hydroxyquinolinato) aluminium (Alq3)).[18] To clarify the effect of AlO_X on V_{OC}, the J-V characteristics were investigated in the dark.

Figure 2.9 shows the J-V characteristics measured in the dark before and after introduction of dry N_2 gas into vacuum chamber. In order to better visualize the changes, the current density is displayed with a logarithmic scale. Dry N_2 gas causes a lowering of the current density within the overall range and the shoulder at low-bias is diminished from 0 to 0.3 V. The J-V characteristics in the dark were then analyzed using the Eq. (2.1). It follows that the lowering of current density and diminishment of the shoulder at low-bias cause decrease of the J_0 and n_d values, respectively. V_{OC} is expressed in the following Eq. (2.6) using J_0 and n_d.[15)]

$$V_{OC} = \frac{n_d kT}{q} ln\left(\frac{J_{ph}}{J_0}\right) \qquad (2.6)$$

This formula indicates that the widely V_{OC} shift in this experiment was due to lowering of J_0 induced by high rectification.

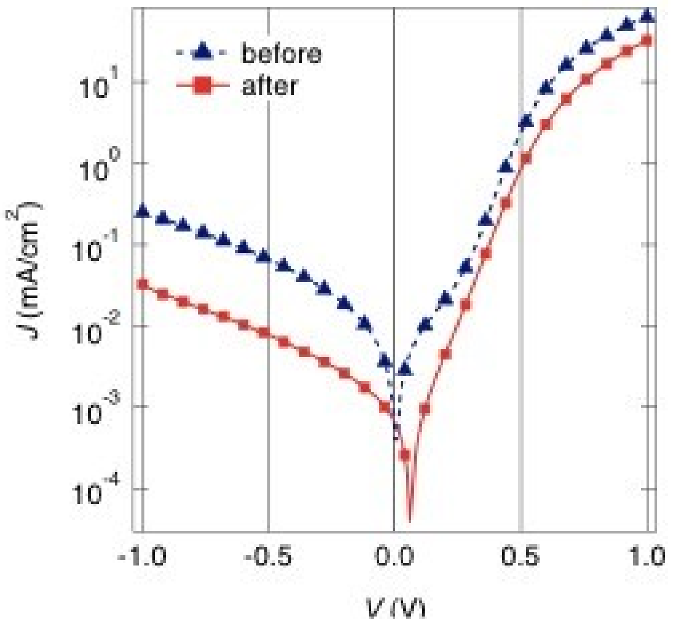

Fig. 2.9. J-V characteristics of the device before and after N_2 gas purge in the dark.

To more precisely evaluate the rectification, the series and shunt resistance were also investigated. Figure 2.10 shows the time-depoendent change of series and shunt resistance. After N_2 purge, the series resistance increased from 101 to 153 Ω. On the other hand, shunt resistance was dramatically increased from 2.7×10^4 to 19.0×10^4 Ω, with order of magnitude. It is well known that the series resistance decreases the device performance. However this result indicate that the performance can be increase by overwhelming the effect of increase of shunt resistance, resulting in high rectification and improvement of PCE. The lowering of the leakage current by the very thin insulating layer is the promising way to improve the PCE.

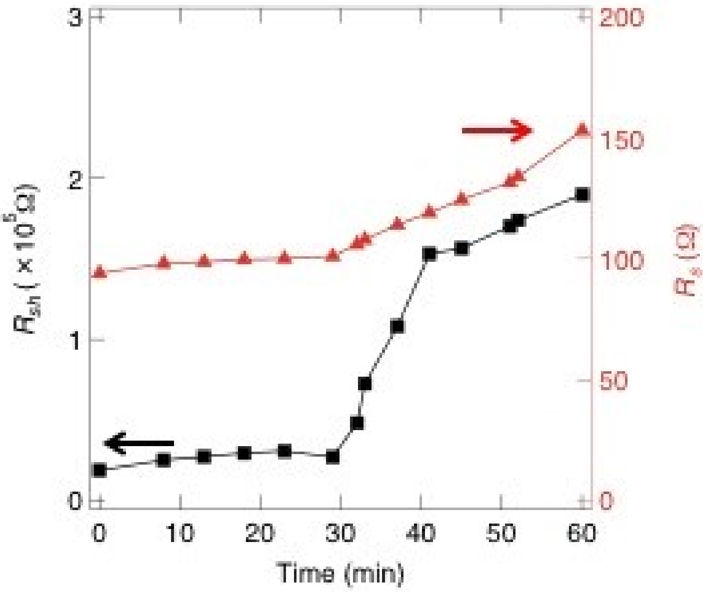

Fig. 2.10. Time dependent change of series resistance and shunt resistance. N_2 gas introduced at 30 min.

2.4 Conclusion

The current-voltage characteristics of BP-PCBM solar cells were measured subsequent to deposition of Al as a cathode material. The rapid change in the inner structure of OPV cells was revealed as below.

- Even in vacuum, shifts of photovoltaic parameters was observed at 20 min after Al deposition (aging effect).

- The displacement of N_2 gases (99.998%) in the evaporation chamber enhanced the photovoltaic parameters. The power conversion efficiency was increased 24% over the initial characteristics (from 1.04% to 1.29%). The reason for this change is not yet fully understood, but it can be well explained by the formation of AlO_X.

- The widely V_{OC} shift in this experiment was due to lowering of J_0 induced by high rectification. The lowering of the leakage current by the very thin insulating layer is the promising way to improve the PCE.

2.5 Reference

[1] H. Ishii, K. Sugiyama, E. Ito and K. Seki, *Adv. Mater.*, 8, 11 (1999).

[2] C. Zhang, S. Tong, C. Zhu, C. Jiang, E. Kang and D. Chan, *Appl. Phys. Lett*,. 94, 103305 (2009).

[3] A. Hayakawa, O. Yoshikawa, T. Fujieda, K. Uehara and S. Yoshikawa, *Appl. Phys. Lett.*, 90, 163517 (2007).

[4] Y. Kinoshita, R. Takenaka and H. Murata, *Appl. Phys. Lett.*, 92, 243309 (2008).

[5] K. Sarangerel, C. Ganzorig, M. Fujihira, M. Sakomura and K. Ueda, *Chem. Lett.*, 37, 778 (2008).

[6] F. Zhang, M. Ceder and O. Inganäs, *Adv. Mater.*, 19, 1835–1838 (2007).

[7] S. Yamakawa, K. Tajima and K. Hashimoto, *Org. Electron.*, 10, 511– 514 (2009).

[8] C. Brabec, S. Shaheen, C. Winder, N. Sariciftci, P. Denk, *Appl. Phys. Lett.*, 80, 1288 (2002).

[9] SI. Na, SH. Oh, SS. Kim and DY. Kim, *Org. Electron.*, 10, 496–500 (2009).

[10] N. Karst and J. C. Bernède, *phys. stat. sol. (a)*, 203, R70– R72 (2006).

[11] Q. L. Song, M. L. Wang, E. G. Obbard, X. Y. Sun, X. M. Ding, X. Y. Hou, C. M. Li, *Appl. Phys. Lett.*, 89, 251118 (2006).

[12] K. Kawano, R. Pacios, D. Poplavskyy, J. Nelson, D. C. Bradley, J. R. Durrant, *Sol. Ene. Mater. and Sol. Cel.*, 90, 3520-3530 (2006).

[13] Y. Matsuo, Y. Sato, T. Niinomi, I. Soga, H. Tanaka and E. Nakamura, *J. Am. Chem. Soc.*, 131, 16048–16050 (2009).

[14] J. C. Bernede, *J. Chil. Chem. Soc.*, 53, Nº3 (2008).

[15] A. Moliton and J. Nunzi, *Polym. Int.*, 55, 583–600 (2006).

[16] E. Ahlswede, J. Hanisch, and M. Powalla, *Appl. Phys. Lett.*, 90, 163504 (2007).

[17] M. Vogel, S. Doka, Ch. Breyer, M. Ch. Lux-Steiner, and K. Fostiropoulos, *Appl. Phys. Lett.*, 89, 163501 (2006).

[18] P. Vivo, J. Jukola, M. Ojala, V. Chukharev and H. Lemmetyinen, *Sol. Energy Mater. Sol. Cells*, 92, 1416 (2008).

3. Evaluation of Vacuum Deposited Benzoporphycene Thin Film as Photoactive Layer

3.1 Introduction

Porphyrinoids such as phthalocyanines and porphyrins have attracted considerable attention as active materials for organic electronic devices including organic light emitting diodes, organic field-effect transistors and organic solar cells because they possess excellent optical and electrical properties.[1–8] In particular, porphyrinoids have been widely investigated as the photoactive materials for organic photovoltaic (OPV) cells. The first OPV cells were fabricated with porphyrins.[9] C. W. Tang also used phthalocyanine to construct first *pn* bilayer devices.[10] Recently, Hori *et. al* have been synthesized 1,4,8,11,15,18,22,25-octahexylphthalocyanine and reported that the OPV cells utilizing the phthalocyanine showed 3.1% PCE.[11,12] The OPV cells utilizing zinc-phthalocyanine and benzoporphyrin (BP) with optimized structure showed 4.08% and 5.20%, respectively.[13, 14] Thus, porphynoids are a promising material for OPV cells.

Benzoporphycene (BPc) (Fig. 3.1) is a constitutional isomer of BP with two direct bonds between neighboring isoindoles and two ethenyl bridges. Compared with BP, BPc has low symmetry and displays broad absorption bands in the visible region, so it is considered suitable for use in OPV cells. In this chapter, we investigated the potential of BPc film as photoactive layer by using vacuum deposited BPc film.

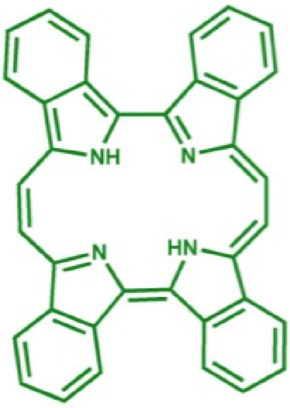

Fig. 3.1. Molecular strucuture of BPc.

3.2 Experimental

The procedure used to synthesize BPc has been reported elsewhere.[15)] A layer of poly(3,4-ethylenedioxythiophene):poly(styrenesulfonate) (PEDOT:PSS) with a thickness of 30 nm was deposited by spin-coating at 3000 rpm from an aqueous solution (Baytron P VP AI 4083) on the top of a glass substrate patterned with indium tin oxide (ITO) layer. The layer was then annealed at 135 °C for 10 min. A BPc film was deposited at a rate of 0.03 nm/sec on the ITO/PEDOT:PSS substrate. The optical properties of the films were characterized using an ultraviolet-visible (UV-vis) absorption spectrometer (JASCO, V-670). Morphologies of films were observed by atomic force microscopy (AFM, Seiko Instruments, SPI 3800N). The θ–2θ profiling for BPc powder and the films was performed using the RINT 2000 series (Rigaku Co.) and Super Lab (Rigaku Co.), respectively.

Each OPV cell has common structure as follows: ITO/PEDOT:PSS (30 nm)/BPc/PCBM (30 nm)/LiF (0.5 nm)/Al (60 nm). A PCBM layer (30 nm) was spin-coated from a 1% (w/w) PCBM-toluene solution at 1500 rpm onto each former substrate. LiF was vacuum deposited at a rate of 0.1 nm/min, and then Al was vacuum-deposited at a rate of 0.1 nm/sec as an opposite electrode. The current-voltage (J-V) characteristics of the OPV cells were measured in air under a 100 mW/cm^2 light illumination (AM 1.5) at room temperature, without encapsulation of the devices.

3.3 Result and discussion

UV-vis absorption spectra of vacuum-deposited BPc film are presented in Figure 3.2. The absorption spectrum of BPc film exhibited a Soret band around at 450 nm and Q-band between 550 and 750 nm. BPc had broad absorption band from 360 to 750 nm. Compared with BP,[16)] BPc displayed broad absorption bands in the visible region, so it is considered suitable for use in OPV cells. The spectra of PCBM, which are commonly used *n*-type semiconductor in OPV cells, were also shown in Fig. 3.2. PCBM has the absorption peak at 350 nm and fill the gap in the visible region.

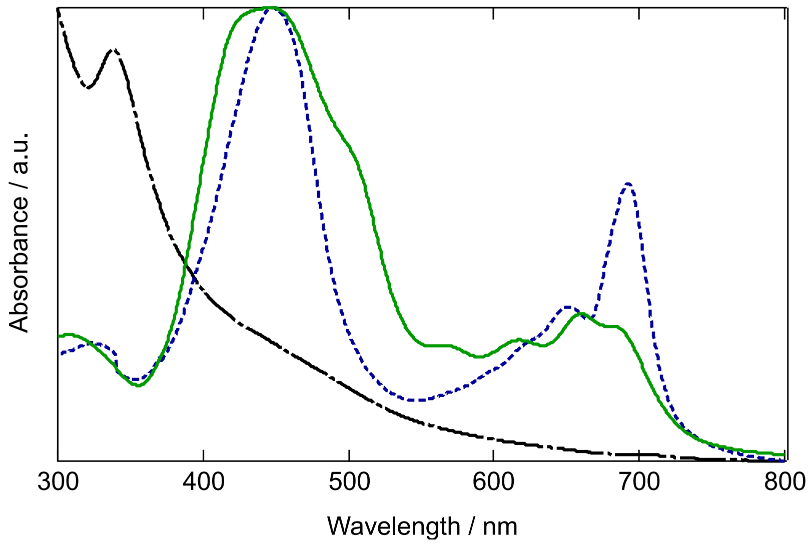

Fig. 3.2. UV-vis absorption spectra of BPc (solid), BP(dotted) and PCBM (broken) on ITO/PEDOT:PSS substrate.

Figures 3.3 (a) ~ (d) depicts the AFM image of BPc films with varying thickness. In each AFM images of BPc films, 100-nm-width grains were observed uniformly. In the AFM image of 40-nm-thick BPc film, the texture of underlying ITO was clearly observed. With increasing of film thickness, the texture was disappeared. In the AFM image of 80-nm-thick BPc film, the texture of ITO was almost disappeared and fully covered with BPc grains.

Figure 3.4 shows the XRD pattern of BPc powder and the vacuum-deposited films. The lattice constants of the compound are a = 5.536 Å, b = 14.502 Å, c = 14.754 Å, α = 98.633°, β = 91.079°, γ = 96.534° (triclinic).17) BPc took herringbone packing in the crystal (Fig. 3.5(a)). From these lattice constants and calculated intensity, the diffraction peaks were assigned as shown in Fig 3.4. The XRD pattern of the each vacuum deposited BPc film showed diffraction peaks at 2θ = 6.1 and 12.2°, which is corresponded to 010 and 020 reflection of BPc crystal. Another reflection of the BPc crystal was not observed. This indicates that the a-c plane of the BPc crystal is parallel to the substrate surface and BPc molecules take the edge-on orientation (Fig. 3.5(b)).

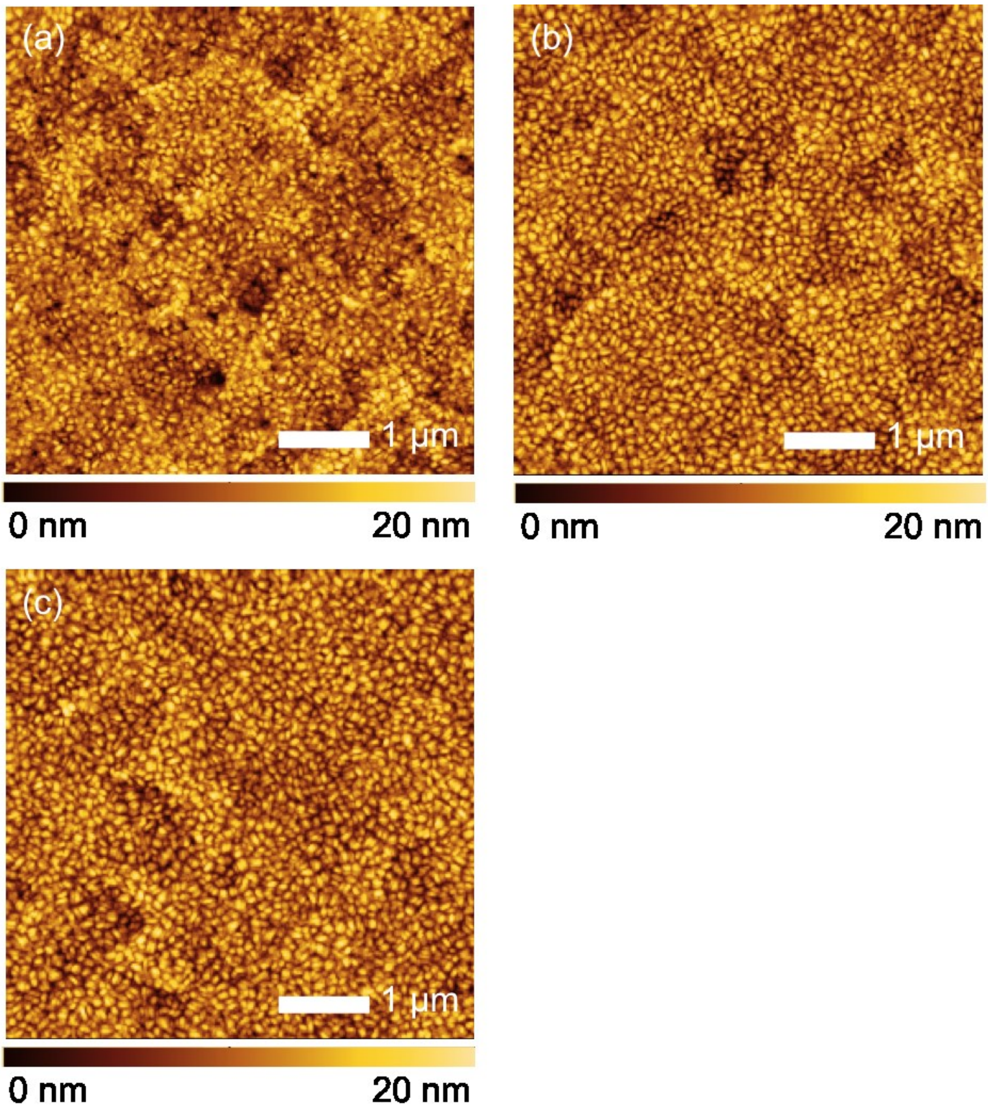

Fig. 3.3. AFM image of the vacuum-deposited BPc film (a) 40 nm (b) 60 nm (c) 80 nm.

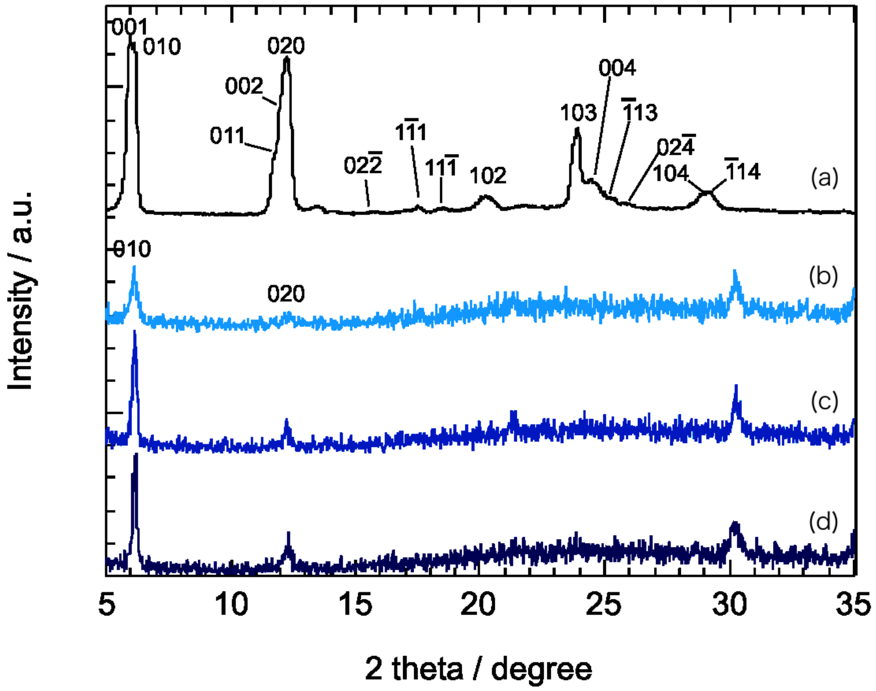

Fig. 3.4. XRD pattern of BPc powder (a), and BPc films (b) 40 nm (c) 60 nm (d) 80 nm.

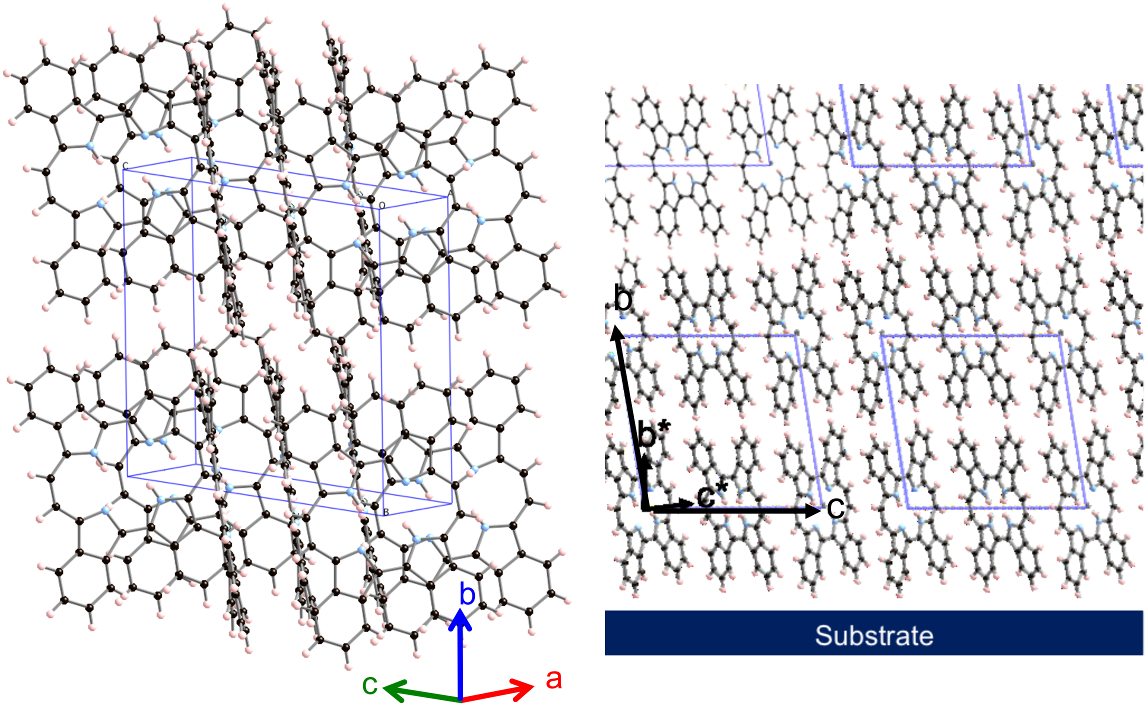

Fig. 3.5. (a) Schematic view of BPc crystal. (b) Orientation of BPc crystal on ITO/PEDOT:PSS substrate.

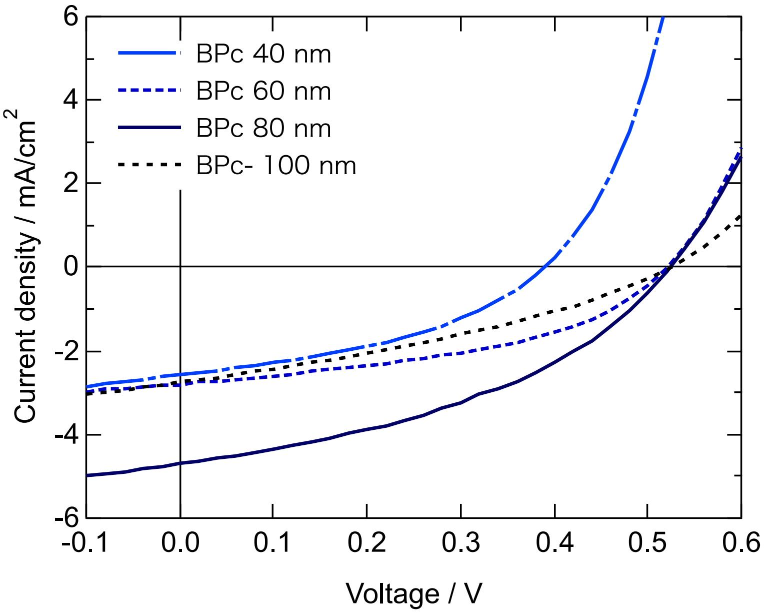

Fig. 3.6. *J-V* curves measured for cells utilizing vacuum deposited BPc films.

OPV cells were fabricated using the vacuum deposited BPc thin film as an active layer. *J-V* curves obtained under illumination are presented in Fig. 3.6, and device performances are summarized in Table 3.1. Cell utilizing 40-nm-thick BPc film showed low open circuit voltage (V_{OC}) due to the thin BPc layer. The photovoltaic parameters are as follows. The $\mathrm{V_{OC}}$, short circuit current density (J_{SC}) and fill factor (*FF*) were 0.39 V, 2.57 mA/cm^2 and 0.40, respectively, and its resulting PCE was 0.40%. The cell utilizing 60-nm, 80-nm, and 100-nm thick BPc films showed same V_{OC}, 0.52 V. These result indicates that the BPc grains fully cover the PEDOT:PSS substrate by deposition of over 60-nm-thick BPc film. The V_{OC} can be estimate from the highest occupied molecular orbital (HOMO) level of donor material and lowest unoccupied molecular orbital (LUMO) level of acceptor material.18) The HOMO level of BPc was also determined at 5.1 eV by PYS measurement. The V_{OC} of the cells utilizing BPc and PCBM (LUMO = 4.2eV19)) is expected at 0.6 V. Therefore, the results of *J-V* curves and PYS measurement validates each other. As increasing of film thickness from 60 nm to 80 nm, the J_{SC} increased. But the cell utilizing 100-nm thick BPc showed low J_{SC}, 2.73 mA/cm^2. The optimized thickness of BPc was 80 nm and its resulting PCE was at 0.99%. Though the cells had *pn* planar structure and fabrication process were carried out in ambient condition, the PCE reached about 1%. The BPc can be expected as a candidate of photoactive layer in OPV cell.

Table 3.1. Photovoltaic parameters.

Thickness of BPc film	J_{SC} (mA/cm^2)	V_{OC} (V)	FF (-)	R_s (Ω)	R_{sh} (Ω)	PCE (%)
40 nm	2.57	0.39	0.40	20	33	0.40
60 nm	2.80	0.52	0.43	91	1.0×10^5□	0.61
80 nm	4.70	0.52	0.40	98	1.0×10^5□	0.99
100 nm	2.73	0.52	0.34	112	4.3×10^5□	0.48

3.4 Conclusion

The morphology and photovoltaic properties of vacuum deposited film were evaluated. The findings were as below.

- BPc displayed broad absorption band from 360 nm to 750 nm, so it is considered suitable for use in OPV cells.

- Only 010 and 020 reflections were observed in XRD profiles for vacuum deposited BPc film. BPc molecules took only edge-on orientation in the vacuum deposited film.

- The HOMO level of BPc was determined at 5.1 eV

- The OPV cell utilizing vacuum deposited BPc film showed nearly 1% PCE. The BPc can be expected as a candidate of photoactive layer in OPV cell.

3.5 Reference

[1] G. de la Torre, C. G. Claessens, and T. Torres, *Chem Commun.*, 2000 (2007).

[2] C. W. Tang, *Appl. Phys. Lett.*, 48, 183 (1986).

[3] Z. Bao, A. J. Lovinger, and A. Dodabalapur, *Appl. Phys. Lett.*, 69, 3066 (1996).

[4] J. H. Lee, C. C. Liao, P-J. Hu, and Y. Chang, *Synth. Metals*, 144, 279 (2004).

[5] D. Wohrle and D. Meissner, *Adv. Mater.*, 3, 129 (1991).

[6] A. Key and M. Graetzel, *J. Phys. Chem.* 97, 6272 (1993).

[7] D. Gust, T. A. Moore, and A. L. Moore, *Acc. Chem. Res.*, 34, 40 (2001).

[8] A. R. Murphy and J. M. J. Frechet, *Chem. Rev.*, 107 1066 (2007).

[9] D. Kearns, M. Calvin, *J. Chem. Phys.* 29, 950 (1958).

[10] C. W. Tang, *Appl. Phys. Lett.*, 48, 183 (1986).

[11] T. Hori, Y. Miyake, N. Yamasaki, H. Yoshida, A. Fujii, Y.Shimizu, M. Ozaki, *Appl. Phys. Express*, 3, 101602 (2010).

[12] T. Hori, N. Fukuoka, T. Masuda, Y. Miyake, H. Yoshida, A. Fujii, Y. Shimizu, M. Ozaki, *Sol. Ener. Mater. and Sol. Cells*, 95, 3087 (2011).

[13] Y. Zhou, T. Taima, T. Miyadera, T. Yamanari, M. Kitamura, K. Nakatsu, Y. Yoshida, *Nano Lett.*, 12, 4146 (2012).

[14] Y. Matsuo, Y. Sato, T. Niinomi, I. Soga, H. Tanaka, E. Nakamura, *J. Am. Chem. Soc.*, 131, 16048 (2009).

[15] D. Kuzuhara, J. Mack, H. Yamada, T. Okujima, N. Ono, and N. Kobayashi, *Chem. Eur. J.* **15** (2009) 10060.

[16] S. Aramaki, Y. Sakai, R. Yoshiyama, K. Sugiyama, N. Ono, and J. Mizuguchi, *Proc.of SPIE.*, Vol.5522, 27 (2004).

[17] D. Kuzuhara, H. Yamada, S. Mori, T. Okujima, and H. Uno, *J. Porphyrins Phthalocyanines* **15** (2011) 931.

[18] M. C. Scharber, D. Muhlbacher, M. Koppe, P. Denck, C. Waldauf, A. J. Heeger, and C. J. Brabec, *Adv. Mater.*, 18, 789 (2006).

[19] C. Winder, D. Muhlbancher, H. Neugebauser, N. S. Sariciftci, C. Brabec, R. Janssen, and J. K. Hummelen, *Mol. Cryst. & Liq. Cryst.*, 385, 93 (2002).

4. Fabrication of Phase-separated Benzoporphycene/[6,6]-Phenyl-C_{61}-Butyric Acid Methyl Ester Films for Use in Organic Photovoltaic Cells

4.1 Introduction

In chapter 3, vacuum deposited benzoporphycene (BPc) thin film was evaluated as a photoactive layer. The BPc film showed broad absorption and good photovoltaic properties. However, macrocyclic π-conjugated molecules including BPc generally have low solubility in common solvents. It makes difficult to adopt to wet processes, facilitate processing and allow low-cost fabrication. To overcome this problem, soluble photo- or thermo-convertible precursors with bulky substituents have been synthesized.1-5) There have been several reports on the conversion behavior of soluble precursors and the electric properties of the organic compounds formed after conversion.6-11) Afzali *et al.*5) reported that OFETs containing pentacene prepared from a thermo-convertible precursor show a high field-effect mobility of ~0.89 $cm^2 V^{-1} s^{-1}$. Matsuo *et al.*12) fabricated organic photovoltaic (OPV) cells using a benzoporphyrin (BP) precursor that exhibit a high power conversion efficiency (PCE) of 5.2%. To use BPc in a wet process, Kuzuhara and Yamada in NAIST prepared a thermo-convertible BPc precursor (BPc-pre) with bulky substituents as same as benzoporphyrin precursor, as shown in Fig. 4.1.13)

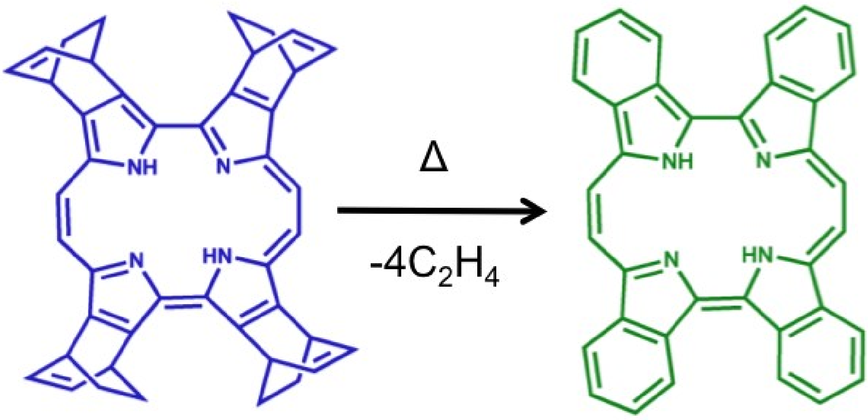

Fig. 4.1. Reaction scheme of BPc-pre to BPc.

In this chapter, the thermal conversion behavior, crystal growth of BPc from the soluble precursor in the film and the effect of coexistence with [6,6]-phenyl-C_{61}-butyric acid methyl ester (PCBM) on film morphology were investigated. Moreover, the thickness of BPc films was increased by alternating between spin-coating of BPc-pre/PCBM solution and annealing, and then the structure of the resulting films was investigated. The BPc films were also evaluated as the photoactive layer in

OPV cells.

4.2 Experimental

4.2.1 Preparation and evaluation of BPc film and BPc/PCBM mixture film

The procedure used to synthesize BPc-pre has been reported elsewhere.13) Dichloromethane is a good solvent for BPc-pre, dissolving in it to give a saturated concentration of 0.15% (w/w). A layer of poly(3,4-ethylenedioxythiophene):poly(styrenesulfonate) (PEDOT:PSS) with a thickness of 30 nm was deposited by spin-coating from an aqueous solution on the top of a glass substrate patterned with indium tin oxide (ITO) layers. The layer was then annealed at 135 °C for 10 min. A BPc-pre film was spin-coated on the ITO/PEDOT:PSS substrate using saturated dichloromethane solution. To prepare a BPc-pre/PCBM mixed film, PCBM was added to the saturated dichloromethane solution of BPc-pre. The molar ratio of BPc-pre to PCBM was fixed at 1:1. Annealing to cause thermal conversion was performed at various temperatures under atmospheric conditions. The structural change from BPc-pre to BPc was confirmed using infrared (IR) spectroscopy (Jasco, FT/IR-660 Plus). Thermogravimetric analysis (TGA) was carried out using a thermogravimetric analyzer (VAP-9000, Ulvac Riko). The optical properties of the films were characterized using an ultraviolet-visible (UV-vis) absorption spectrometer (ALS, SEC-2000). Morphologies of films were observed by atomic force microscopy (AFM, Seiko Instruments, SPI 3800N) and field emission scanning electron microscopy (FE-SEM, Jeol, JSM-7500F). Electron diffraction patterns of the films were recorded at an acceleration voltage of 100 kV by transmission electron microscopy (TEM, Hitachi H-7100).

4.2.2 Fabrication and characterization of OPV cells

In this study, three kinds of OPV cells were fabricated. Cell (I)–(III) had the following common structure: ITO/PEDOT:PSS (30 nm)/ [BPc/PCBM mixed layer] /PCBM (30 nm)/LiF (0.5 nm)/Al (60 nm). The BPc/PCBM mixed layer of cell (I) was fabricated by spin-coating a BPc-pre/PCBM mixed solution onto an ITO/PEDOT:PSS substrate and then heating it at 200 °C for 10 min. The photoactive layer of cell (II) was fabricated by alternating between spin-coating and heating at 200 °C for 10 min for five cycles. For the photoactive layer of cell (III), the same method as that to prepare cell (II) was used, except that annealing was performed at 250 °C for 1 min. A PCBM layer (30 nm) was fabricated in each cell by spin-coating from a toluene solution. LiF (0.5 nm) and aluminum (60 nm) were deposited as a cathode at a base pressure of 5×10^{-4} Pa with deposition rates of 0.01 nm/min and 0.1 nm/sec, respectively. The light flux was set AM 1.5 sunlight illumination, produced with a filtered Xe-lamp in a solar simulator. The measurements in this chapter were carried out in air at room temperature, without encapsulation of the devices.

4.3 Result and discussion

Figure 4.2 shows the TG analysis curve for BPc-pre powder obtained at a heating rate of 10 °C / min in a nitrogen atmosphere. When BPc-pre powder was annealed, a weight loss was observed over the temperature range from 125 to 210 °C. Total weight loss was 18.8%, which was consistent with the loss of four ethylene groups by retro-Diels-Alder reaction at the four bicyclo moieties. The color of BPc-pre powder changed from light blue to light green by annealing.

Figure 4.3 shows the IR spectra of an as-spun BPc-pre film and that of a BPc-pre film annealed at 200 °C for 10 min. Both spectra showed bands at around 1023, 1080, 1339, 1532, 1558, 1607 $\mathrm{cm^{-1}}$ that are derived from the vibration modes of δ C-H (alkene), ν C-N (pyrrole), ν C-N (pyrrole), ν C=C (pyrrole), ν C=C (pyrrole) and ν C=C (alkene), respectively. These are the distinguishing bands of porphycene rings. After annealing, absorption bands at 722, 1463, 2865 and 2937 $\mathrm{cm^{-1}}$ disappeared, and now ones appeared at 734, 888, 1446 and 1602 $\mathrm{cm^{-1}}$. The former bands are assigned as δ_s C -H, δ_{as} C-H, ν_s C-H and ν_{as} C-H of an alkane, respectively, while the latter are the vibration modes of δ C-H, δ C-H, ν C=C and ν C=C of benzene rings, respectively. These changes indicate that the bicyclo structure on the outer side of the porphycene ring converts into a benzene ring, so BPc-pre is converted into BPc by annealing.

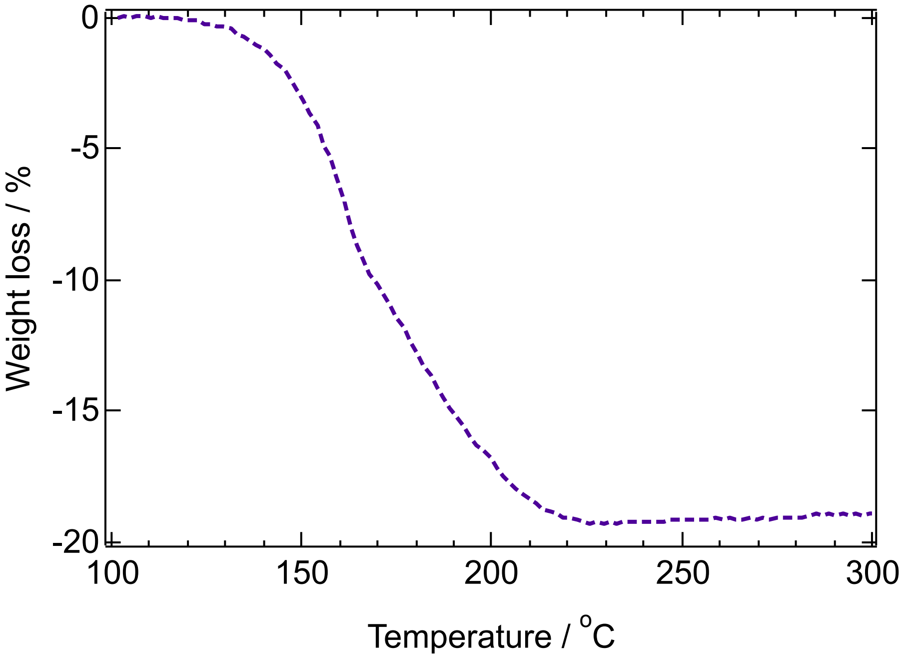

Fig. 4.2. TG analysis curve of BPc-pre.

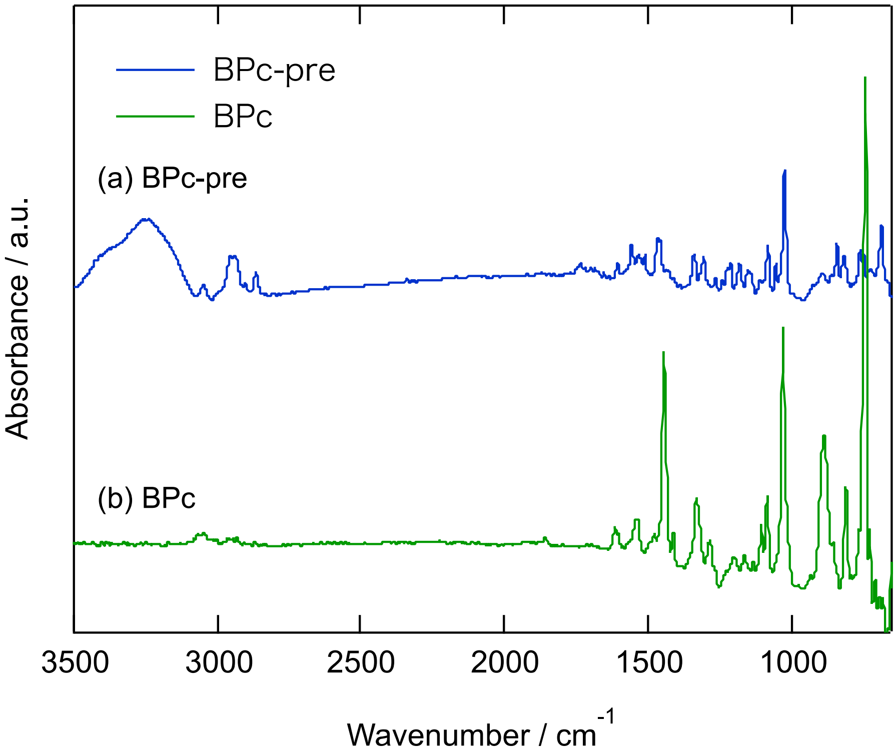

Fig. 4.3. IR spectrum of (a) as-spun BPc-pre film and (b) BPc-pre film after annealing at 200 °C for 10 min.

UV-vis absorption spectra of a BPc-pre film before and after annealing at 200 °C for 10 min, together with that of a 35-nm-thick BPc film that was vacuum-deposited on an ITO/PEDOT:PSS substrate are presented in Fig. 4.4. The absorption spectrum of the as-spun BPc-pre film exhibited a Soret band around at 390 nm and Q-band between 550 and 700 nm. After annealing, the Soret band exhibited a red shift to 450 nm, and the Q-band extended to 750 nm. The positions of the absorption peaks of the converted film agreed well with those of the vacuum-deposited film. From the results of TGA, IR and UV-vis measurements, we concluded that the retro-Diels-Alder reaction of BPc-pre was completed by annealing at 200 °C for 10 min.

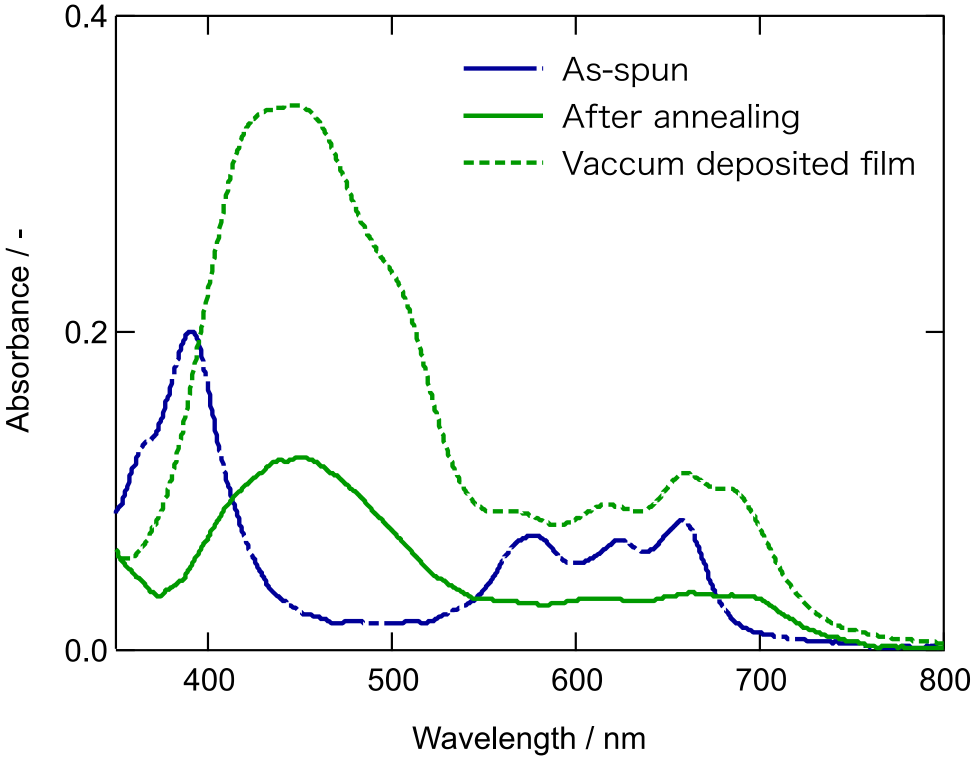

Fig. 4.4. UV-vis absorption spectrum of as-spun BPc-pre film, BPc-pre film after annealing at 200 °C for 10 min, and vacuum-deposited BPc film.

Figure 4.5(a) and (b) depict AFM images of the as-spun BPc-pre film and the same film after annealing at 200 °C for 10 min (*i.e.*, a BPc film), respectively. The as-spun BPc-pre film was composed of a 20-nm-thick smooth layer. In contrast, discrete particles with a height of over 100 nm were observed after annealing. When the BPc-pre film was converted, a continuous BPc layer was not obtained even when annealing conditions such as temperature (170–250 °C) and interval were varied. An AFM image of a BPc/PCBM film converted at 200 °C for 10 min is illustrated in Fig. 4.6(a). The BPc/PCBM film was a continuous layer with a smooth surface (RMS roughness ~1.8 nm). After conversion, the surface roughness of the film improved considerably compared with that of the BPc-only film. A high resolution electron diffraction (HRED) pattern of the BPc/PCBM film obtained over an area with a diameter of 150 μm showed the superposition of patterns from both a BPc crystal (triclinic, a = 5.536 Å, b = 14.502 Å, c = 14.754 Å, α = 98.633°, β = 91.079°, γ = 96.534°)[14] and a PCBM crystal (monoclinic, a = 10.274 Å, b = 19.101 Å, c = 19.342 Å, β = 91.616°)[15], as shown in Fig. 4.6(c). The diffraction pattern of BPc coincided to the pattern projected along the b*-axis of a BPc crystal. BPc crystals oriented uniaxially to the substrate surface but with random in-plane. Conversely, the diffraction spots from PCBM were indexed as 210, 012, and 021 reflections. The orientation of PCBM crystals was random. To clarify the film structure, a dichloromethane solution was spin-coated on the BPc/PCBM film, repeatedly. After rinsing, discrete laminar crystals that were <1 μm wide and 20 nm high were clearly observed, as illustrated in Fig. 4.6(b). An HRED pattern of the film after rinsing showed only the diffraction rings from a BPc

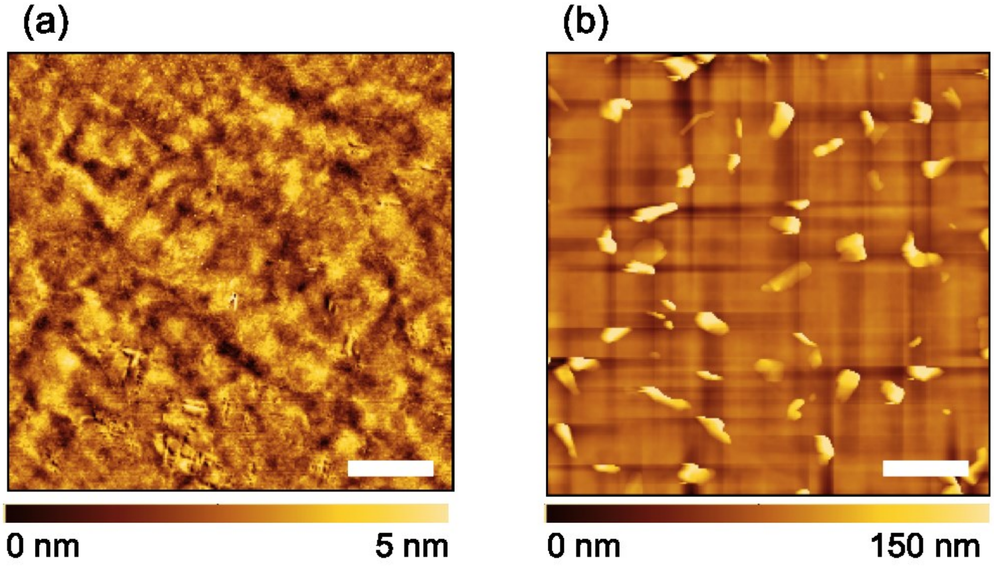

Fig. 4.5. AFM image of (a) as-spun BPc-pre film, (b) BPc-pre film after annealing for 10 min (*i.e.*, BPc film). (scale bar: 1 μm).

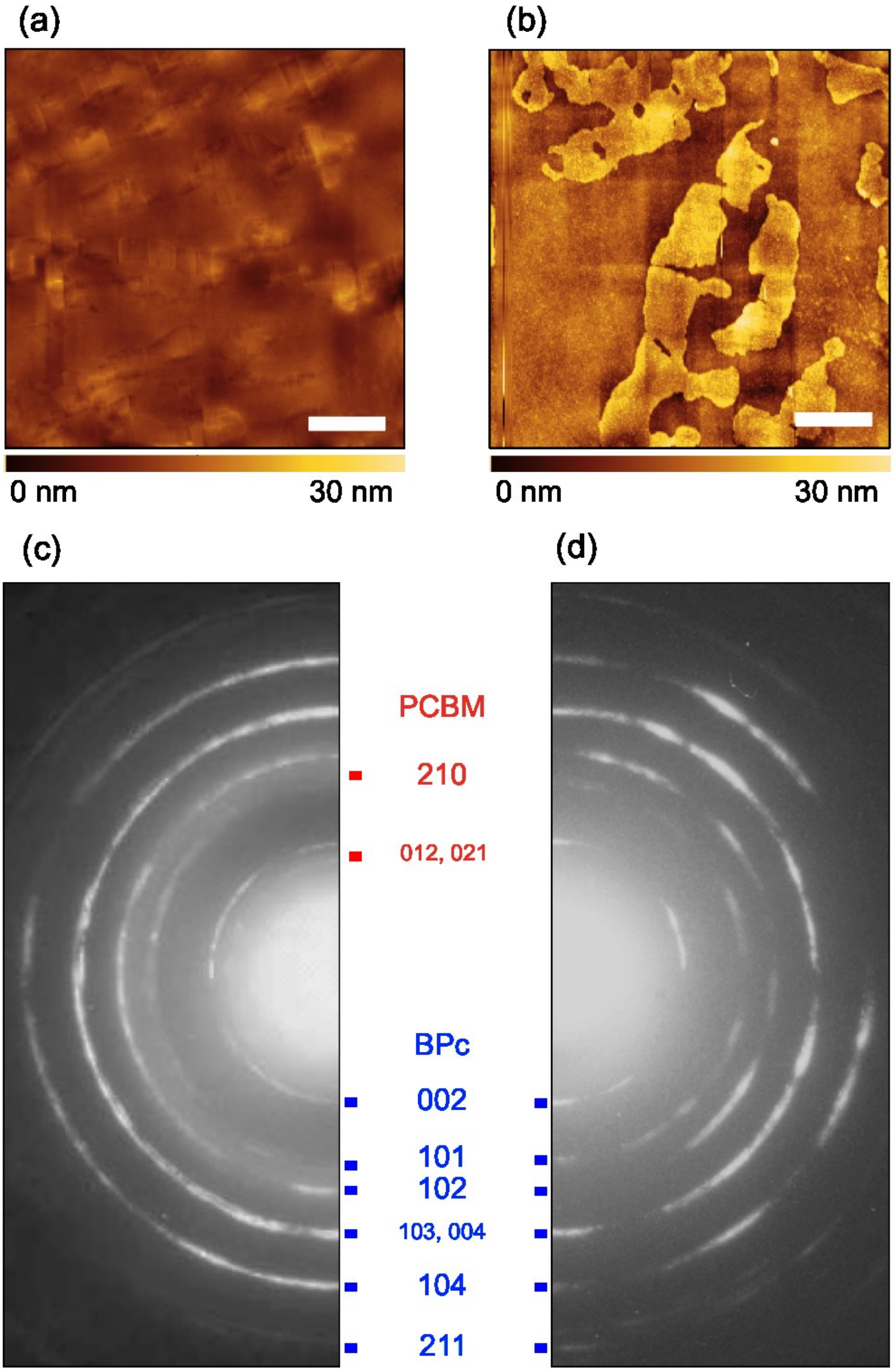

Fig. 4.6. AFM image and HRED pattern of BPc/PCBM film converted at 200 °C for 10 min [(a), (b)], and those of a BPc/PCBM film rinsed with dichloromethane [(c), (d)] (scale bar: 1 μm).

crystal (Fig. 4.6(d)). Although PCBM crystals were dissolved by rinsing with dicholormethane, the BPc crystals remained tightly adsorbed onto the substrate surface. BPc molecules crystallized on the substrate surface and grew two-dimensionally because of strong molecular cohesion with edge-on orientation, resulting in the formation of laminar crystals of BPc. It appears that PCBM in the film acts as a matrix during the crystallization of BPc. In examining the effect of the matrix, poly[2-methoxy-5-(2-ethylhexyloxy)-1,4-phenylenevinylene] (MEH-PPV) was blended with BPc-pre as a polymer matrix instead of PCBM. Figure 4.7 shows the optical micrograph of BPc-pre/MEH-PPV film after annealing under the same conditions. BPc crystallized discretely to form grains over 100 nm in height, which were quite similar to those formed from the BPc-pre film, although MEH-PPV remained amorphous. Therefore, we concluded that PCBM crystals formed by annealing suppress surface diffusion and the subsequent aggregation of BPc, resulting in the formation of a smooth and phase-separated BPc/PCBM film (Fig. 4.8).

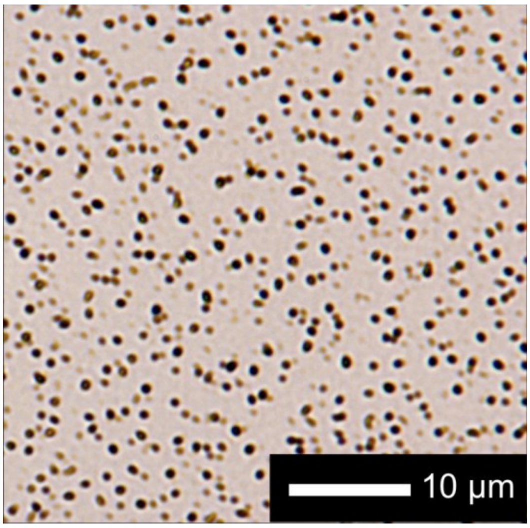

Fig. 4.7. Optical micrograph of BPc/MEH-PPV film converted at 200 °C for 10 min.

When a BPc-pre/PCBM mixed solution was over-coated on a BPc-pre/PCBM film, the initial BPc-pre/PCBM film dissolved and a fresh film of same thickness formed. As a result, film stacking by multi spin-coating steps was difficult. Thicker films could be formed by alternating between

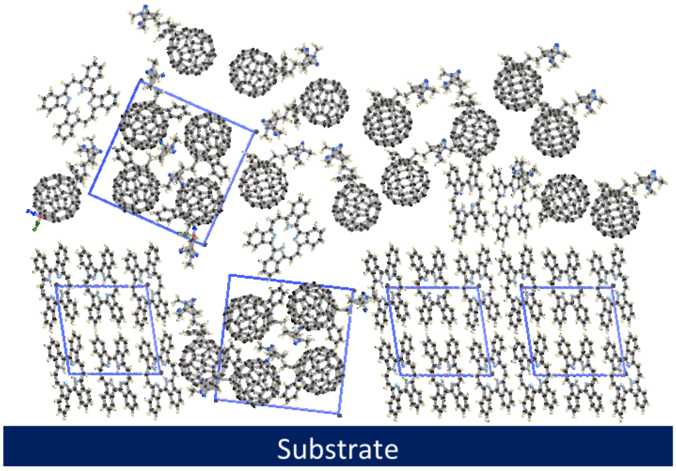

Fig. 4.8. Schematic image of the BPc/PCBM film.

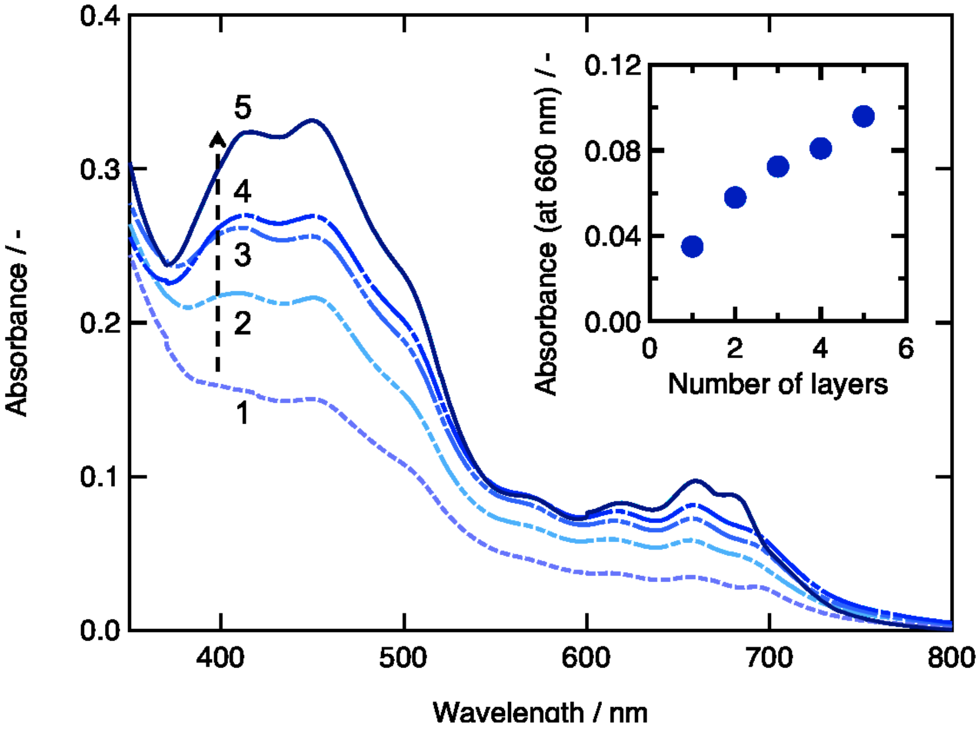

Fig. 4.9. UV-vis absorption spectra of multi-stacked BPc/PCBM films. The inset shows the dependence of absorbance at 660 nm on the number of alternating spin-coating/annealing cycles.

spin-coating BPc-pre/PCBM solution and annealing. UV-vis absorption spectra of multi-stacked BPc/PCBM films are presented in Fig. 4.9. In the wavelength region below 550 nm, the absorbance of a single layer of BPc/PCBM was larger than that of a BPc film converted from BPc-pre alone (Fig. 4.4) because its absorption overlapped with that of PCBM.16) In contrast, in the wavelength region from 550 to 800 nm, the absorbance of a single layer of BPc/PCBM was almost comparable to that of a BPc film converted from BPc-pre alone. The absorbance at 660 nm increased proportionally with the number of spin-coating and subsequent annealing cycles, as shown in the inset of Fig. 4.9. This indicates that each layer was almost the same thickness, and that BPc in the underlying layer was not dissolved.

Figure 4.10(a) shows an FE-SEM image of a BPc/PCBM film with five layers. The film surface before rinsing was very smooth and similar to that of the single-layer BPc/PCBM film shown in Fig. 4.6(c). After rinsing, many tabular BPc grains about 1 μm wide and several micrometers long were observed (Fig. 4.10(b)). Careful observation of individual grains revealed that the long axis of the crystal in the upper layer was aligned parallel to that of the crystal in the lower layer, as indicated by arrows. A selected area electron diffraction (SAED) pattern of the tabular crystal indicated by the circle corresponds to a single net pattern projected along the b*-axis of a BPc crystal (Fig. 4.10(c)). This indicates that BPc converted from BPc-pre crystallized homoepitaxially on the underlying BPc crystals in each deposition process, as shown in Fig. 4.10(d). A cross-sectional image of the BPc/PCBM film with five layers after rinsing is depicted in Fig. 4.11. A BPc layer with a thickness of 20 nm was clearly observed. The highest grain had a height of about 100 nm, which is good agreement with five times the height of a single layer of BPc grains. The cross-sectional SEM image confirms that the thickness of BPc can be increased by repeated spin-coating/annealing cycles.

The homoepitaxial crystallization of BPc can be explained as follows. BPc-pre was thermally converted to BPc in the BPc-pre/PCBM blend film, and BPc and PCBM crystallized individually to form a phase-separated structure. When a BPc-pre/PCBM mixed layer was spin-coated on top of a phase-separated BPc/PCBM film, PCBM crystals were partially dissolved by dichloromethane, but BPc crystals were not. As a result, as amorphous layer of BPc-pre/PCBM formed on the discontinuous crystalline BPc film. Upon annealing, BPc-pre was converted to BPc, which then

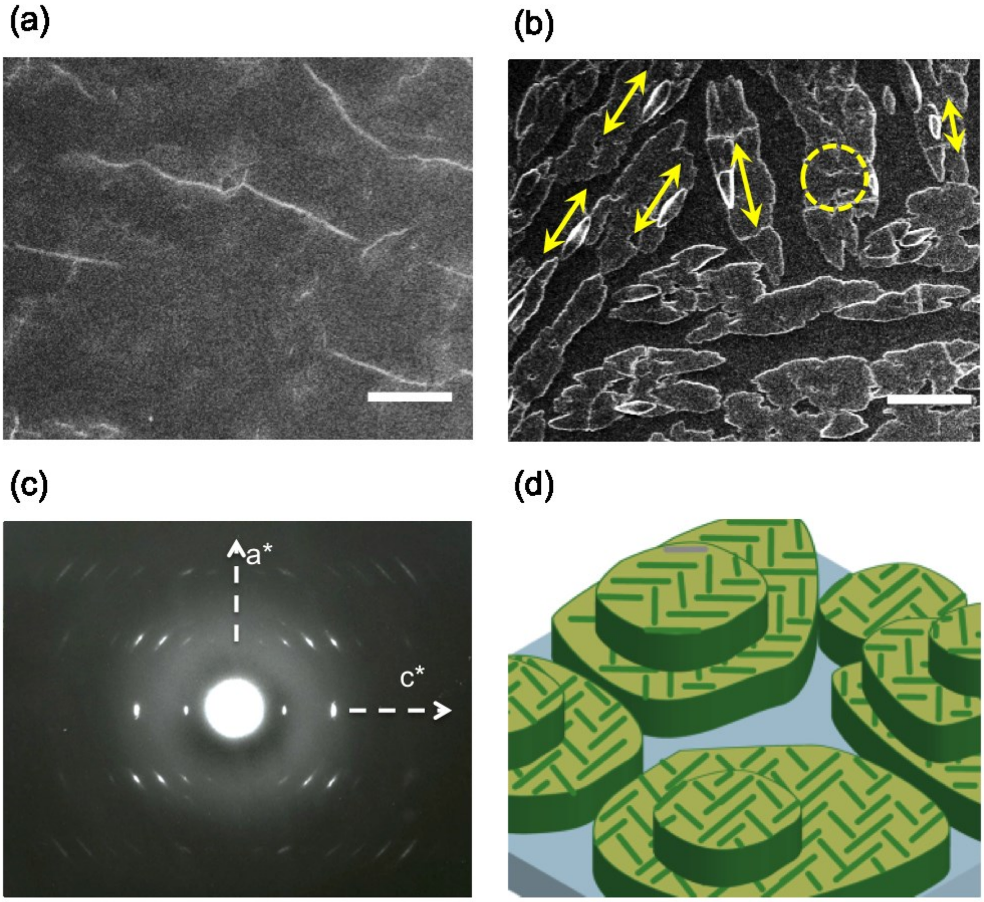

Fig. 4.10. Topological SEM image of a BPc/PCBM film containing five layers prepared at 200 °C: (a) as-prepared, and (b) after rinsing. (c) SAED pattern of the area indicated by a circle, and (d) schematic representations of the homoepitaxial growth of BPc (scale bar: 1 μm).

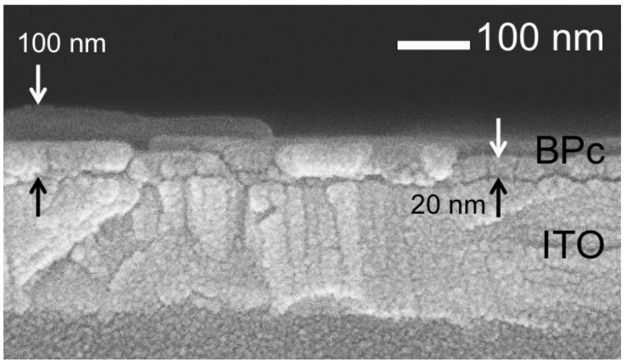

Fig. 4.11. Cross-sectional SEM image of a BPc/PCBM film with five layers after rinsing.

crystallized. The BPc crystals in the underlying layer act as seed crystals. In contrast, a BPc-pre film formed by one spin-coating step was very thin, with the same thickness as the first BPc/PCBM layer.

Therefore, deposited BPc cannot fully cover the underlying BPc crystals. Repetition of the above process forms BPc grains of varying height from 20 to 100 nm, producing a phase-separated, single-crystalline BPc nanostructured thin film.

OPV cells were fabricated using the phase-separated BPc/PCBM thin film as an active layer. *J*-*V* curves obtained in the dark and under illumination are presented in Fig. 4.12(a) and (b), respectively and device performances are summarized in Table 4.1. Cell (I) showed low rectification in the dark and slight photoconversion under illumination. The open circuit voltage (V_{OC}), short circuit current density (J_{SC}) and fill factor (*FF*) of cell (I) were 0.03 V, 0.88 mA/cm^2 and 0.25, respectively, and its resulting PCE was 6.6×10^{-3}%. The photoactive layer of cell (I) was composed of discrete 20-nm-high BPc grains and a 30-nm-thick PCBM film. The thin photoactive layer caused the low rectification and poor photoconversion of this cell.

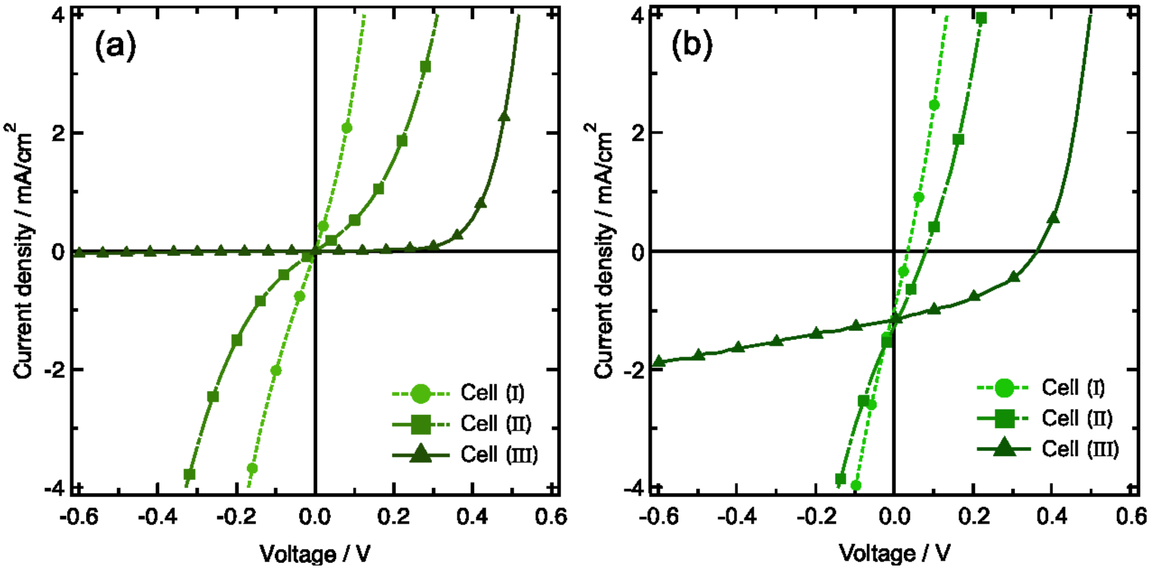

Fig. 4.12. *J*-*V* curves measured for cells (I)–(III) (a) in the dark, and (b) under illumination.

The film stacking by repetition of spin-coating and annealing at 200 °C increased V_{OC} from 0.03 to 0.08 V and J_{SC} from 0.88 to 1.22 mA/cm^2. Although the active layer of cell (II) was five times thicker than that of cell (I), cell (II) also showed poor rectification in the dark and low V_{OC}, with almost the same characteristics as those of cell (I). In contrast, the active layer prepared at 250 °C (cell (III)) exhibited significantly improved rectification and cell performance. The *J*-*V* curve measured in the dark for cell (III) exhibited good diode behavior, and it achieved V_{OC}, J_{SC} and *FF* of 0.36 V, 1.14 mA/cm^2 and 0.40, respectively. These parameters yielded a PCE for cell (III) of 0.16%.

Table 4.1. Photovoltaic parameters of cell (I)–(III).

	Device configuration	J_{SC} (mA/cm^2)	V_{OC} (V)	FF (-)	η (%)
Cell (I)	BPc:PCBM (1:1) 200 °C 10 min	0.88	0.03	0.25	6.6×10^{-3}
Cell (II)	5-layered BPc:PCBM (1:1) 200 °C 10 min	1.20	0.08	0.25	2.4×10^{-2}
Cell (III)	5-layered BPc:PCBM (1:1) 250 °C 1 min	1.14	0.36	0.40	0.16

The photovoltaic properties of these cells heavily depended on thermal conversion conditions. The BPc/PCBM film prepared at higher temperature (250 °C) above the conversion temperature of BPc-pre showed good photovoltaic performance. However, annealing for 10 min at this temperature, which is same period of the annealing condition at 200 °C, caused surface roughening with the coagulation and crystallization of PCBM. However, using a short annealing time prevented surface roughening. Figure 4.13(a) shows an FE-SEM image of a film that was annealed at 250 °C for 1 min and subsequently rinsed. Small grains of BPc 200 ~ 500 nm in size were observed. The grain size was about one-sixth that of BPc crystals annealed at 200 °C. Although the grain size depended on

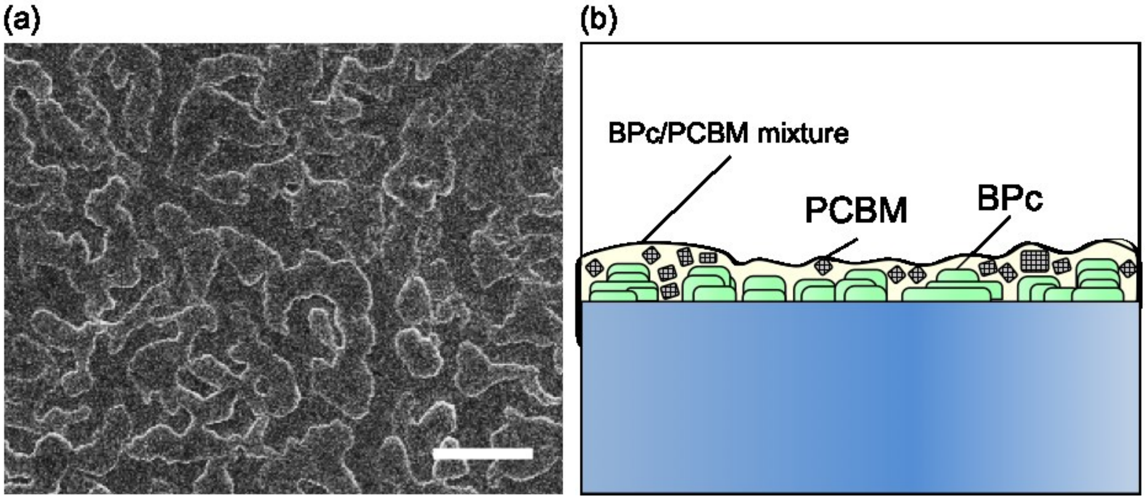

Fig. 4.13. (a) Topological SEM image of a BPc/PCBM film with five layers prepared at 250 °C after rinsing, and (b) the film formation mechanism (scale bar: 1 μm).

annealing conditions, the SAED pattern of each grain showed a similar single net pattern projected along the b*-axis of the BPc crystal, so BPc molecules adopt an edge-on orientation regardless of annealing conditions. Annealing for 1 min was sufficient for conversion of BPc-pre to BPc but inhibited crystal growth because there was less time for migration of converted BPc molecules. Therefore, a fine phase-separated, single-crystalline BPc film formed, as illustrated schematically in Fig. 4.13(b). The miniaturization of grains increased the coverage of BPc on the PEDOT:PSS substrate and reduced the contact area between the PEDOT:PSS anode and PCBM, which is an *n*-type semiconductor. This decreased the leakage current and improved the PCE of cell (III) compared with those of cell (I) and (II).

4.4 Conclusion

We investigated the thermal conversion behavior of BPc-pre and film structure of BPc and BPc/PCBM. The resulting film was evaluated as photoactive layer. The findings were as below.

- BPc-pre had a high cohesive property. A continuous BPc layer was not obtained even when annealing conditions such as temperature (170–250 °C) and interval were varied.

- PCBM crystals dramatically inhibited the aggregation of BPc-pre and BPc, resulting in a phase-separated structure with a flat surface.

- The crystals of BPc converted from BPc-pre oriented uniaxially to the substrate surface with edge-on orientation but with random in-plane.

- BPc converted from BPc-pre crystallized homoepitaxially on the underlying BPc crystals in each deposition process, alternating between spin-coating BPc-pre/PCBM solution and annealing.

- High temperature annealing (*i.e.*, 250 °C) reduced the size of BPc crystals and the contact area between PEDOT:PSS and PCBM. The decreasing the contact caused the leakage current to decrease and PCE to increase. Resulting PCE was 0.16 %.

4.5 Reference

[20] A. R. Brown, A. Pomp, D. M. de Leeuw, D. B. M. Klaassen, E. E. Havinga, P. Herwig, and K. Mullen, *J. Appl. Phys.* **79** (1996) 2136.

[21] S. Ito, T. Murashima, H. Uno and N. Ono, *Chem. Commun.* (1998) 1661.

[22] H. Uno, Y. Yamashita, M. Kikuchi, H. Watanabe, H. Yamada, T. Okujima, T. Ogawa, and N. Ono, *Tetrahedron Lett.* **46** (2005) 1981.

[23] H. Yamada, Y. Yamashita, M. Kikuchi, H. Watanabe, T. Okujima, H. Uno, T. Ogawa, K. Ohara and N. Ono, *Chem. Eur. J,* **11** (2005) 6212.

[24] A. Afzali, C. D. Dimitrakopoulos, and T. L. Breen, *J. Am. Chem. Soc.* **124** (2002) 8812.

[25] S. Aramaki, Y. Sakai, and N. Ono, *Appl. Phys. Lett.* **84** (2004) 2085.

[26] H. Yamada, T. Okujima, and N. Ono, *Chem. Commun.* (2008) 2957.

[27] N. Noguchi, S. Junwei, H. Asatani, and M. Matsuoka, *Cryst. Growth and Design* **10** (2010) 1848.

[28] S.-Y. Ku, C. D. Liman, J. E. Cochran, M. F. Toney, M. L. Chabinyc, and C. J. Hawker, *Adv. Mater.* **23** (2011) 2289.

[29] M. Guide, X.-D. Dang, and T.-Q. Nguyen, *Adv. Mater.* **23** (2011) 2313.

[30] Y. Murai, M. Misaki, K. Ishida, and Y. Ueda, *App. Phys. Express* **4** (2011) 121603.

[31] Y. Matsuo, Y. Sato, T. Niinomi, I. Soga, H. Tanaka, and E. Nakamura, *J. Am. Chem. Soc.* **131** (2009) 16048.

[32] D. Kuzuhara, J. Mack, H. Yamada, T. Okujima, N. Ono, and N. Kobayashi, *Chem. Eur. J.* **15** (2009) 10060.

[33] D. Kuzuhara, H. Yamada, S. Mori, T. Okujima, and H. Uno, *J. Porphyrins Phthalocyanines* **15** (2011) 931.

[34] J. H. Choi, T. Honda, S. Seki, and S. Fukuzumi, *Chem. Commun.* **47** (2011) 11213.

[35] C. J. Brabec, F. Padinger, N. S. Sariciftci, and J. C. Hummelen, *J. Appl. Phys.* **85** (1999) 6866.

5. Dimethyl Fused Benzoporphycene Precursor and Its Application to Organic Photovoltaic Cells

5.1 Introduction

The conversion behavior and film formation of a BPc precursor (BPc-pre-1) has been investigated in chapter 4. However BPc-pre-1 poorly dissolved in organic solvents. The thickness of BPc-pre-1 film fabricated by spin-coating was only 20 nm, not sufficient for application to a photoactive layer of organic photovoltaic (OPV) cells.

In this chapter, dimethyl fused benzporphycene precursor (BPc-pre-2) (shown in Fig. 5.1) was synthesized and used. It can be expected that the more bulky substituent enable to dissolve BPc-pre-2 well[1, 2] and reduces the intermolecular aggregation in the film. OPV cells utilizing BPc, which was converted from BPc-pre-2 as a *p*-type semiconductor and [6,6]-phenyl-C_{61}-butyric acid methyl ester (PCBM) as an *n*-type semiconductor was fabricated. The correlation between crystalinity and OPV performance was investigated.

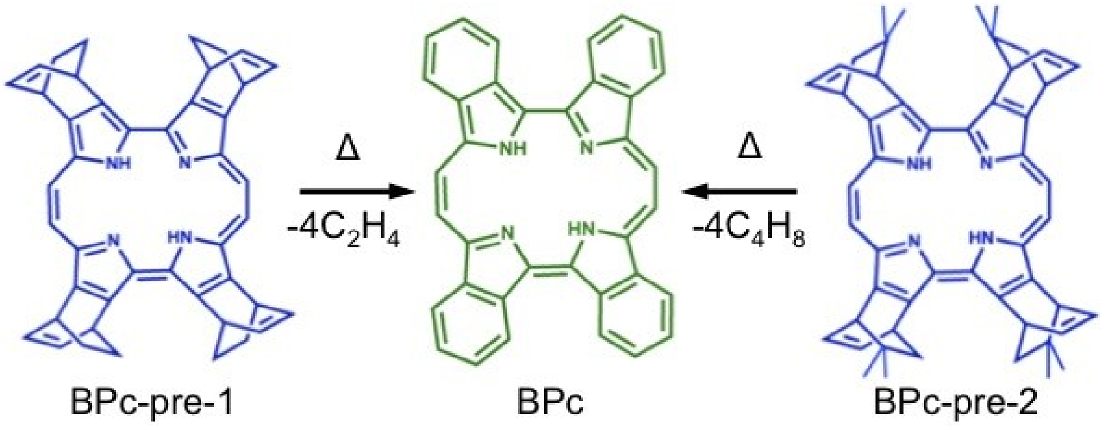

Fig. 5.1. Reaction scheme from BPc-pre-1 and 2 to BPc.

5.2 Experimental

BPc-pre-2 powder and the data of ^{1}H nuclear magnetic resonance (NMR) spectrum of BPc-pre-2 were supplied by Dr. Kuzuhara and Prof. Yamada in NAIST. Dichloromethane proved a good solvent for BPc-pre-1 and BPc-pre-2, and gave a saturated concentration of 0.15% and 0.7% (w/w), respectively. BPc-pre-1 film was spin-coated on indium tin oxide (ITO)/ poly(3,4-ethylenedioxythiophene):poly(styrene sulfonate) (PEDOT:PSS) substrates by spin-coating of saturated BPc-pre-1 dichloromethane solution at 1500 rpm, and BPc-pre-2 film was formed from 0.6% dichloromethane solution. Annealing for thermal conversion was carried out at various temperatures under atmospheric conditions. The optical properties of the films were characterized using an ultraviolet–visible (UV-vis) absorption spectrometer (ALS SEC-2000). The structural change from BPc-pre to BPc was examined using Fourier-transform infrared (FT-IR) spectroscopy (Jasco, FT/IR-660 Plus). Thermogravimetric analysis (TGA) was carried out using a VAP-9000 (Ulvac Riko). Film morphologies were observed by polarized optical microscope (POM, Olympus BX51), atomic force microscopy (AFM, Seiko Instruments, SPI 3800N), field-emission scanning electron microscopy (FE-SEM, Jeol, JSM-7500F), and transmission electron microscopy (TEM, Hitachi, H-7100). Electron diffraction patterns of the films were recorded at an acceleration voltage of 100 kV by TEM.

Hole-only devices were fabricated with PEDOT:PSS and Au electrodes as the anodes and cathodes to measure space charge limited current (SCLC) and calculate the hole mobilities.[3-5)] Au electrode was deposited on the prepared ITO/PEDOT:PSS/BPc. The electrical characteristics were measured using Keithley 4200 source/measure units in the dark.

In this study, *pn* planar junction OPV cells were fabricated. Each cell has common structure as follows: ITO/PEDOT:PSS (30 nm)/BPc (50 nm)/PCBM (30 nm)/LiF (0.5 nm)/Al (60 nm). The BPc layer was fabricated by spin-coating a 0.15% of BPc-pre-1 or 0.6% of BPc-pre-2 solution onto a ITO/PEDOT:PSS substrate and subsequently heating at several temperature and intervals. A PCBM layer (30 nm) was spin-coated from a toluene solution onto each cell. LiF and Al were then vacuum-deposited as an opposite electrode. The current-voltage (*J*-*V*) characteristics of the OPV cells were measured in air under a 100 mW/cm^2 light illumination (AM 1.5) at room temperature, without encapsulation of the devices.

5.3 Results and Discussion

First, re-crystallized and dried BPc-pre-2 powder was analyzed by using ^{1}H NMR spectroscopy. ^{1}H NMR spectrum showed a singlet at 7.32 ppm from chloroform, used in re-crystallization process. The other signals were assigned with BPc-pre-2. ppm 9.79 (4H, meso), 7.25–7.14 (8H, olefin), 5.93

(4H, bridge head), 5.00-4.97 (4H, bridgehead), 2.05-2.00 (4H, bridge), 1.73-1.69 (4H, bridge), 1.52-1.50 (12H, methyl), 0.69 (2H, NH), 0.65-0.58 (methyl). The ratio of amount of BPc molecule and chloroform in dried powder was calculated at about 1:1 from the signals at 7.32 and 7.25–7.14 ppm (Fig. 5.2). When BPc-pre-2 powder was heated, weight loss was observed over the temperature range from 150 to 210 °C (Fig. 5.3). The total weight loss was about 37.0%, which was consistent with the loss of four isobutene groups and chloroform molecule. The results of NMR spectrum and the TG analysis for BPc-pre-2 validate each other. These results indicate that chloroform molecules co-crystalize with BPc-pre-2. Though the size of leaving group and packing structure were different between BPc-pre-2 and BPc-pre-1, the weight loss of BPc-pre-2 was observed over almost same temperature range of BPc-pre-1, from 125 to 210 °C.

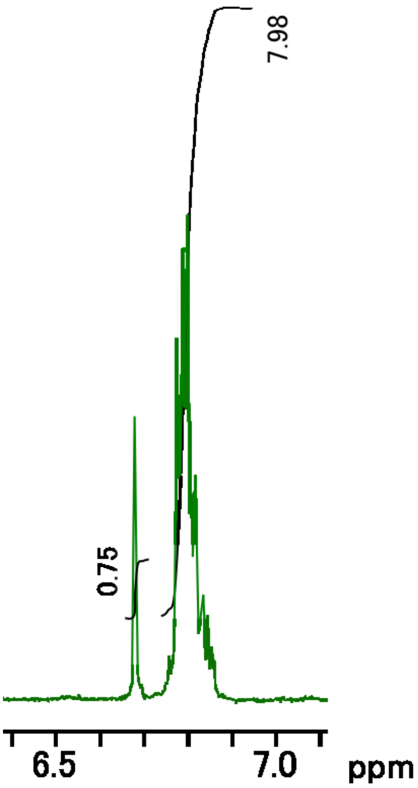

Fig. 5.2. NMR spectrum of BPc-pre-2 powder in $CDCl_3$.

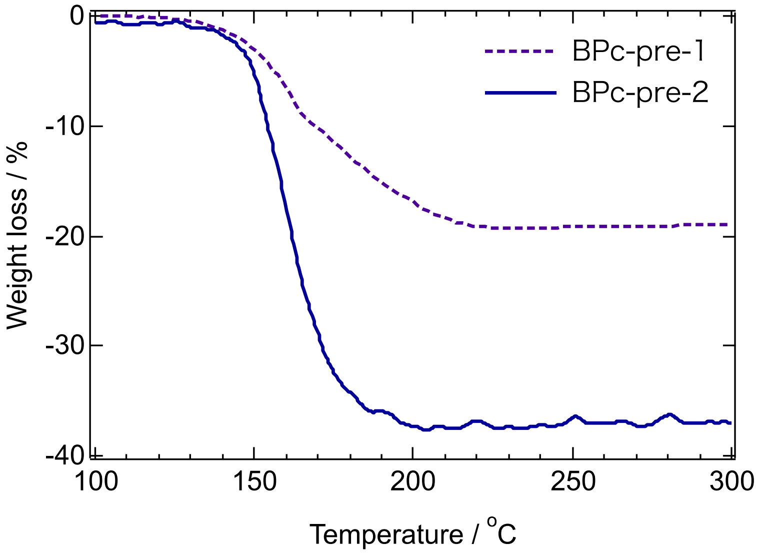

Fig. 5.3. Thermogravimetric curve for BPc-pre-1 and BPc-pre-2.

Figure 5.4 shows the IR spectra of the as-spun BPc-pre-1 and 2 film, and that of the BPc-pre-2 film annealed at 200 °C for 10 min. As-spun BPc-pre-2 film had bands at 1382 and 1450 cm^{-1}, which derives from methyl rock and C-H scissoring vibration modes in CH_3. The other absorption bands of the as-spun BPc-pre-2 film almost corresponded with that of the BPc-pre-1 one. The spectrum of BPc-pre-2 and annealed film showed the common bands at around 1023, 1080, 1339, 1532, 1558, and 1607 cm^{-1}, which derives from vibration modes in porphycene rings. After annealing, weak absorption bands at 1382 and 1450 cm^{-1} and medium absorption bands at 722, 1463, 2865, 2937 and 2954 cm^{-1} were disappeared. As former shown, the former absorption bands derive from methyl rock and C-H scissoring vibration modes in CH_3. The latter bands derive from the vibration modes of C-H bonds in alkane. On the other hand, absorption bands at 734, 812, 888, 1446 and 1602 cm^{-1} were appeared after annealing, which derives from the vibration modes in benzene rings. These results indicate that the dimethyl fused bicyclo structure at outer side of porphycene ring converts into benzene ring.

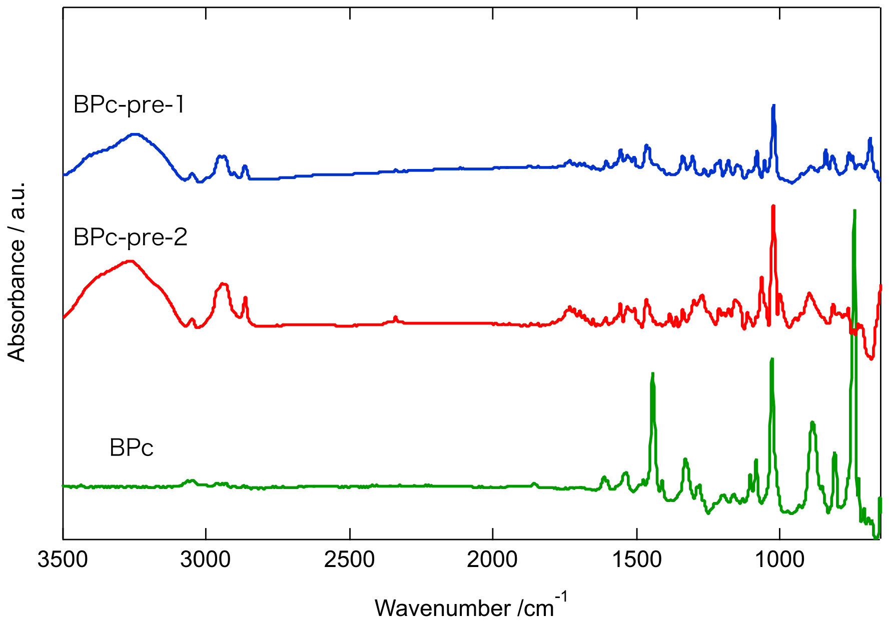

Fig. 5.4. IR spectra of BPc-pre-1, BPc-pre-2, and annealed BPc-pre-2 film.

The color of BPc-pre-2 thin film changed from blue to green by annealing. Figure 5.5 shows the time-dependent UV-vis absorption spectra of BPc-pre-2 film during the annealing process at 200 °C, and the UV-vis absorption spectra of the BPc-pre-1 film before and after annealing at 200 °C for 10 min. The absorption spectrum of the as-spun BPc-pre-2 film exhibited a Soret band at around 390 nm and a Q-band in the wavelength region between 550 and 700 nm. The positions of absorbance peaks of BPc-pre-2 were completely coincident with that of BPc-pre-1. With increased annealing time, the Soret band was redshifted to 450 nm, and the Q band extended to 750 nm. The spectral shape of BPc film converted from BPc-pre-2 was also corresponded with that converted from BPc-pre-1. The differences between the precursors were not observed except for the absorbance, which derives from the film thickness. The thickness for BPc-pre-1 and 2 was 20 nm and 80 nm, respectively. The conversion time depended on the annealing temperature. As increasing of annealing temperature, the reaction rate was increased. In this chapter, the annealing time for device fabrication was set at twice the time for conversion, summarized in Table 5.1.

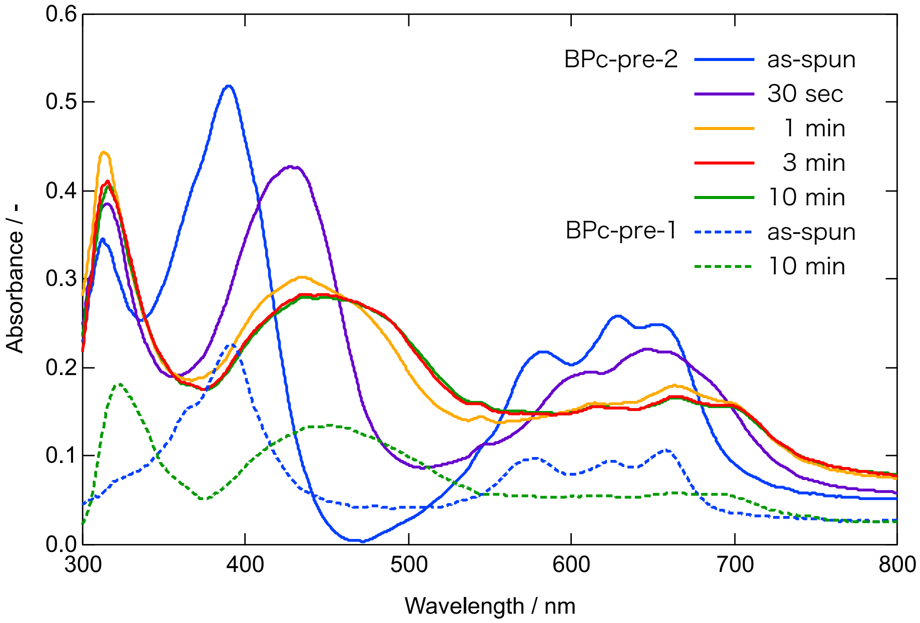

Fig. 5.5. Time-dependent UV-vis absorption spectra of BPc-pre-2 during annealing at 200 °C, and UV-vis absorption spectra of BPc-pre-1 film before and after annealing at 200 °C for 10 min.

Table 5.1. The time for conversion of BPc-pre-2.

Temp. °C	150	170	200	250
Conversion time	120 min	48 min	8 min	1.5 min
Annealing time	240 min	120 min	20 min	3 min

As-spun BPc-pre-2 film was composed of a smooth layer (root-mean-square (RMS) roughness ≈ 0.2 nm; see Fig. 5.6 (a)). The high resolution electron diffraction (HRED) pattern of the as-spun film showed a halo pattern (see Fig. 5.6 (b)), indicating that the BPc-pre-2 film was amorphous. Figure 5.6 (c) shows the AFM image of the BPc-pre-2 film after annealing at 200 °C for 10 min (i.e., BPc film). On the contrary of BPc-pre-1, the BPc film converted from BPc-pre-2 was composed of smooth layer. Though there were many small spots that seems to be generated by desorption of leaving groups, the surface roughness was drastically improved. The selected area electron diffraction (SAED) pattern obtained from a circle with a diameter of 1 μm showed the pattern projected along the *b**-axis of the BPc crystal (triclinic, a = 5.536 Å, b = 14.502 Å, c = 14.754 Å, α

= 98.633°, β = 91.079°, and γ = 96.534°) (Fig. 5.6 (d)).[6)] This indicates that the (010) plane of the BPc crystal is parallel to the substrate surface and BPc molecules take the edge-on orientation as same as that of the BPc film converted from BPc-pre-1. In the case of BPc-pre-1, the precursor aggregates and then converts into BPc, resulting in discontinuous BPc film shown in chapter 4. On the other hand, bulky substituent of BPc-pre-2 reduces the intermolecular aggregation in the film. BPc-pre-2 converts into BPc before aggregation, and BPc subsequently crystalizes, resulting in flat and continuous BPc film.

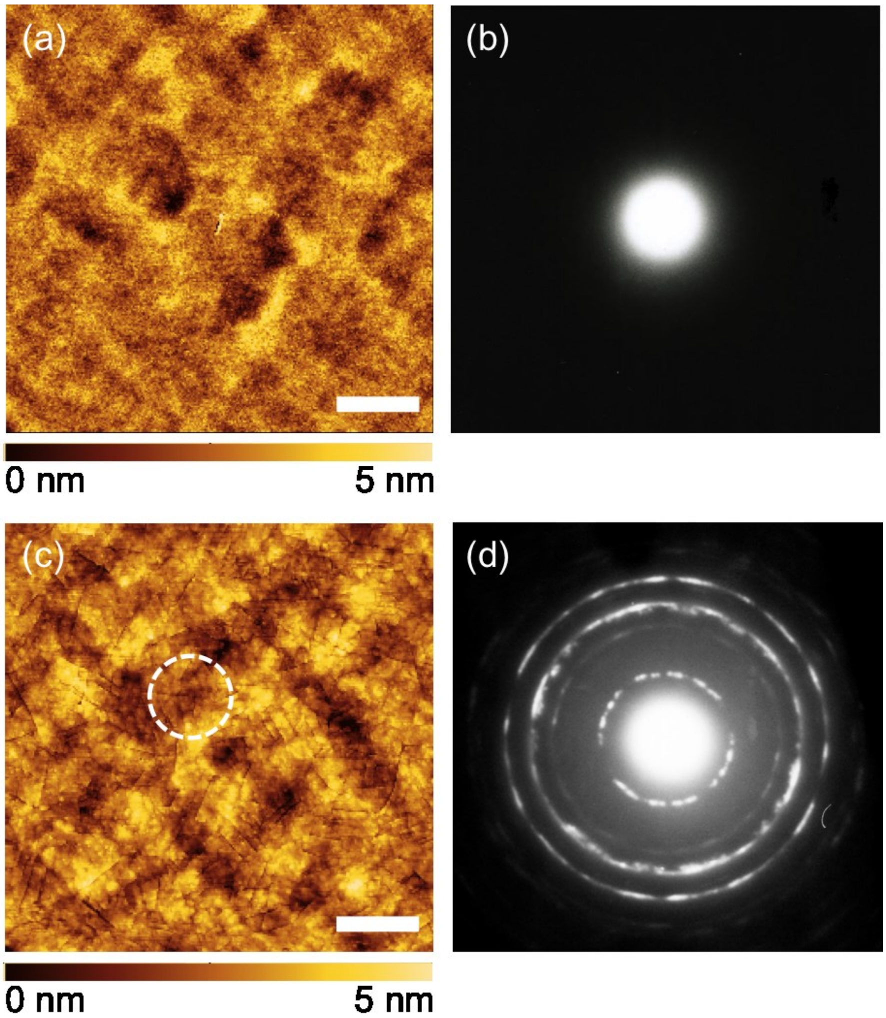

Fig. 5.6. AFM image and SAED pattern of as-spun BPc-pre-2 film (a)(b), and that of BPc-pre-2 film annealed at 200 °C for 10 min (c)(d). Scale bar: 1μm

Figure 5.7 shows XRD patterns of BPc film prepared at several temperature from 150 to 250 °C. BPc film converted at 200 °C clearly showed diffraction peaks at 6.1° and 12.2°, which derives from

(010) and (020) reflections, which is consistent with SAED pattern shown in Fig. 5.6. As decreasing annealing temperature, the crystalinity was also decreased. In particular, BPc film prepared at 150 °C showed the diffraction peak from not only (010) plane but also (001) plane at around 5.9°.

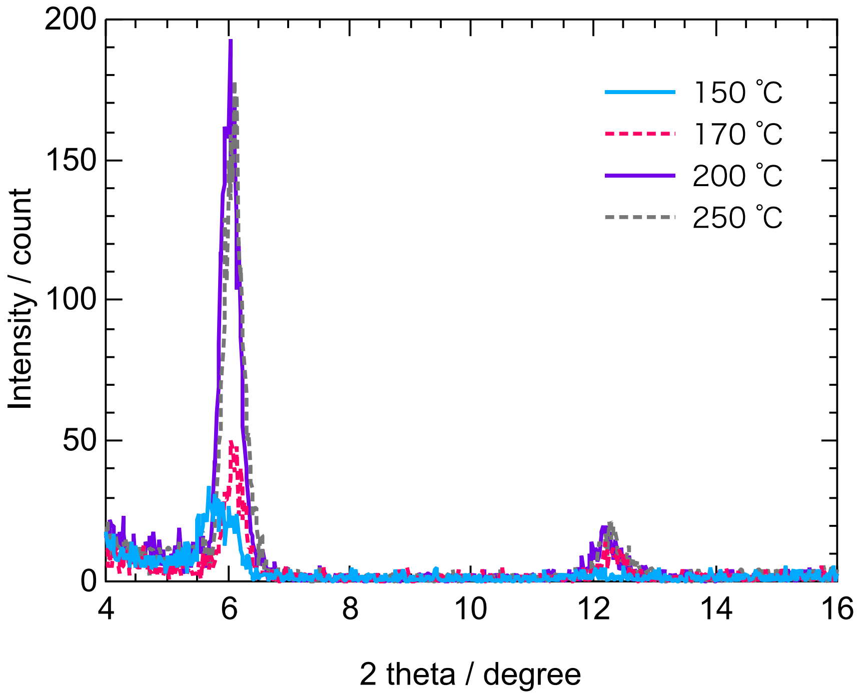

Fig. 5.7. XRD patterns of BPc films prepared at several temperature.

Figure 5.8 shows the AFM images of BPc film converted from BPc-pre-2 at below 200 °C. BPc film converted at 170 °C also had smooth surface (Fig. 5.8 (a)). On the other hand, some aggregates were observed in BPc film prepared at 150 °C indicated by arrow (Fig. 5.8 (b)). As decreasing the annealing temperature, it takes long time to convert into BPc. Though BPc-pre-2 has low cohesive property, BPc-pre-2 even aggregates and then converts into BPc. Therefore, BPc converted from precursor at 150 °C includes the aggregates. The crystalinity of BPc converted from precursor at 150 °C is not so high, resulting in random orientation of BPc crystals.

In annealing at 250 °C, the orientational domain size was dramatically increased (Fig. 5.9 (a)). The most common size of the orientaional domain was about 450 μm^2, which was calculated from POM image. The edges of domains in POM image were also observed in AFM images (Fig. 5.9 (b)). In the zoomed AFM image of the domain (Fig. 5.9 (c)), a lot of tiny cracks were observed but the depth of the observed cracks was about 1 ~ 2 nm. Moreover, the cracks were not observed in the cross-sectional FE-SEM image of BPc film (not shown). Therefore, the cracks are surface structure. Fig. 5.9 (d) shows the superposition of TEM image and the SAED pattern of BPc film prepared at 250 °C. TEM image showed a single net pattern projected along the *b**-axis of the BPc crystal. The angle between the direction of the cracks and the a*-axis was ±37°; the cracks were parallel to the (207) and (20-7) planes of BPc crystals. In real lattice, the (207) and (20-7) planes are parallel to the herringbone packed molecular plane of BPc (Fig. 5.9(e)). BPc crystals are easy to cleave at the molecular planes in order to relax the strain associate with crystallization, resulting in formation of the "herringbone" surface texture.

The height scale in AFM image of each BPc film converted from precursor at between 150 °C and 250 °C was within 10 nm. Therefore we concluded that each BPc film converted from BPc-pre-2 have smooth surface enough to treat as planar OPV cells. Moreover, BPc in each film took edge-on orientation. These results indicate that the crystalinity is variable by annealing temperature without roughening of the film and changing the orientation of BPc crystal. It enables to evaluate direct correlation between crystalinity and device performance.

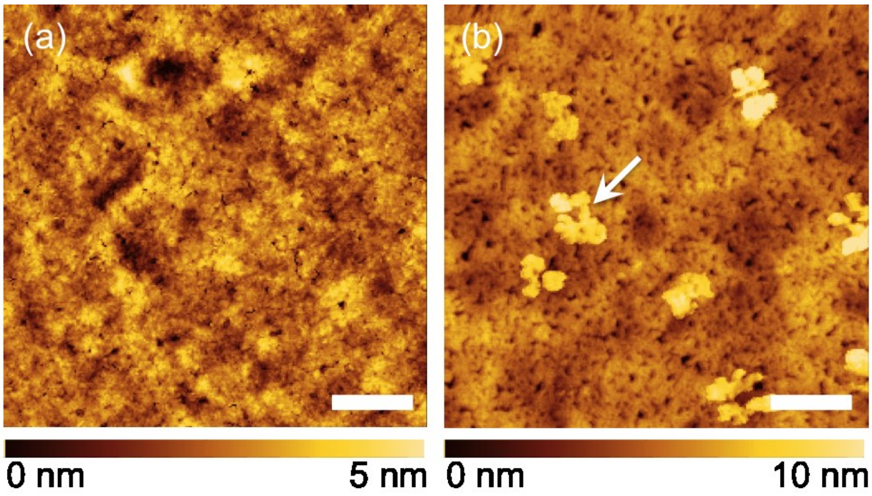

Fig. 5.8. AFM images of BPc films prepared at (a) 170 °C and (b) 150 °C.

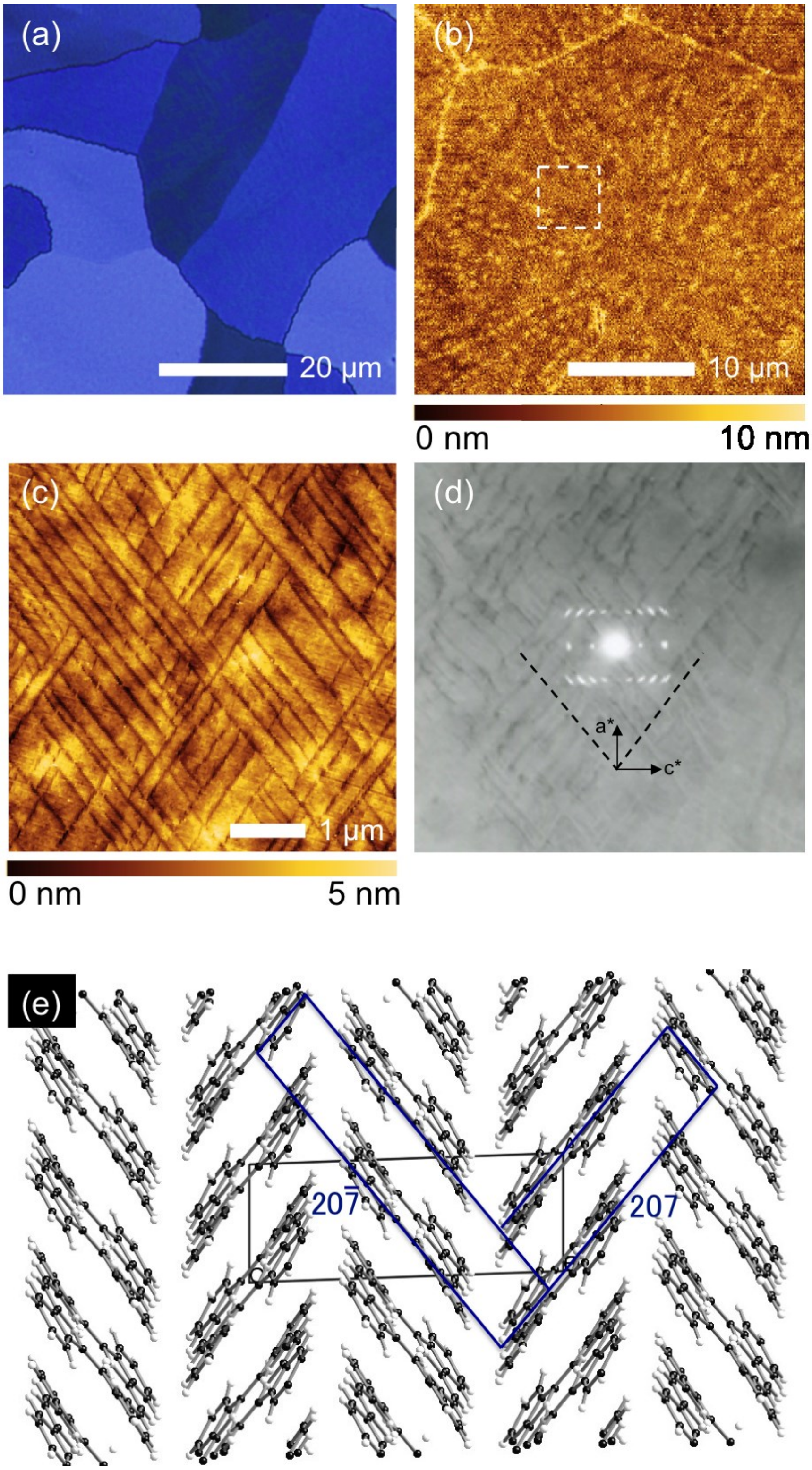

Fig. 5.9. (a) Optical micrograph, (b) 30 μm×30 μm sized and (c) 5 μm×5 μm sized AFM images of BPc film prepared at 250 °C. (d) The superposition of TEM image and SAED pattern. (e) Schematic structure of BPc crystal.

Figure 5.10 shows the *J–V* curves of OPV cells utilizing BPc film converted from BPc-pre-1 and BPc-pre-2. The cell fabricated from BPc-pre-1 showed slight photoconversion under illumination. The photoactive layer of cell utilizing BPc-pre-1 was composed of discrete 100-nm-height BPc grains and 30-nm-thick PCBM film. The thin photoactive layer caused the low rectification and deteriorated photoconversion. The film prepared from BPc-pre-2 drastically improved rectification and cell performance. This indicated that the good *pn* junction formed in the cells. The photovoltaic parameters, such as the short circuit current density (J_{SC}), open circuit voltage (V_{OC}), fill factor (*FF*), power conversion efficiency (PCE) are summarized in Table 5.2. The performance of the photovoltaic cells was found to depend greatly on the annealing temperature. At 150 °C annealing temperature, a power conversion efficiency of 0.61% was obtained. When the annealing temperature was increased to 170 °C and 200 °C, the PCE increased to 1.19% and 1.29%, respectively. The more improvement of device performance was achieved at 250 °C, in which V_{OC} = 0.47, J_{SC} = 5.35, *FF* = 0.59, and the resulting PCE was 1.49%.

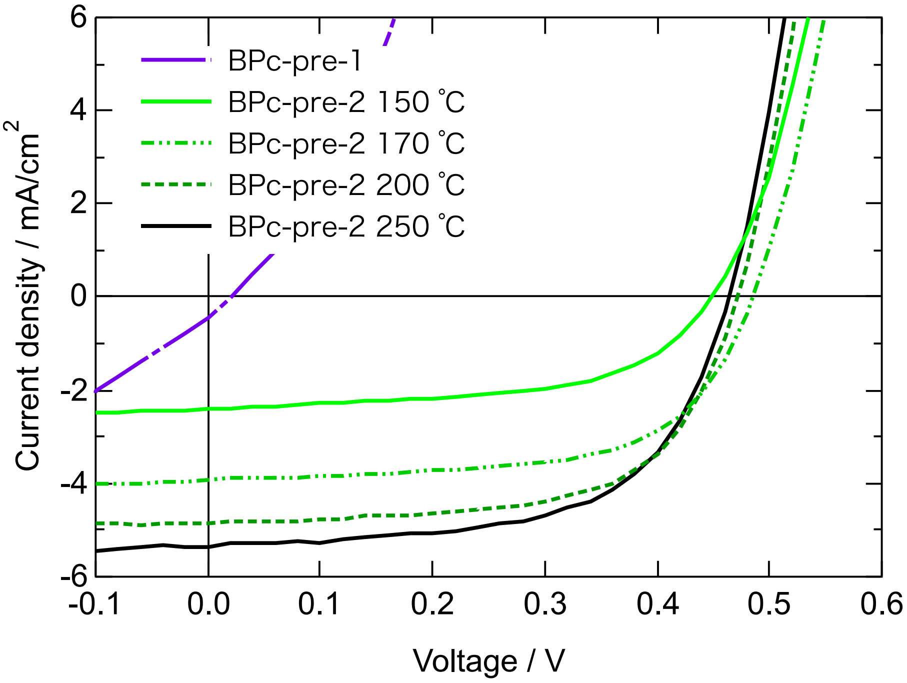

Fig. 5.10. *J-V* curves of OPV cells utilizing BPc converted from precursors under illumination.

PCE was mainly increased by improvement of J_{SC}, therefore, the charge transport properties of the device were additionally investigated. The hole mobilities (μ_h) of the BPc thin films were investigated using SCLC measurements with hole-only devices. Figure 5.11 shows the dark currents of ITO/PEDOT:PSS/BPc/Au devices with the corrected bias, which was determined as the difference between the work function of PEDOT:PSS and the HOMO level of BPc. SCLC behavior can be characterized by the Mott–Gurney square law (Equation(5.1)),

$$J=\frac{9}{8}\mu\varepsilon\frac{V^2}{L^3} \tag{5.1}$$

$$J=\frac{9}{8}\mu\varepsilon_0\varepsilon'\frac{V^2}{L^3} \tag{5.2}$$

where ε is the static dielectric constant of the medium, i.e., the organic layer, ε_0 is vacuum permittivity, ε' is the relative dielectric constant and μ is the charge carrier mobility.7) The relative dielectric constant was assumed at 3.0. The μ_h was calculated from the currents in the square law region, which was also summarized in Table 5.2. The film prepared at 150 °C showed the lowest mobility, 1.56×10^{-3} cm^2 V^{-1} s^{-1}. The μ_h of the BPc film gradually increases as the increasing of annealing temperature. The μ_h of the BPc film prepared at 250 °C reached at 1.29×10^{-2} cm^2 V^{-1} s^{-1}, which is about 10 times of that prepared at 150 °C. The dependence of mobility on annealing temperature is caused by the increasing the crystalinity, as supported by XRD analysis. The increasing of crystalinity enables to pass the carrier effectively, resulting in enhancing the mobility.

Table 5.2. Photovoltaic parameters and the hole mobilities.

Precursor	Temp. (°C)	J_{SC} (mA/cm^2)	V_{OC} (V)	FF (-)	PCE (%)	Mobility (cm^{2}V^{-1}s^{-1})
BPc-pre-1	200	0.36	0.02	0.25	1.8×10^{-3}	
BPc-pre-2	150	2.39	0.45	0.57	0.61	1.56×10^{-3}
	170	3.92	0.48	0.63	1.19	5.17×10^{-3}
	200	4.56	0.47	0.60	1.29	8.56×10^{-3}
	250	5.35	0.47	0.59	1.49	1.29×10^{-2}

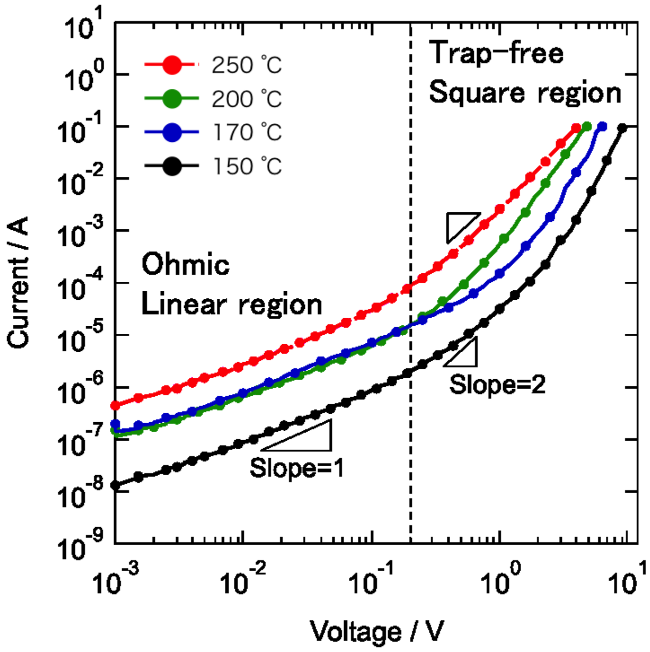

Fig. 5.11. *I-V* curves for hole-only devices.

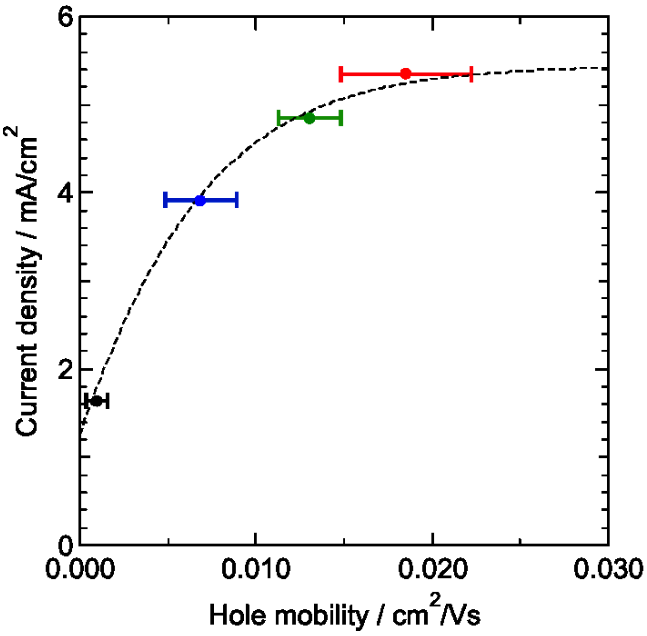

Fig. 5.12. The plot of short circuit current density vs hole mobility.

Figure 5.12 shows a comparison of the J_{SC} and the μ_h of BPc film obtained by SCLC measurements. We found that, in the region below 0.01 cm^2 V^{-1} s^{-1}, the J_{SC} has a good linear relationship with the μ_h, but J_{SC} rather saturates over 0.01 cm^2 V^{-1} s^{-1}. The maximum J_{SC} in this BPc/PCBM cell was roughly calculated as around 7.5 mA/cm^2 from the absorbance of the film and solar spectrum. As increasing of the μ_h, the value will approach to the line of 7.5 mA/cm^2. The orientaional control of BPc crystal will leads to further improvement of carrier mobility, eventually PCE.

5.4 Conclusion

In this chapter, dimethyl fused thermo-convertible BPc precursor was evaluated as an active material for OPV cells. The correlation between crystalinity of BPc and OPV performance was investigated. The findings were as below.

- The novel design of precursor enables to not only dissolve the precursor well into solvent, but also prevent the cohesion of precursor. The BPc converted from BPc-pre-2 had smooth roughness (RMS= ~ 0.2 nm) in each annealing condition (from 150 °C to 250 °C)

- BPc crystals are easy to cleave at the molecular planes in order to relax the strain associate with crystallization, resulting in formation of the “herringbone” surface texture in BPc film prepared at 250 °C.

- As increasing of annealing temperature, the BPc was highly crystalized without roughening the film surface and changing molecular orientation (edge-on), and the hole mobility was enhanced from 1.56×10^{-3} to 1.29×10^{-3} cm^2 V^{-1} s^{-1}. Moreover, the PCE of OPV cells fabricated from BPc-pre-2 was also enhanced from 0.61 % to 1.49 %. The direct correlation between hole mobility and PCE was experimentally demonstrated.

5.5 Reference

[1] T. Okujima, Y. Hashimoto, G. Jin, H. Yamada, H. Uno, and N. Ono, *Tetrahedron*, **64**, 2405 (2008).

[2] H. Yamada, T. Okujima, and N. Ono, *Chem. Commun.* 2957 (2008).

[3] P. W. M. Blom, M. J. M. de Jong, M. G. van Munster, *Phys. Rev. B*, **55**, R656 (1997).

[4] V. D. Mihailetchi, J. K. J. van Duren, P. W. M. Blom, J. C. Hummelen, R. A. J. Janssen, J. M. Kroon, M. T. Rispens, W. J. H. Verhees, M. M. Wienk, *Adv. Funct. Mater.*, **13**, 43 (2003).

[5] C. Melzer, E. J. Koop, V. D. Mihailetchi, and P. W. M. Blom, *Adv. Func. Mater.*, **14**, 865 (2004).

[6] D. Kuzuhara, H. Yamada, S. Mori, T. Okujima, and H. Uno, *J. Porphyrins Phthalocyanines* **15** (2011) 931.

[7] M. A. Lampert, P. Mark, Current injection in Solids, Academic Press, New York 1970.

6. Fabrication and Semiconducting Properties of Monodisperse n-Type Phthalocyanine Nanograss

6.1 Introduction

The texture of the interface between *p*-type and *n*-type semiconductors is an important parameter that determines the performance of organic photovoltaic (OPV) cells. The diffusion length of photogenerated excitons in organic materials is typically in the order of 10 nm.1-4) Therefore, to maximize the dissociation of excitons and charge collection, control of the *p*-*n* junction nanostructure is a crucial factor.5, 6) In chapter 4, thin film of benzoporphycene (BPc) was controlled by phase-separation of BPc and [6,6]-phenyl-C_{61}-butyric acid methyl ester (PCBM). However the diameter of BPc grain was sub-micrometer and the shape was tabular, not sufficient small to dissociate charge carriers effectively. The tabular benzoporphycene crystals are due to its crystal orientation. π-Stacking direction was parallel to the substrate, and BPc crystals grow preferentially to in-plane. The orientation control is an important factor to fabricate vertically long grains.

On the other hand, the fabrication of semiconducting nanorods has been widely investigated7-9) to increase the interface between *pn* interface, and drastically improvement in power conversion efficiency (PCE) was demonstrated. However, *n*-type organic semiconducting nanorods have not been reported to date.

In previous studies, metal-2,3,9,10,16,17,23,24-octacyanophthalocyanine ($MPc(CN)_8$) (M = 2K, Cu, Fe, Co, Ni, Zn) molecules were synthesized on metal and/or alkali halide substrates by chemical vapor deposition (CVD) of tetracyanobenzene (TCNB).10-13) $MPc(CN)_8$ molecules are formed on the metal substrate by the tetramerization of vaporized TCNB molecules.10) $MPc(CN)_8$ molecules form $MPc(CN)_8$–M complexes and stack face-to-face with π-to-π distances of approximately 0.34 nm along the long axis of the crystals, thereby forming upright-standing, micrometer-sized, needle-like crystals.10) This structure has potential for efficient charge dissociation and collection at the electrode. Cyclic voltammetry measurements of $MPc(CN)_8$ and $MPc(CN)_8$–M complexes have been performed by Louati *et. al* 14) and Takeshita *et. al* 15), respectively. The redox properties of $MPc(CN)_8$ and its complexes shift toward the anodic direction compared with that of unsubstituted phthalocyanine, which indicates that $MPc(CN)_8$ is a good electron-accepting material.

In this chapter, a $K_2Pc(CN)_8$–K film was prepared on a single KCl crystal in an attempt to fabricate monodisperse $K_2Pc(CN)_8$–K nanograss. The semiconducting characteristics of the $K_2Pc(CN)_8$–K nanograss, such as the field effect and photovoltaic properties, were investigated.

6.2 Experimental

6.2.1 Preparation of $K_2Pc(CN)_8$–K nanograss on KCl

A $K_2Pc(CN)_8$–K film was prepared from TCNB (Tokyo Kasei Inc., no further purification) and KCl. Single-crystal KCl specimens were purchased from Okenshoji Co., Ltd and cleaved in air. TCNB and KCl were placed into a 10 mm diameter Pyrex test tube with TCNB at the end of the tube and the 100 mm^2 KCl crystal held at a distance of 50 mm from the TCNB. After evacuating and purging with argon gas three times, the tube was melt-sealed at 10 Pa. Each sealed tube was approximately 100 mm long. The sealed tube was heated at a prescribed temperature and time in a hot air oven. The substrates covered with a $K_2Pc(CN)_8$–K film were then cleaved to half their original thickness.

6.2.2. Characterization of $K_2Pc(CN)_8$–K nanograss on KCl

The films deposited on KCl crystals were examined using UV-vis absorption spectroscopy (Jasco V-670). The surface morphology was investigated using field emission-scanning electron microscopy (FE-SEM; Jeol JSM-7500M). Films for high-resolution transmission electron microscopy (HRTEM; Jeol JEM-200CX) were separated from the KCl substrates by contact with a water surface, and then mounted on a microgrid. Photoemission yield spectroscopy (PYS; Bunkou Keiki BIP-KV201) was performed on a thin film of $K_2Pc(CN)_8$–K to determine the highest occupied molecular orbital (HOMO) level. The sample for PYS was prepared by mounting a $K_2Pc(CN)_8$–K film on indium tin oxide (ITO)-coated glass. The lowest unoccupied molecular orbital (LUMO) level was estimated from the HOMO levels and the band gaps determined from the spectral edge of the UV-vis absorption spectrum.

A $K_2Pc(CN)_8$–K field-effect-transistor (FET) was fabricated as follows. Source and drain electrodes were formed on top of an *n*-type Si wafer with a thermally grown oxide (ca. 300 nm thick) by photolithography (lift-off) of Au (100 nm)/Cr (5 nm). The channel length and width were 50 μm and 5 mm, respectively. A $K_2Pc(CN)_8$–K film floated on water was then mounted on the substrate and heated at 60 °C for 10 min under dry N_2 gas flow. The FET properties were measured with a semiconductor parameter analyzer (Keithley 4200). Two photovoltaic devices (Fig. 6.1), ITO/(poly(3-hexylthiophene-2,5-diyl) (P3HT; Aldrich):$K_2Pc(CN)_8$–K)/LiF/Al (device A) and ITO/P3HT/nanograss $K_2Pc(CN)_8$–K/LiF/Al (device B), were also fabricated using P3HT and $K_2Pc(CN)_8$–K as the *p*-type and *n*-type semiconductors, respectively. The active layer in device A was fabricated as follows. $K_2Pc(CN)_8$–K formed on the KCl substrate was dispersed in water and subsequently centrifuged. After washing with water and acetone several times, the $K_2Pc(CN)_8$–K powder was dried at 135 °C for 3 h. The $K_2Pc(CN)_8$–K powder was then dissolved in a chloroform solution containing 12 mg/mL P3HT, (1:1 weight ratio). The $K_2Pc(CN)_8$–K/P3HT film was spin-coated from a chloroform solution onto an ITO substrate at 1500 rpm and then heated at 135 °C for 20 min. For device B, the $K_2Pc(CN)_8$–K film was fabricated on the substrate at 330 °C for 24 h with 0.5 mg of TCNB. The length of the nanograss was estimated to be ca. 300 nm from FE-SEM measurements. The P3HT film was then spin-coated from a chloroform solution (12 mg/mL) onto the $K_2Pc(CN)_8$–K /KCl substrate. In this case, the P3HT film acts not only as a *p*-type semiconductor, but also as a reinforcement layer. The P3HT/$K_2Pc(CN)_8$–K film was then separated from the KCl substrate on a water surface. The floated film was transferred onto an ITO substrate by horizontal lifting transfer, and subsequently dried at room temperature for 1 h followed by heating at 135 °C for 20 min. A LiF (0.5 nm)/Al (60 nm) bilayer as a cathode electrode was vacuum-deposited on each substrate under a vacuum of 5×10^{-4} Pa. The *J*-*V* characteristics of the as-prepared photovoltaic cell were measured using a Keithley 2400 sourcemeter in air with 100 mW/cm^2 light illumination (AM1.5).

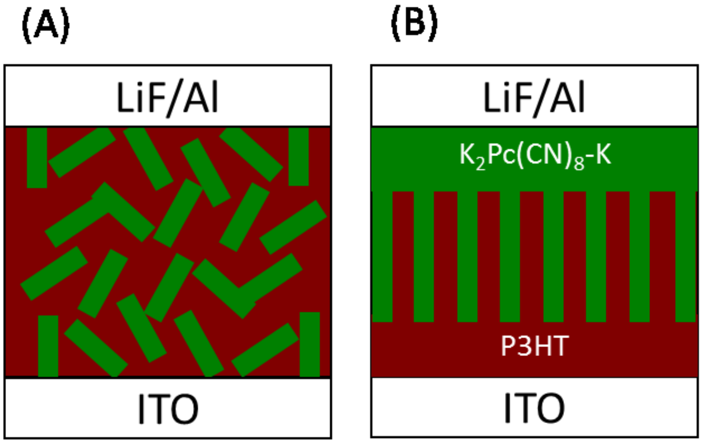

Fig. 6.1. Schematic diagrams of device structures: (A) ITO/(P3HT:$K_2Pc(CN)_8$–K)/LiF/Al and (B) ITO/P3HT/nanograss $K_2Pc(CN)_8$–K/LiF/Al.

6.3 Results and discussion

6.3.1 Morphological control of $K_2Pc(CN)_8$–K nanograss

We have determined that it is possible to limit the growth of the films by adjustment of the amount of TCNB feed. Figure 6.2 shows UV-vis absorption spectra of several $K_2Pc(CN)_8$–K films prepared with different amounts of TCNB, and that of a vacuum-deposited CuPc film as a reference. The amount of TCNB was varied from 1.0 to 0.1 mg under a fixed heating temperature of 300 °C. The absorbance of the film was proportional to the amount of TCNB. FE-SEM images of the films prepared with various amounts of TCNB are shown in Figs. 6.3(a)–(d). As with the UV-vis absorption spectra (Fig. 6.2), the length of the nanograss was approximately proportional to the amount of TCNB used. Therefore, it is possible to fabricate nanograss with a controlled length by simply adjusting the amount of TCNB addition.

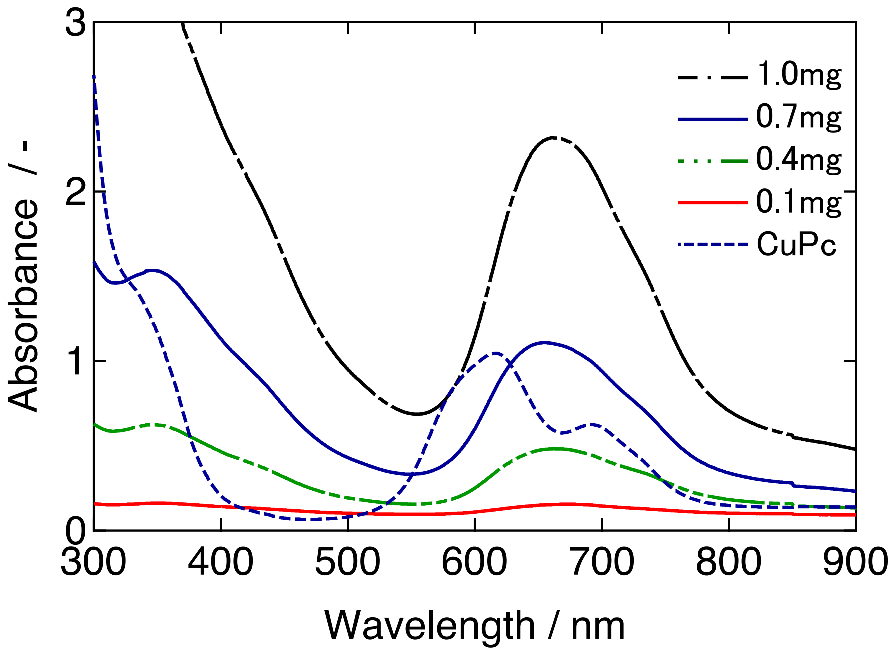

Fig. 6.2. UV-vis spectra of $K_2Pc(CN)_8$–K films prepared with various amounts of TCNB and CuPc film.

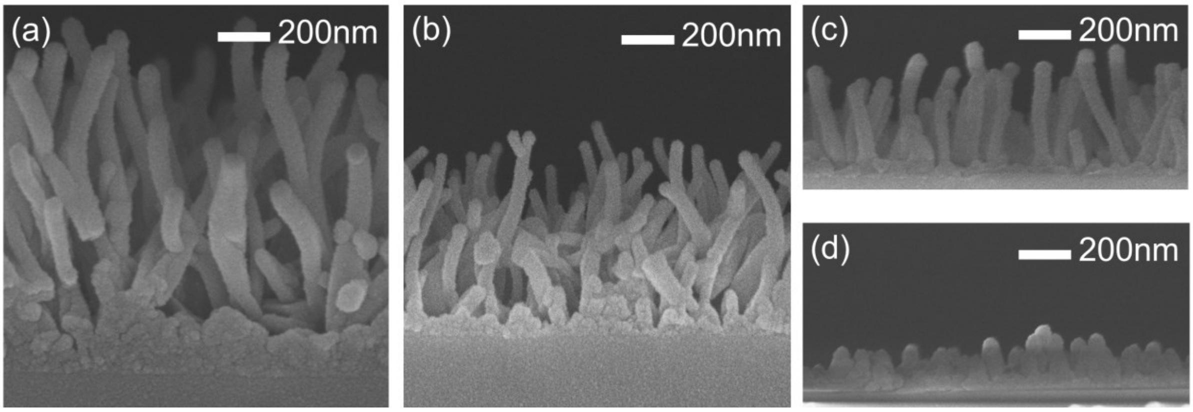

Fig. 6.3. Cross-sectional FE-SEM images of $K_2Pc(CN)_8$–K films prepared with various amounts of TCNB: (a) 1.0, (b) 0.7, (c) 0.4, and (d) 0.1 mg.

Figure 6.4 shows histograms of the length of rods consisting of nanograss obtained from FE-SEM images of $K_2Pc(CN)_8$–K films prepared at various temperatures. The nanograss formed at 240 °C for 24 h was relatively short, which indicates that these conditions are not sufficient for reaction with the TCNB. In contrast, the nanograss heated at over 270 °C for 24 h had an average length of approximately 200 ~ 300 nm, which indicates that heat treatment at 270 °C for 24 h is

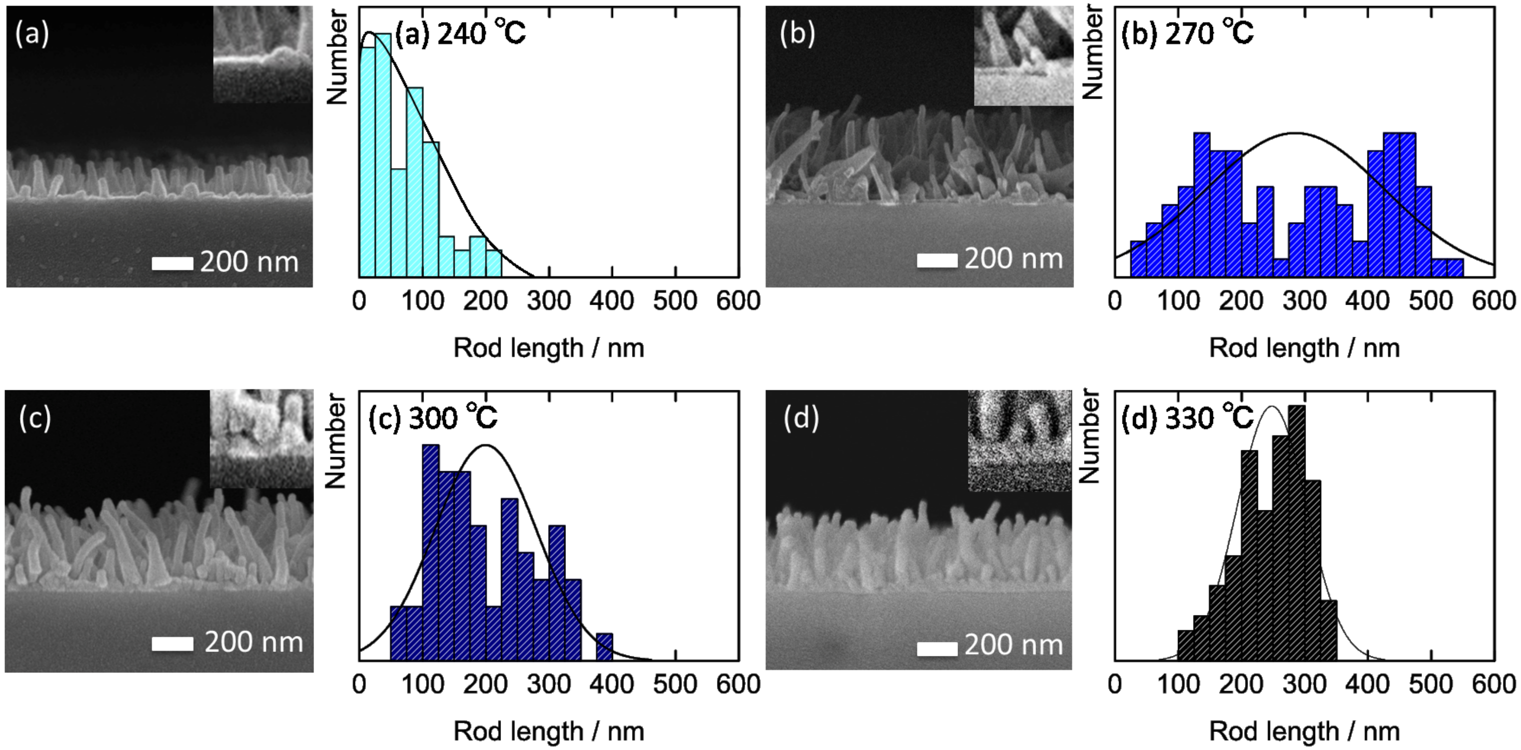

Fig. 6.4. Length distribution of rods consisting of nanograss and cross-sectional FE-SEM images of K2Pc(CN)8–K films fabricated with 0.5 mg TCNB at (a) 240, (b) 270, (c) 300, and (d) 330 °C for 24 h. The insets in the FE-SEM images show the interface between the nanograss and the substrate.

sufficient to induce reaction with the TCNB. The heating temperature also affected the film morphology. The length of rods consisting of nanograss formed at 270 °C had a wide distribution. A high heating temperature was effective (e.g., 330 °C) for the fabrication of nanograss with a uniform length that is vertically aligned on the substrate. As the nanograss became monodisperse, the diameter of the individual rods also approached a saturation value (60 nm). It should be noted that the gaps between the rods were occupied by $K_2Pc(CN)_8$–K grains, except for the film formed at 240 °C; see insets in the FE-SEM images of Fig. 6.4.

The synthesis method used allows the simultaneous formation of molecules and the film of nanograss. Therefore, an understanding of the reaction scheme is important for elucidating the mechanism of film formation. Scheme 6.1 shows that $K_2Pc(CN)_8$ molecules are formed by the tetramerization of TCNB with potassium in KCl.[11)] The amount of $K_2Pc(CN)_8$ produced is determined by the amount of metal and TCNB, assuming that the reaction temperature and time are sufficient to induce reaction. In the present experiments investigating the control of the $K_2Pc(CN)_8$–K nanograss length, sufficient metal was provided for the reaction, because the substrate material is single KCl crystal. Therefore, the amount of TCNB supplied determined the amount of $K_2Pc(CN)_8$ produced.

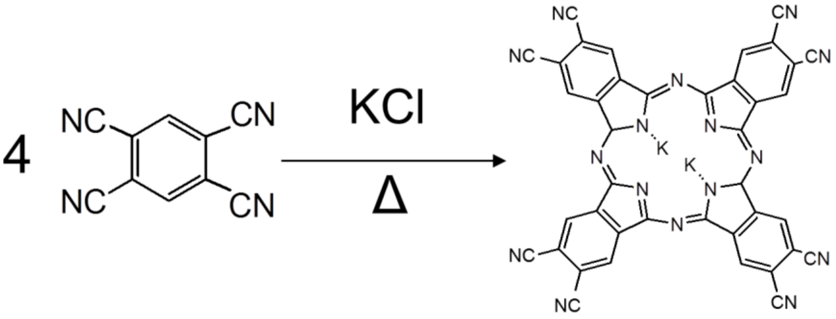

Scheme 6.1. Reaction scheme for the synthesis of $K_2Pc(CN)_8$.

Figure 6.5 shows a box plot of the nanograss length and the absorbance at 660 nm, as a function of the amount of TCNB. In addition to the nanograss length, the absorbance of the films increased linearly with the amount of TCNB supplied. This consistency between the nanograss length and absorbance indicates that TCNB reacts with metal at the top of the nanograss, and the nanograss grows sequentially. The sequential growth is attributed to the unique reaction and the crystal structure of the nanograss.

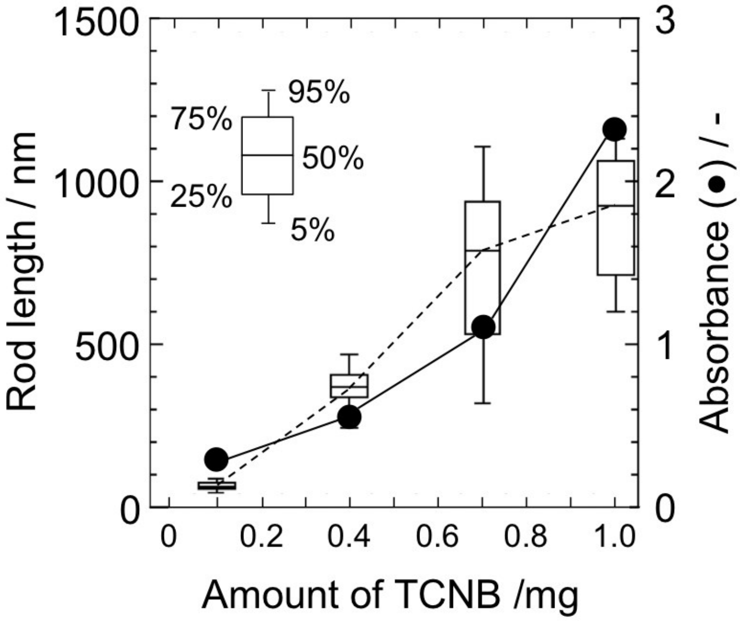

Fig. 6.5. Nanograss length as a function of the amount of TCNB, and the absorbance at 660 nm.

Figure 6.6(a) shows a HRTEM micrograph of disk-like crystallites formed at the initial stage of reaction that create a grid pattern with a spacing of 1.56 nm, which coincides with the a and b lattice constants of tetragonal cells. These results demonstrate that the crystals have their c axis perpendicular to the KCl(100) surface. In this conformation, $K_2Pc(CN)_8$ molecules are stacked in a staggered arrangement within the crystal (Fig. 6.6(b)).10) In the crystals of the $K_2Pc(CN)_8$–K complex, the phthalocyanine molecules are stacked and the central metal atoms are overlapped (Fig. 6.6(c)), where the overlap acts as the metal distribution channel.13) TCNB reacts with the metal at the top of the nanograss, resulting in growth of the nanograss.

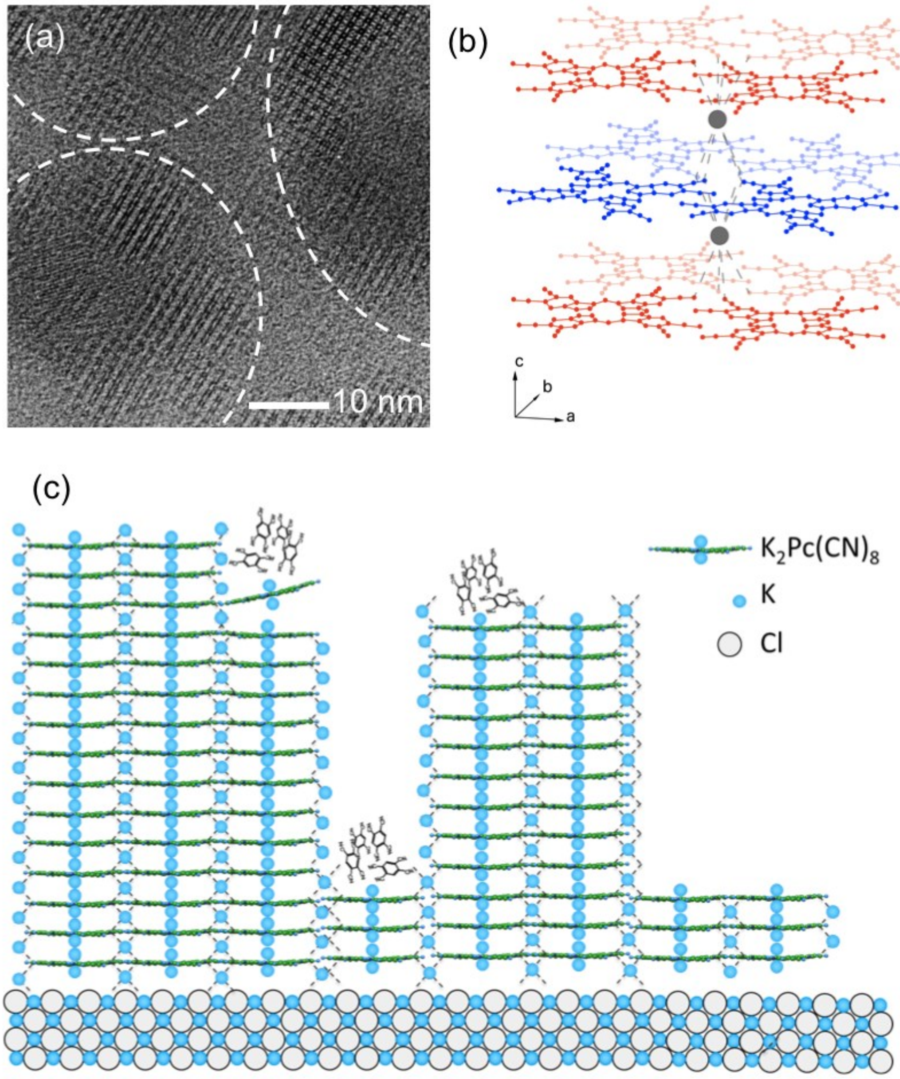

Fig. 6.6. (a) HRTEM image of $K_2Pc(CN)_8$–K at the initial growth phase showing many domains with a grating-like structure. (b) Schematic image of a $K_2Pc(CN)_8$–K complex crystal. (c) Schematic diagram showing the growth of the $K_2Pc(CN)_8$–K complex crystals.

UV-vis absorption spectroscopy also provides relevant information regarding the packing structure in the films. Many of the phthalocyanine molecules take herringbone-packing structures in the crystal and exhibit large splitting of the Q-band (Davydov splitting). CuPc forms an α-phase in the thin films and exhibits Davydov splitting. However, the $K_2Pc(CN)_8$–K films did not show Q-band splitting, because the relative position of the molecules causes alignment of the transition dipoles parallel to each other. The absorption spectra of the $K_2Pc(CN)_8$–K films had similar profiles, regardless of the nanograss length, which confirms that the nanograss is entirely composed of crystals of the $K_2Pc(CN)_8$–K complex, i.e., from the bottom to the top of the nanograss. These results also indicate that nanograss growth occurs sequentially in the vertical direction. The heating temperature was found to determine the uniformity of the nanograss. Scheme 6.1 shows that the production of $K_2Pc(CN)_8$ is determined by the addition of TCNB and metal. The diffusion of metal in the nanograss is the most important factor that determines the uniformity of the nanograss length. The area where the central metals overlap in the $K_2Pc(CN)_8$–K crystals acts as a metal distribution channel. The distribution of the rod lengths directly reflects the number of defects in this metal distribution channel. This result can be explained by the increase in the diffusion rate due to annealing at high temperature, which minimizes the contribution of defects, so that uniform growth of the nanograss is achieved.

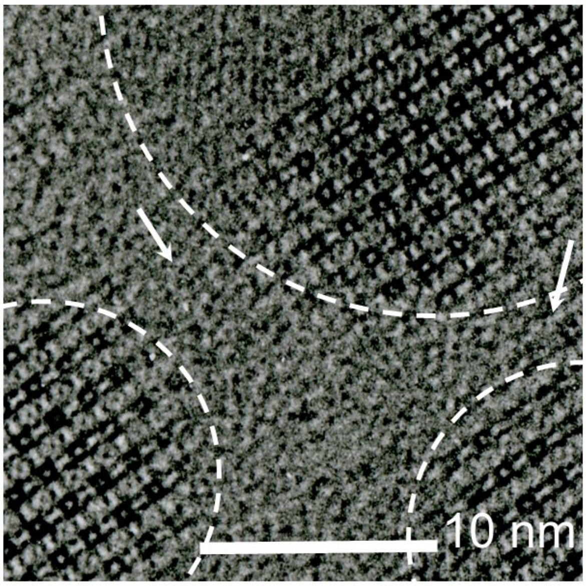

Fig. 6.7. HRTEM image of $K_2Pc(CN)_8$–K at the initial growth phase with emphasis on the gaps between the disk-like crystallites. The arrows indicate the gaps.

The mechanism for the formation of $K_2Pc(CN)_8$ grains in the gaps between the rods was investigated using HRTEM. In the case of very thin films, a region with many defects existed between the disk-like domains (Fig. 6.7). This indicates that if $K_2Pc(CN)_8$–K domains with different epitaxial orientations collide, in-plane coalescence arises with defects, which would result in an area with multiple defects. It is considered that the metal atoms, which act as nuclei for the tetramerization of TCNB, are transferred through the phthalocyanine ring channel. This channel is solidly formed in the ordered structure consisting of $K_2Pc(CN)_8$–K complex structures, which results in faster rate of formation of phthalocyanine molecules. In contrast, the growth rate in the disordered regions is slow and grains with relatively small size grow in these gaps.

6.3.2 Semiconducting properties of $K_2Pc(CN)_8$–K films

PYS measurements were performed on thin $K_2Pc(CN)_8$–K films to determine the HOMO level of $K_2Pc(CN)_8$–K. The results indicate that $K_2Pc(CN)_8$–K has a HOMO level of 5.80 eV, and has a relatively larger ionization potential than an unsubstituted phthalocyanine such as CuPc. The ionization potential is strongly dependent on the substituents in the benzene ring. Thus, the electron withdrawing effect of the CN-group stabilizes π conjugation. A LUMO level of 4.30 eV for $K_2Pc(CN)_8$–K was determined from the absorption edge, indicating a relatively narrow band gap (1.50 eV).

Figure 6.8 shows the drain-source current-voltage characteristics of $K_2Pc(CN)_8$–K films at different gate voltages. The positive values of both the drain and gate voltages indicate that $K_2Pc(CN)_8$–K is an electron-transporting (*n*-type) material. However, the water-flow transferred film has a non-negligible effect of trapped water.16) The measurement method also has a problem with the contact between the $K_2Pc(CN)_8$–K film and SiO_2 surface, which leads to a significantly distorted I_d–V_d profile and prevents observation of the I_d versus V_g^2 relation in the transfer characteristics and accurate calculation of the electron mobility. Evaluation of the field effect behavior of $MPc(CN)_8$ films has been previously attempted using vacuum deposition and spin-coating techniques.17) However, these characteristics were not observed due to decomposition caused by heating. In the presently used CVD method, synthesis and film formation can be performed at the same time, which allows for the formation of $MPc(CN)_8$ films without decomposition, and as such, measurement of their FET characteristics. The channel of a FET is formed at the interface between the semiconducting film and the insulating layer; therefore, conduction cannot be achieved by only the nanograss structures. This supports our finding that the gaps between the rods were occupied by small $K_2Pc(CN)_8$–K grains.

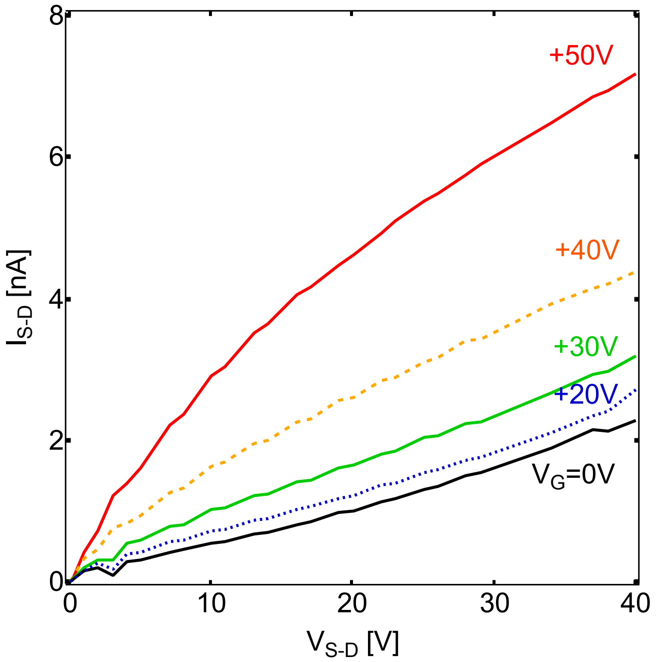

Fig. 6.8. Drain-source current-voltage characteristics of a FET consisting of $K_2Pc(CN)_8$–K films measured at various gate voltages.

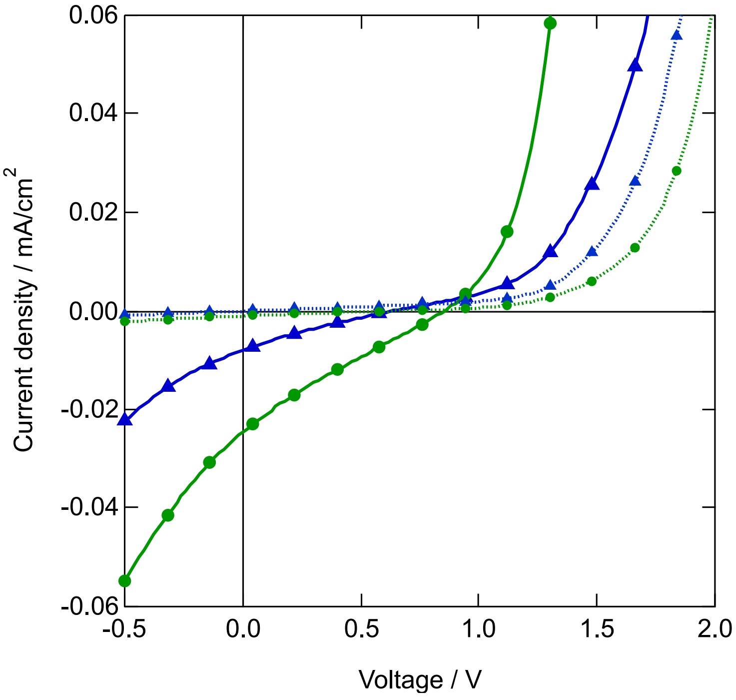

Fig. 6.9. *J*–*V* characteristics of bulk-heterojunction cells (device A (▲)) and a P3HT/nanograss $K_2Pc(CN)_8$–K device (device B (●)). Solid line: under illumination; dotted line: dark conditions.

Figure 6.9 shows *J–V* curves for devices A and B, obtained under both illumination and dark conditions. Each device showed good rectification in the dark and photovoltaic effects under illumination. The open circuit voltage (V_{OC}), short circuit current density (J_{SC}), fill factor (*FF*), and PCE of device A were 0.62 V, 8.0 μA/cm^2, 0. 20, and 1.1×10^{-3}%, respectively. In the case of device B, these parameters were 0.85 V, 24.4 μA/cm^2, 0.23, and 4.7×10^{-3} %, respectively. The LUMO level of $K_2Pc(CN)_8$–K was determined to be 4.3 eV in this work. The HOMO level of P3HT has been widely investigated and determined to be 5.0-5.2 eV.18, 19) According to semiconductor physics, V_{OC} is proportional to the difference between the HOMO level of the donor material and the LUMO level of the acceptor compound.20) V_{OC} for the P3HT/$K_2Pc(CN)_8$–K OPV device was calculated to be approximately 0.7-0.9 V, which validates both the PYS and *J-V* measurements. The PCE of device B was approximately four times better than that of device A as a result of the increased parameters (J_{SC} in particular). The enhanced J_{SC} was attributed to the efficient dissociation and collection of photogenerated hole-electron pairs at the interface between the $K_2Pc(CN)_8$–K nanograss and P3HT. The efficient charge collection structure also slightly improved the *FF*. The formation and alignment of the nanograss on the substrate was an important factor for improvement of the PCE.

However, the J_{SC} and *FF* were still low, due to the high series resistance of the device.21-23) The series resistance of OPV cells containing $K_2Pc(CN)_8$–K nanograss was estimated to be approximately 3000 Ω/cm^2. The high series resistance results from two non-optimal points. One is the setting of the film thickness to 300 nm for device fabrication. The length of nanograss used as a photoactive layer in OPV cells should be between 100 and 200 nm; therefore, to fabricate nanograss of this length, the amount of TCNB feed should be set to 0.1–0.3 mg (Fig. 6.7). However, a film thickness of over 300 nm was required to fabricate a self-supporting film on water with sufficient mechanical strength to withstand breaking. Another point is that annealing and solvent annealing processes were not employed for penetration of P3HT between the rods.24) When used, these processes caused shrinking of the films, so that the *J-V* characteristics could not be measured. These points can be overcome by the appropriate selection of an electrode material for inverted cells and direct fabrication of the nanograss on the device substrate. Even though the fabrication process is primitive, these preliminary results are encouraging and demonstrate the advantages of this approach for the fabrication of efficient OPVs.

6.4 Conclusion

Growth of vertical *n*-type phthalocyanine nanograss was achieved using the CVD method with TCNB. The nanograss was characterized as *n*-type semiconducting layer in OPV cells. The findings were as below.

- The process was controlled to achieve monodisperse nanograss with individual rod diameters of 60 nm and lengths of 250 nm.

- The gaps between the rods were fully covered with $K_2Pc(CN)_8$–K complex grains. The film continuity at the interface between the substrate and the nanograss layer allowed measurement of the FET characteristics of the material. The $K_2Pc(CN)_8$–K complex film exhibited *n*-type conduction characteristics on the FET.

- The energy of the HOMO level of $K_2Pc(CN)_8$–K was determined to be 5.8 eV.

- Organic photovoltaic cells containing $K_2Pc(CN)_8$–K as an *n*-type semiconductor were also fabricated, and the PCE of a cell containing vertical-aligned-nanograss was approximately four times larger than that of a nanograss dispersed bulk-heterojunction-type cell.

6.5 Reference

[1] M. Theander, A. Yartsev, D. Zigmantas, V. Sundstrom, W. Mammo, M.R. Andersson, O. Inganas, *Phys. Rev. B* **61**, 12957 (2000).

[2] A. Haugeneder, M. Neges, C. Kallinger, W. Spirkl, U. Lemmer, J. Feldmann, U. Scherf, E. Harth, A. Gugel, K. Mullen, *Phys. Rev. B* **59**, 15346 (1999).

[3] J.J.M. Halls, K. Pichler, R.H. Friend, S.C. Moratti, A.B. Holmes, *Appl. Phys. Lett.* **68**, 3120 (1996).

[4] T. Stubinger, W.J. Brutting, *Appl. Phys.* **90**, 3632 (2001).

[5] R.A. Marsh, C. Groves, N.C. Greenham, *J. Appl. Phys.* **101**, 083509 (2007).

[6] P.K. Watkins, A.B. Walker, G.L.B Verschoor, *Nano Lett.* **5**, 1814 (2005).

[7] F. Yang, M. Shtein, S.R. Forrest, *Nature Matter.* **4**, 37 (2005).

[8] Y. Zheng, R. Bekele, J. Ouyang J. Xue, *J. Org. Electron.* **10**, 1621 (2009).

[9] M. Hirade, H. Nakanotani, M. Yahiro, C. Adachi, *ACS App. Mater. Interfaces* **1**, 80 (2010).

[10] M. Ashida, Y. Ueda, H. Yanagi, N. Uyeda, Y. Fujiyoshi, J.R. Fryer, *Acta Crystallogr.* **B44**, 146 (1988).

[11] M. Ashida, Y. Ueda, H. Yanagi, K. Sayo, *J. Polym. Sci. A Polym. Chem.* **27**, 3883 (1989).

[12] H. Yanagi, Y. Ueda, M. Ashida, *Bull. Chem. Soc. Jpn* **61**, 2313 (1988).

[13] Y. Ueda, H. Yanagi, S. Hayashi, M., Ashida, *J. Electron Microsc.* **38,** 101(1989).

[14] A. Louati, M.E. Meray, J.J. Andre, J. Simon, K.M. Kadish, M. Gross, A. Giraudeau, *Inorg. Chem.* **24**, 1175 (1985).

[15] K. Takeshita, M. Ashida, *J. Electrochem. Soc.* **138**, 2617 (1991).

[16] Y. Y. Noh, J. J. Kim, Y. Yoshida, K. Yase, *Adv. Mater.* **15**, 699 (2003).

[17] Z. Bao, A.J. Lovinger, J. Brown, J. Am. Chem. Soc. **120**, 207 (1998).

[18] U. Salzner, J.B. Lagowski, P.G. Pickup, R.A. Poirier, Synth. Met., **96**, 177 (1998).

[19] T. Johansson, W. Mammo, M. Svensson, M. Andersson, O. Inganäs, *J. Mater. Chem.* **13**, 1316 (2003).

[20] M. C. Scharber, D. Muhlbacher, M. Koppe, P. Denck, C. Waldauf, A. J. Heeger, and C. J. Brabec, *Adv. Mater.* **18**, 789 (2006).

[21] S. M. Sze, Physics of Semiconductor Devices, Wiley-Interscience, New York 1981

[22] M. A. Green, Solar Cells: Operating Principles, Technology, and System Applications, Prentice-Hall, Englewood Cliffs, NJ, USA 1982.

[23] J. D. Servaites, S. Yeganeh, T. J. Marks, M. A. Ratner, *Adv. Func. Mater.* **20**, 97 (2010).

[24] D. C. Olson, Y. J. Lee, M. S. White, N. Kopidakis, S. E. Shaheen, D. S. Ginley, J. A. Voigt, J. W. P. Hsu, *J. Phys. Chem. C* **111**, 16640 (2007).

7. Conclusions

This thesis offers two unique methods to fabricate the films of novel porphyrinoids, precursor method and CVD method. Fabrication and utilizing these films in OPV cells leads to a contribution to the understanding of the photophysical and charge transporting processes for photovoltaic applications. Using high-performance p-i-n stacked OPV cell and constructing measurement system enables to evaluate the photovoltaic parameters of the devices immediately after Al deposition, and also revealed the phenomena at hetero-interfaces.

There are a number of conclusions that can be drawn from the work in this thesis as follows.

In chapter 2, the current-voltage characteristics of BP-PCBM solar cells were measured subsequent to deposition of Al as a cathode material until the time when the device is exposed to N_2 gas at atmospheric pressure. Even in vacuum, shifts of photovoltaic parameters was observed at 20 min after Al deposition (aging effect). The displacement of N_2 gases in the evaporation chamber enhanced the photovoltaic parameters, in particular V_{OC}. The PCE was increased 24% over the initial characteristics. The change of photovoltaic parameters can be well explained by the formation of AlO_X. Future work should be focused upon the development of air-stable cathode with very-thin and uniform insulating layer at the semiconductor-electrode interface for durable and high performance OPV cells.

In chapter 3, the morphology, optical and photovoltaic properties of vacuum deposited BPc film were reported. BPc took edge-on orientation in the vacuum deposited BPc film. The BPc film showed broad absorption in visible region, and the HOMO level of BPc was also determined at 5.1 eV. The OPV cell utilizing vacuum deposited BPc film showed nearly 1% PCE; BPc is a promising candidate for photoactive material for OPV cell.

In chapter 4, the thermal conversion behavior of a BPc-pre and the film formation of BPc in the presence of PCBM were reported. The BPc films were composed of discrete particles over 100 nm in height due to aggregation of BPc-pre. On the other hand, during heat conversion process of BPc-pre/PCBM mixture film, both BPc and PCBM crystallized independently and PCBM crystals dramatically inhibited the aggregation of BPc, resulting in a phase-separated structure. Repeated spin-coating of BPc-pre and PCBM in dichloromethane solution and subsequent annealing allowed the thickness of BPc films to be increased. BPc crystallized homoepitaxially on the underlying crystalline BPc layer after each deposition step. The thermal conversion conditions affected the size of BPc crystals and the photovoltaic properties of the corresponding cell. An organic photovoltaic cell containing a repeatedly-stacked BPc film prepared at 250 °C showed good rectification and a PCE of 0.16%. The correlation between the coverage of *p*-type semiconducting layer and photovoltaic properties was revealed.

In chapter 5, dimethyl-fused benzporphycene precursor (BPc-pre-2) was synthesized and used. The novel design of precursor enables to not only dissolve the precursor well into solvent, but also prevent the cohesion of precursor. The crystalinity is variable by annealing temperature without roughening of the film and changing the orientation of BPc crystals (edge-on). As increasing of annealing temperature, the BPc was highly crystalized, and the hole mobility was enhanced from 1.56×10^{-3} to 1.29×10^{-3} cm^2 V^{-1} s^{-1}. Moreover, the PCE of OPV cells fabricated from BPc-pre-2 was also enhanced from 0.61% to 1.49% and exceeded that of OPV cells composed of vacuum-deposited film. The direct correlation between hole mobility and PCE was experimentally demonstrated.

In chapter 6, formation of $K_2Pc(CN)_8$–K complex crystal was controlled to uniform nanograss with individual rod diameters of 60 nm and lengths of 250 nm. This is the first report on the fabrication of n-type semiconducting nanograss. The amount of TCNB simply determined the length of rods. The reaction temperature was found to determine the length distribution of the rods consisting of nanograss. The energy of the HOMO of $K_2Pc(CN)_8$–K was determined to be 5.8 eV. The PCE of a cell containing vertical-aligned-nanograss was approximately four times larger than that of a nanograss dispersed bulk-heterojunction-type cell. The formation and alignment of the nanograss on the substrate were important factors for the improvement of the PCE.

In conclusion, precursor and CVD methods are promising route for fabricating the thin film of novel porphyrinoids, having good semiconducting properties. However, BPc mainly took edge-on orientation, which is not favorable orientation for OPV cells. For controlling molecules to face-on orientation and fabricating high performance OPV cells, further investigation of materials should also be carried out. Fabrication method of $K_2Pc(CN)_8$-K complex nanograss is also still primitive. In the future, the film should be directly constructed on the target substrate. The design of apparatus for film formation, which enables to control of the pressure and convection in the reactor etc., will open the door to more precise control of film structure and further improvement of semiconducting properties.

List of Achievements

List of Publication

[1] H. Saeki, K. Hirohara, Y. Koshiba, S. Horie, M. Misaki, K. Takeshita, K. Ishida and Y. Ueda, Current-voltage characteristics of organic photovoltaic cells following deposition of cathode electrode, *Applied Physics Letters*, **97**, 193307, 2010. (Top 20 most downloaded)

[1'] (Note) H. Saeki, K. Hirohara, Y. Koshiba, S. Horie, M. Misaki, K. Takeshita, K. Ishida and Y. Ueda, Current-voltage characteristics of organic photovoltaic cells following deposition of cathode electrode, *Virtual Journal of Nanoscale Science & Technology*, **22**, 2010.

[2] H. Saeki, O. Kurimoto, M. Misaki, D. Kuzuhara, H. Yamada and Y. Ueda
Thermal Conversion Behavior and Morphology Control of Benzoporphycene from a Novel Soluble Precursor, *Applied Physics Express*, **6**, 035601 (2013).

[3] H. Saeki, M. Misaki, D. Kuzuhara, H. Yamada and Y. Ueda
Fabrication of Phase-separated Benzoporphycene/[6,6]-Phenyl-C_{61}-Butyric Acid Methyl Ester Films for Use in Organic Photovoltaic Cells, *Japanese Journal Applied Physics*, 投稿中.

[4] H. Saeki, M. Misaki, D. Kuzuhara, H. Yamada and Y. Ueda
Dimethyl Adducted Benzoporphycene Precursor and Its Application to Organic Photovoltaic Cells, 投稿準備中.

[5] H. Saeki, M. Nishimoto, Y. Koshiba, M. Misaki, K. Ishida and Y. Ueda
Fabrication and Semiconducting Properties of Monodisperse n-Type Phthalocyanine Nanograss, *Thin Solid Films*, **531**, 513-518 (2013).

(Note) The publishing thesis [1] was selected by the member of editorial board of American Physic

Society, and was reprinted in Virtual Journal of Nanoscale Science & Technology of issues on November 15, 2010.

List of Bulletin

[1] 佐伯宏之、広原和門、木梨憲司、三崎雅裕、上田裕清
可溶性前駆体を用いた高効率 p-i-n 有機薄膜太陽電池の創成
神戸大学連携創造本部先端研究推進部門　2009 年度年報、Vol. 5、115-116、2010 年

[2] 西本光穂子、佐伯宏之、三崎雅裕、上田裕清
ナノピラー構造を有する有機薄膜太陽電池の創成
神戸大学連携創造本部先端研究推進部門　2010年度年報、Vol. 6、121-122、2011年

International Conference

[1] Hiroyuki Saeki, Kazuto Hirohara, Yasuko Koshiba, Masahiro Misaki, Kenji Ishida, Yasukiyo Ueda and Kimiya Takeshita, p-i-n Junction Organic Photovoltaic Cell Prepared by Wet Process, Fourth East Asia Symposium on Functional Dyes and Advanced Materials, Osaka International House Foundation, Japan, Jul. 2009.

[2] Hiroyuki Saeki, Kazuto Hirohara, Yasuko Koshiba, Masahiro Misaki, Kenji Ishida and Yasukiyo Ueda, p-i-n Organic Photovoltaic Cell Prepared by Wet Process, Workshop on Information, Nano and Photonics Technology 2009, Kobe University, Japan, Nov. 2009.

[3] Hiroyuki Saeki, Masahiro Misaki, Yasuko Koshiba, Satoshi Horie, Kenji Ishida and Yasukiyo Ueda, Behavior of current-voltage characteristics of polythiophene: fullerene solar cell just after deposition of metal cathode, International Conference on Science and Technology of Synthetic Metals 2010, Kyoto international conference center, Japan, Jul. 2010.

[4] Hiroyuki Saeki, Masahiro Misaki, Yasuko Koshiba, Satoshi Horie, Kenji Ishida and Yasukiyo Ueda, Initial I-V characteristics of organic photovoltaic cells, 2010 International Chemical Congress of Pacific Basin Societies, Hawaii, USA, Dec. 2010.

[5] Hiroyuki Saeki, Masahiro Misaki, Yasuko Koshiba, Satoshi Horie, Kenji Ishida and Yasukiyo Ueda, Effect of organic-inorganic interfacial control on the initial I-V characteristics of organic photovoltaic cells, Sixth International conference on Molecular Electronics and Bioelectronics, Sendai international center, Japan, Mar. 2011.

[6] Hiroyuki Saeki, Mihoko Nishimoto, Yasuko Koshiba, Masahiro Misaki, Satoshi Horie, Kenji Ishida and Yasukiyo Ueda, Nano-structure control of octacyanophthalocyanine thin-film prepared by chemical vapor deposition, Korea-Japan Joint Forum (KJF 2011) Organic Materials Electronics and Photonics, Gyeongju, Korea, Sep. 2011.

[7] Hiroyuki Saeki, Mihoko Nishimoto, Yasuko Koshiba, Masahiro Misaki, Satoshi Horie, Kenji Ishida and Yasukiyo Ueda, Fabrication of dense n-type phthalocyanine nano-rod array, MNC 2011, 24th International Microprocesses and Nanotechnology Conference, Kyoto, Japan, Oct. 2011.

[8] Hiroyuki Saeki, Mihoko Nishimoto, Yasuko Koshiba, Masahiro Misaki, Satoshi Horie, Kenji Ishida and Yasukiyo Ueda, Morphology control of octacyanophthalo- cyanine for nano-rod array of n-type organic semiconductor, Materials Research Society (MRS) fall meeting, Boston, USA, Nov. 2011.

[9] Hiroyuki Saeki, Mihoko Nishimoto, Yasuko Koshiba, Masahiro Misaki, Kenji Ishida and Yasukiyo Ueda, Fabrication and photovoltaic characterization of $K_2Pc(CN)_8$-K complex nano-rod, International Conference on Electroluminescence 2012 (ICEL 2012), Fukuoka, Japan, Sep. 2012.

[10] Hiroyuki Saeki, Masahiro Misaki, Daiki Kuzuhara, Hiroko Yamada and Yasukiyo Ueda, Preparation of Benzoporphycene Thin Film from a Novel Soluble Precursor and Its Application to Organic Photovoltaic Cells, 12th European Conferene on Molecular Electronics (ECME 2013), London, England, Sep. 2013.（発表予定）

National Congress

[1] 佐伯宏之、広原和門、小柴康子、石田謙司、上田裕清、竹下公也「可溶性低分子系材料によるバルクヘテロ接合型有機薄膜太陽電池の作製と評価」２００９年春季　第５６回応用物理学関係連合講演会、筑波大学、２００９年３月

[2] 佐伯宏之、広原和門、小柴康子、三崎雅裕、石田謙司、上田裕清、竹下公也「大気下湿式法により作製した p-i-n 接合型有機薄膜太陽電池の評価」２００９年秋季　第７０回応用物理学会学術講演会、富山大学、２００９年９月

[3] 佐伯宏之、広原和門、小柴康子、石田謙司、上田裕清「電極蒸着直後における有機薄膜太陽電池の光電変換特性変化」２００９年度　先端膜工学研究推進機構*春季講演*会、神戸大学、２０１０年３月

[4] 佐伯宏之、三崎雅裕、小柴康子、堀江聡、石田謙司、上田裕清「デバイス作製直後における有機薄膜太陽電池の光電変換特性挙動と有機-無機界面の効果」２０１０年秋季　第７１回応用物理学会学術講演会、長崎大学、２０１０年９月

[5] 佐伯宏之、三崎雅裕、小柴康子、石田謙司、上田裕清「有機半導体ナノロッドの作製と特性評価」２０１１年春季　第５８回応用物理学関係連合講演会、厚木、２０１１年３月

[6] 佐伯宏之、西本光穂子、小柴康子、三崎雅裕、堀江聡、石田謙司、上田裕清「オクタシアノフタロシアニンナノロッドの均一成長制御」２０１１年秋季　第７２回応用物理学会学術講演会、山形大学、２０１１年８月

[7] 佐伯宏之、西本光穂子、小柴康子、三崎雅裕、石田謙司、上田裕清「オクタシアノフタロシアニンのナノロッド構造制御」２０１１年度　先端膜工学研究推進機構*春季講演*会、神戸大学、２０１２年３月

[8] 佐伯宏之、西本光穂子、小柴康子、三崎雅裕、堀江聡、石田謙司、上田裕清「フッ化リチウム蒸着膜上でのオクタシアノフタロシアニン薄膜の生成と評価」２０１２年春季　第５９回 応用物理学関係連合講演会、早稲田大学、２０１２年３月

[9] 佐伯宏之、栗本大海、小柴康子、三崎雅裕、上田裕清、葛原大軌、山田容子「熱転化型ベンゾポルフィセン薄膜(II) -有機薄膜太陽電池の作製と評価-」２０１２年秋季　第７３回応用物理学会学術講演会、愛媛大学、２０１２年９月

[10] 佐伯宏之、小柴康子、三崎雅裕、上田裕清「可溶性ベンゾポルフィセン前駆体の有機薄膜太陽電池への応用」２０１２年度　先端膜工学研究推進機構*春季講演*会、神戸大学、２０１３年３月

[11] 佐伯宏之、栗本大海、小柴康子、三崎雅裕、上田裕清、葛原大軌、山田容子「新規ベンゾポルフィセン前駆体を用いた有機薄膜太陽電池の作製と評価」２０１３年春季
第６０回 応用物理学関係連合講演会、神奈川工科大学、２０１３年３月

Reward

[1] 応用物理学会有機分子バイオエレクトロニクス分科会主催
第２３回分子工学若手夏の学校、講演奨励賞受賞、神戸、２００９年９月

[2] 京都大学ベンチャー・ビジネス・ラボラトリー主催
アイデアコンテスト　テクノ愛‘09、入賞受賞、京都、２００９年１１月

[3] 日経新聞社主催
テクノルネサンス・ジャパン　東レ賞、最優秀賞受賞、東京、２０１０年１月

[4] 応用物理学会有機分子バイオエレクトロニクス分科会主催
有機分子・バイオエレクトロニクスの未来を拓く若手研究者討論会
講演奨励賞受賞、愛媛、２０１０年９月

[5] 京都大学ベンチャー・ビジネス・ラボラトリー主催
アイデアコンテスト　テクノ愛‘09、入賞受賞、京都、２０１０年１１月

[6] 平成二十三年度先端膜工学研究推進機構春季講演会
優秀ポスター賞受賞、神戸、２０１２年３月

[7] 平成二十四年度先端膜工学研究推進機構春季講演会
優秀ポスター賞受賞、神戸、２０１３年３月

Acknowledgements

I wish to express my most sincere gratitude and appreciation to both Prof. Yasukiyo Ueda and Dr. Kenji Ishida who together made it possible for me to spend these precious five and half years in Ui-lab at Kobe university with all its benefits (traveling to conferences, excellent lectures and research facilities etc.) where I could learn so much not only about science but also life.

I thank Prof. S. Nishiyama, Prof. A. Mori, Kobe University, and Prof. H. Yamada, NAIST, for serving on my supervisory committee and for their careful perusal of this thesis.

Thanks to Dr. D. Kuzuhara, NAIST, Dr. S. Aramaki and Dr. K. Takeshita, Mitsubishi chemical group science and technology research center, I had the opportunity to use the excellent molecules and research in this exciting new field.

I would like to thank Dr. M. Misaki and Dr. Y. Koshiba who spent many hours to read and comment on the manuscript. For experimental support, I want to thank Dr. N. Tanigaki (AIST), Dr. T. Mizokuro (AIST), M. Nishimoto (currently Kao corp.), O. Kurimoto (Kobe University), T. Onishi (Kobe University), Dr. S. Horie (currently Sensors & Works Co., LTD.), Dr. A. Suda (currently Sensors & Works Co., LTD.) and Dr. T. Takechi (Kobe University). I want to thank Dr. Y. Kuroda (currently Mitsuboshi belting ltd.), Dr. K. Sasaki (currently Idemitsu Kosan co., ltd.) and T. Watanabe (Iwate University) who spent their life of doctoral course together for many interesting and exciting discussions of film formation and organic photovoltaic cell. Furthermore, I want to thank Dr. Y. Yoshida, Dr. T. Yamanari, Dr. H. Ogo, AIST, Prof. K. Takahashi, Dr. T. Taima, Dr. T. Kuwabara, Kanazawa University, Dr. T. Miyadera, JST, Dr. T. Koganezawa, JASRI, Prof. N. Yoshimoto, Iwate University, Prof. A. Kubono, Shizuoka University, Dr. S. Nagamatsu, KAIST and Dr. K. Kinashi, currently Kyoto Institute of Technology, for fruitful comments.

I would like to thank Kobe Technical Club (KTC) and Center for Membrane and Film Technology in Kobe University for their generous financial support. I want to thank Asahi Kasei corp. to give me this excellent opportunity.

Last but not least I would like to thank my whole family for their endless support.

Doctoral Dissertation, Kobe University
“Study on organic photovoltaic cell utilizing thin film of novel porphyrinoids
（新規ポルフィリノイド薄膜を用いた有機薄膜太陽電池に関する研究）”, 116 pages
Submitted on July, 9th, 2013
The date of publication is printed in cover of repository version published in Kobe University Repository Kernel.